Beta Decay Studies of Neutron-Rich Nuclei

BY

Mark Steven Curtin

A Dissertation

Submitted to

Michigan State University

in partial fulfillment of the requirements

for the degree of

DOCTOR OF PHILOSOPHY

Department of Physics

1985

ABSTRACT

Beta Decay Studies of Neutron-Rich Nuclei

By

Mark Steven Curtin

The half-lives of eight neutron-rich light nuclei have been measured using the Reaction Product Mass Separator at NSCL. Utilizing a 30 MeV/A ^{18}O beam from the K500 cyclotron at the National Superconducting Cyclotron Laboratory it was possible to generate sufficient yields of exotic nuclei to determine half-lives. The previously unknown half-lives of ^{14}Be and ^{17}C are reported within this thesis along with the half-lives of ^{9}Li, ^{11}Li, ^{12}Be, ^{12}B, ^{14}B and ^{15}B providing a check on the accuracy of the experimental technique. The half-lives were obtained through repeated measurements of the time interval between the detection of a heavy-ion reaction product and its associated beta. Yield information from the experiment suggests the existance of a reaction

mechanism intermediate between direct and fragmentation mechanisms namely, one in which the neutron-excess of the target plays an increasingly important role in the yields of very neutron-rich nuclei. Shell model predictions for the beta decay of these nuclei are presented and compared to the measured values. This experiment also provided the first significant test of the mass separating properties of the RPMS. The performance of the RPMS is discussed in appendix A.

ACKNOWLEDGMENTS

First and foremost I would like to thank my advisor, Dr. J.A. Nolen, Jr. for suggesting this thesis project and for his dedicated help and guidance throughout both my undergraduate and graduate careers. Without his help and friendship this thesis would not have become reality. I would also like to thank Hobson Wildenthal and Alex Brown for sharing with me their insight into the nuclear shell model. Many thanks go to Leigh Harwood and Al Zeller for their valuable advise concerning magnetic systems and to Steve Bricker for his work on the RPMS. I would like to thank the entire staff at the Cyclotron Laboratory for making the Lab a pleasant place to work (and sometimes live). To my fellow graduate students I would like to say that your friendship and good times will always be remembered. In particular, I wish to thank Jim Duffy and Andrea Micallef for their constant friendship and to the racquetball duo Jack and Don for the "good times".

Finally, I wish to thank my family and the Capen family for their constant love and support throughout this endeavor. To my brother Mike, with whom I have been fortunate to share many of my ideas and dreams, thank you from the bottom of my heart. To my mother whose constant love provided the necessary motivation to complete this work, thank you. Lastly, I would like to thank my fiance Mary for her love, patience and understanding throughout this last and difficult year.

LIST OF FIGURES

LIST OF TABLES

TABLE OF CONTENTS

Chapter 1 - Introduction to the Study of Exotic Nuclei

1.1 Introduction and Motivation

The field of nuclear physics is dedicated to the study of dynamical and structure aspects associated with a system of nucleons interacting via the strong force. Until recently, the testing ground for experimental investigations of such nuclear systems has been limited to nuclei residing on or near the valley of stability. Similarly for light nuclei ($A \leq 40$) investigations of nuclear dynamics has been restricted to relatively cold normal-density nuclear systems where single-particle descriptions of the observed phenomena prevail. The contemporary understanding of such combinations of protons and neutrons belonging to the described regime is based on a shell model theory. Although present day shell model theories have proven extremely successful over limited regimes, many questions concerning their global validity have remained unanswered. Questions concerning the appropriateness of spherical shell model descriptions for nuclei far from the valley of stability may certainly be raised since it is well known that the model breaks down at the onset of regions of deformation. Can existing mass theories be extended out to the very limits of particle stability? If not, what are the implications associated with the breakdown of existing systematics? In addition to the many interesting questions concerning structure aspects of

exotic nuclei there are equally as many questions related to the dynamical characteristics of hot high-density nuclear systems. A vast preponderance of our current knowledge is restricted to normal nuclear density (ρ_o) and near zero temperature ($T\approx 0$). What then is the equation of state of nuclear matter under extreme conditions of temperature and pressure? Many of the suggested questions could not be answered if not for the emergence of heavy-ion collisions as a viable testing ground for such studies.

Heavy-ion collisions have added a new dimension to the study of nuclear physics by providing accessability to vast new territories lying outside the near-stable, $\rho\approx\rho_o$ and $T\approx 0$ domain. A range of differing experimental efforts have emerged that study nuclear phenomena as a function of one or more of the parameters (T_z, ρ, T). For instance one experimental effort is directed toward the study of beta decay of exotic nuclei which isolates in relative purity the isospin dependence of nuclear systems. Structure and decay investigations of exotic nuclei have already benefiAed greatly from this new branch of physics. Experimental investigations of the dynamical characteristics of such collisions are also under way, yet the lack of detailed theoretical predictions makes the experimental results difficult to interpret.

The primary motivation of this thesis is to ascertain information concerning the production and decay modes of

light neutron-rich nuclei. In addition another objective was to help develop the necessary tools to facilitate beta decay half-life measurements using high-energy heavy-ion beams at NSCL. To accomplish the indicated objective, chapter one deals with the current experimental status of heavy-ion production mechanisms and decay studies followed by the contemporary limits of our understanding of effective interactions. Chapter two will review the shell-model approach to beta decay and an appendix will be provided to discuss the Reaction Product Mass Separator which was developed and used for the decay studies given in chapter 3.

Finally, in chapter four, I will present my suggestions and recommendations for future study using the RPMS in light of the results presented here and availability of different beams at NSCL.

1.2 Heavy Ion Production Mechanisms

There can be no denying that the study of exotic nuclei has experienced a renaissance within the last two decades due chiefly to the advantages associated with high-energy nuclear reactions. Evidence for the prolific nature of high-energy nuclear collisions for the production of exotic nuclei began to take shape in the mid 1960's with the discoveries of ^{8}He, ^{11}Li, ^{12}Be, ^{14}B, and ^{15}B [Ce66, Po65, Po66]. Experiments using high-energy proton spallation of

Uranium extended our knowledge of the sodium isotopes [Th75] past the limits of the s-d shell and in so doing radically modified existing mass theories. Meanwhile, in Dubna heavy-ion transfer reactions produced nearly 30 previously unobserved nuclei in the low A region of the Chart of Nuclides [Ar69, Ar70, Ar71a, Ar71b]. This work was extended at Orsay using ^{40}Ar on ^{238}U at 6.6 MeV/A and resulted in the observation of 4 new isotopes [Au79]. As accelerator technology improved, high-energy heavy-ion beams became available to the physics community for the production of exotic nuclei. The first experiments utilizing high-energy heavy-ion beams for the production of exotic nuclei began in the late 1970's at the Lawrence Berkeley Laboratory (LBL) [Sy79] using an ^{40}Ar beam at 205 MeV/A. Within a year's time, another experiment utilizing a rare ^{48}Ca beam again at LBL demonstrated the existence of 14 new isotopes [We79]. Figure 1-1 illustrates the present day boundaries associated with the light neutron-rich nuclei and indicates some of the major contributors to establishing their particle stability.

Concurrent with these experimental investigations, schematic models describing the collision of two heavy ions began appearing in an effort to resolve the observed differences between high and low-energy heavy-ion phenomena. A large class of these models took as their foundation

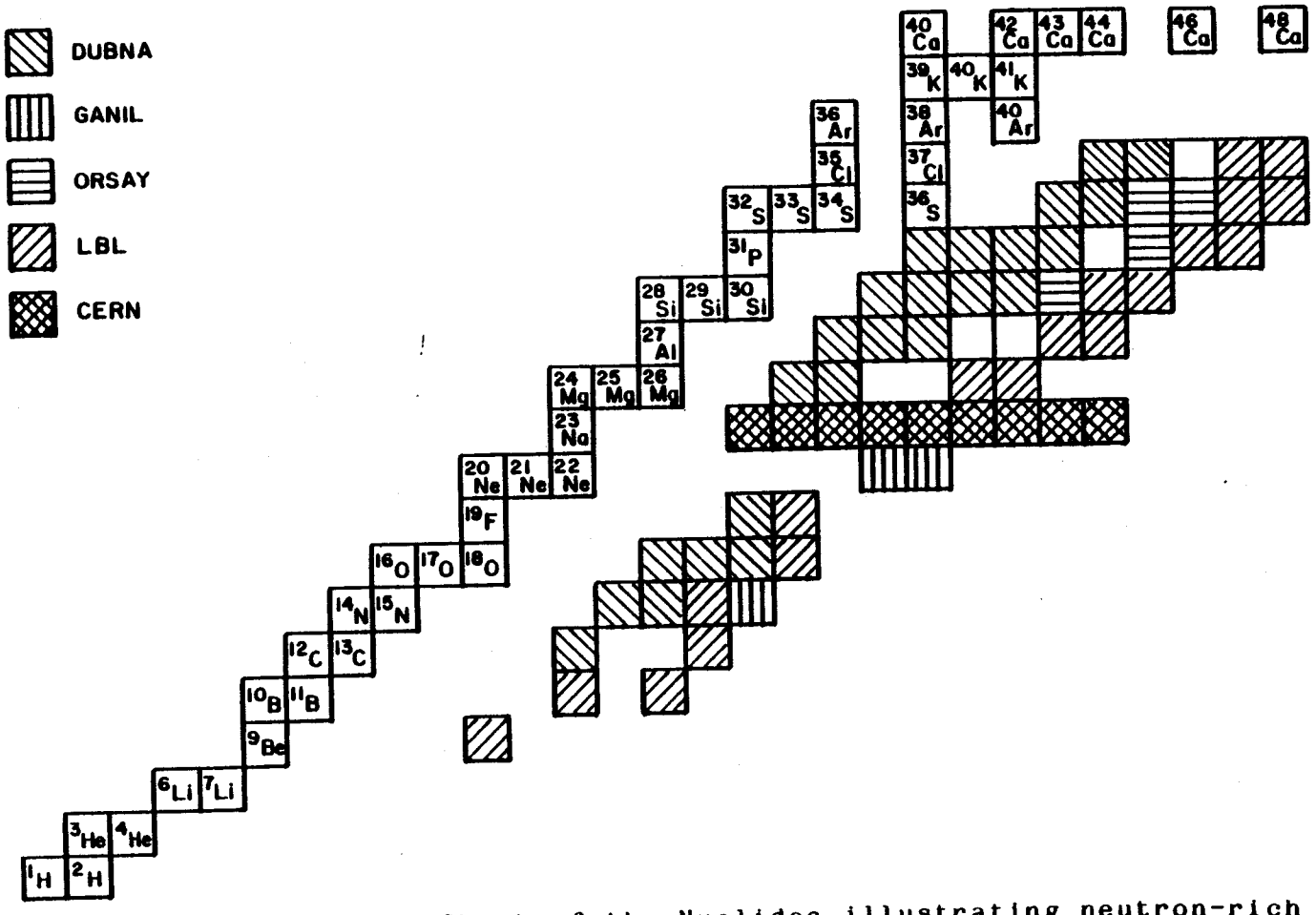

Figure 1-1. Chart of the Nuclides illustrating neutron-rich nuclei whose particle stability has been established (grouped according to the laboratory where the measurement was made).

classical physics thereby describing heavy ions as 'macro'-entities composed of member nucleons. This classical treatment relied on the impact parameter to describe the collision dynamics and the resultant aftermath of nuclei.

It was found that a large percentage of the observed heavy-ion phenomena could be explained by a relatively few number of reaction mechanisms whose boundaries were dependent on the projectile energy and impact parameter of the collision [Sc79] (see figure 1-2). Of the reaction mechanisms illustrated in this figure, fragmentation and deeply-inelastic transfer have proven exceptionally prolific in the production of neutron-rich nuclei as discussed earlier. The relative ability of fragmentation compared to deeply-inelastic mechanisms for the production of exotic nuclei can be seen in figure 1-3. The basic difference between fragmentation and deeply-inelastic mechanisms for the production of exotic nuclei resides in the dependence of the target nucleus. At lower energies where the collision time is longer than the transit time of a nucleon at the Fermi level, the nuclei respond coherently during the collision characteristic of a mean field interaction [Ne78]. Therefore, during a deeply-inelastic collision, neutrons will migrate from the more neutron-rich target nucleus into the projectile nucleus until the N/Z ratio of each member equals the N/Z ratio of the composite system. This proves advantageous since it is possible to produce nuclei having a greater number of neutrons than the original projectile

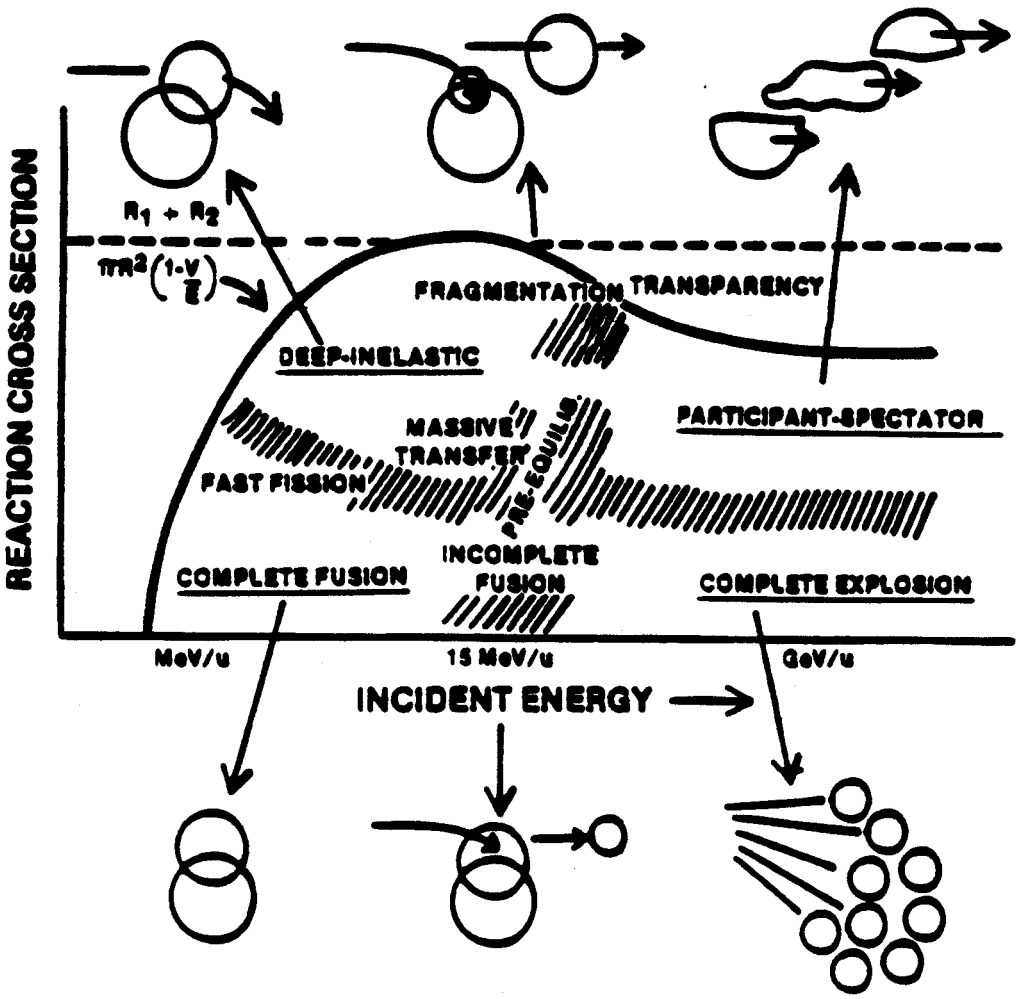

Figure 1-2. Schematic illustration of heavy-ion collision mechanisms as a function of reaction cross-section (equivalent to impact parameter) and bombarding energy.

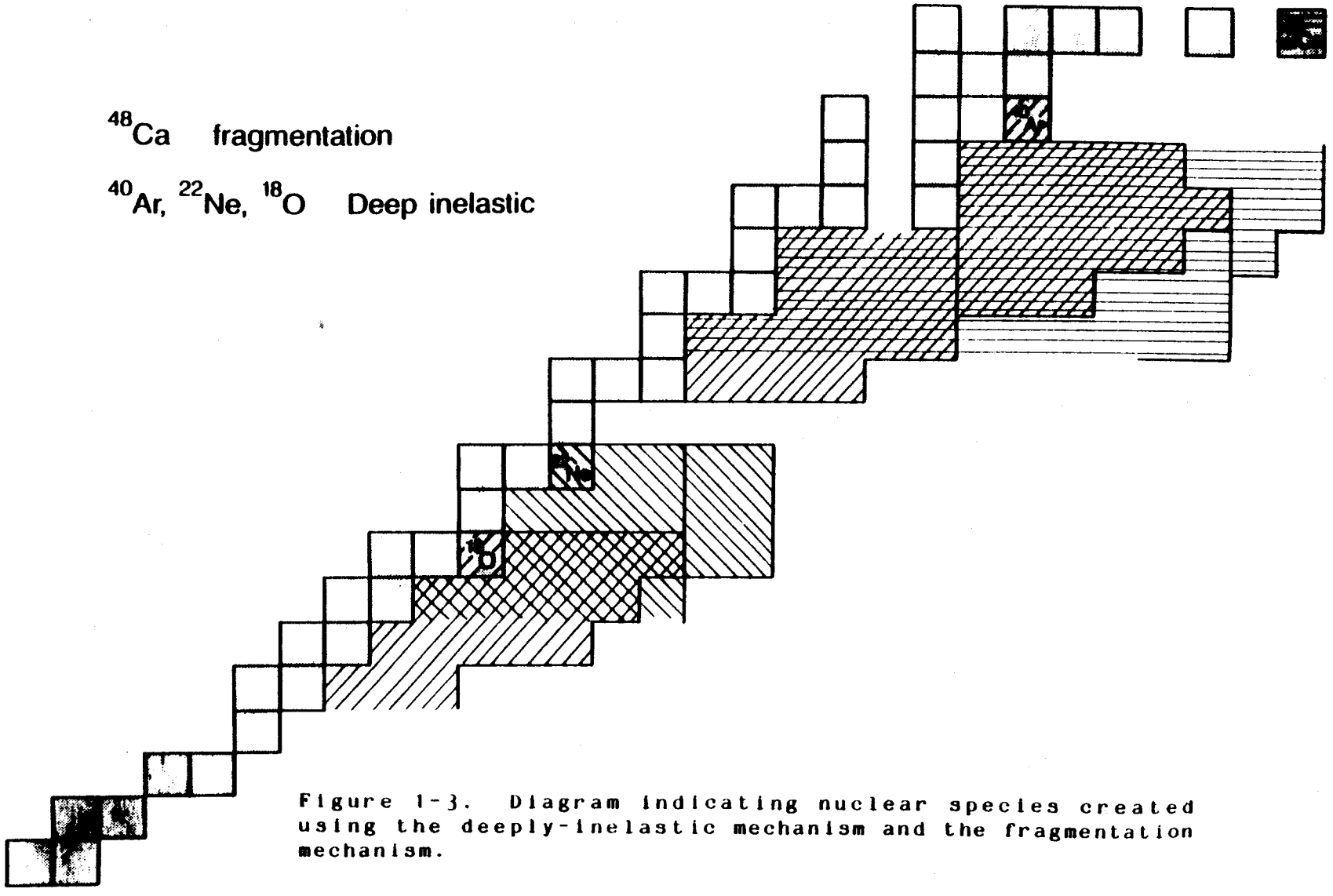

Figure 1-3. Diagram indicating nuclear species created using the deeply-inelastic mechanism and the fragmentation mechanism.

which is not the case for projectile fragmentation. However, if high-energy 'exotic' beams are available, fragmentation has definite advantages over the deeply inelastic mechanism for the production of exotic nuclei. These advantages are:

i) The use of thicker targets can enhance the yield of exotic nuclei by $\approx 10^3$ [Sc79].

ii) Greater kinematic focussing at these energies directs a larger fraction of the total yield into a tight, forwardly-directed cone [Gr75] proving more compatible with the solid-angle characteristics of existing spectrometers.

iii) The energy distribution of projectile fragments is observed to be narrow [Vi79] reducing the required momentum transmission of the spectrometer system.

Combining the advantages given in i) and ii) result in a factor of 10^6 improvement for fragmentation mechanisms when compared to deeply-inelastic mechanisms. Quantitative estimates of the isotopic cross-sections for projectile fragmentation can be obtained using the fireball model [We76, Go77].

The fireball model describes a heavy-ion collision in terms of a two (three) stage abrasion-ablation (-FSI) process as shown in figure 1-4. The peripheral collision between a high velocity projectile and stationary target results in the formation of three entities

i) Target spectator

ii) Projectile Spectator

iii) Participant

The model relies on the impact parameter to determine the number of nucleons in each of the three final state entities by calculating the volume overlap between the projectile and target nuclei. The projectile spectator (representing the exotic isotope) has nearly the same velocity as the original beam except for the energy required to break the nuclear bonds associated with the abraded nucleons as will be discussed in chapter 3. The number of nucleons remaining in the projectile fragment is given by

$$A_{ps} = A_p[1-F(\nu,\beta;s)] \qquad (1-1)$$

where $F(\nu,\beta;s)$ represents the volume sheared away from the incident projectile during impact. The dimensionless

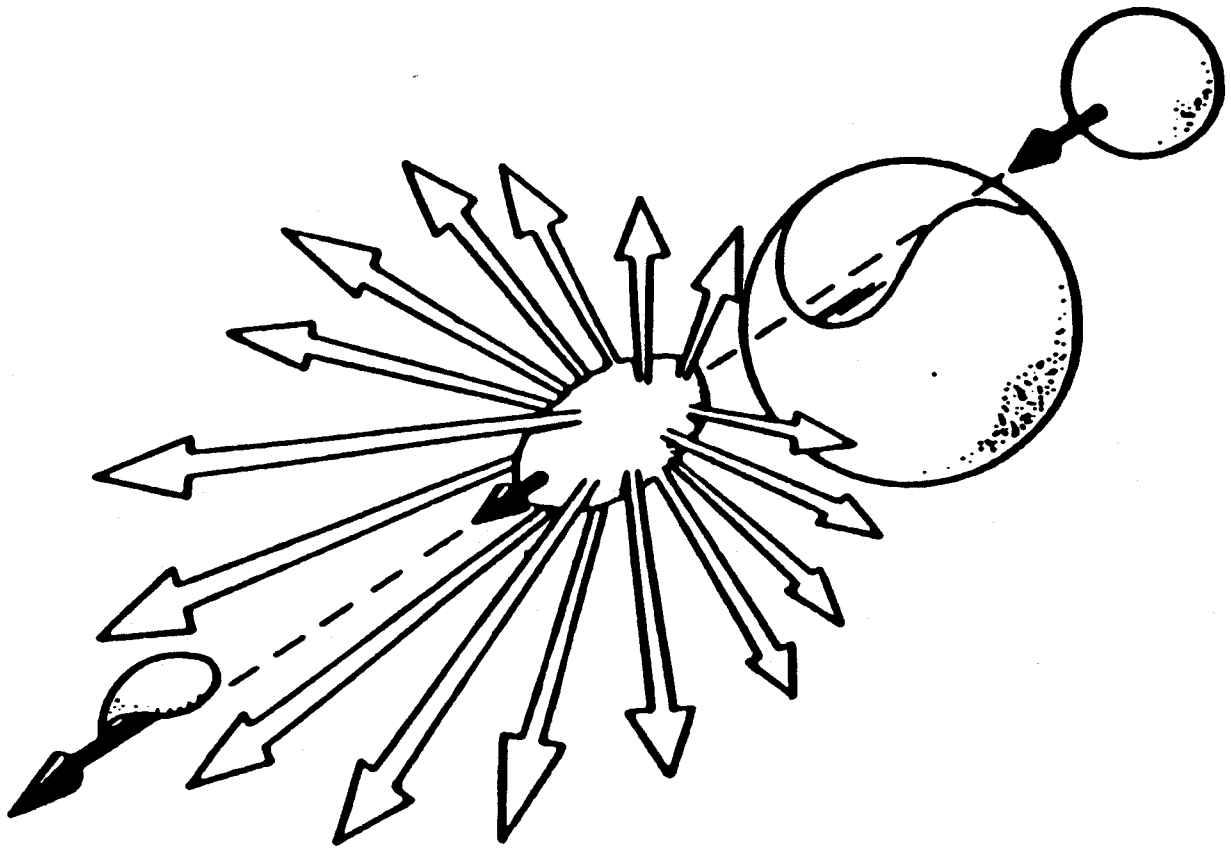

Figure 1-4. Conceptual illustration of the participant-spectator picture using a reaction geometry taken from the fireball model. The overlap region corresponds to the "hot" participant region whereas the projectile and target remnants represent cooler objects.

parameters ν and β specify the relative size and impact parameter characterizing the collision while s signifies a shape dependence. If both ions are assumed spherical with sharp radii, four differing functional forms for $F(\nu,\beta)$ result depending on the region in ν-β space describing the collision (see figure 1-5)

$$F_I = [1-(1-\mu^2)^{3/2}][1-(\beta/\nu)^2]^{1/2} \tag{1-2}$$

$$F_{II} = 3/4(1-\nu)^{1/2}\left(\frac{1-\beta}{\nu}\right)^2 -$$

$$1/8\left(3\left(\frac{1-\nu}{\mu}\right)^{1/2}-[1-(1-\mu^2)^{3/2}][1-(1-\mu)^2]^{1/2}\right)\left(\frac{1-\beta}{\nu}\right)^3$$

$$F_{III} = 3/4(1-\nu)^{1/2}\left(\frac{1-\beta}{\nu}\right)^2-[3(1-\nu)^{1/2}-1]\left(\frac{1-\beta}{\nu}\right)^3$$

$$F_{IV} = 1$$

where

$$\nu = \frac{R_T}{R_p + R_T} \tag{1-3}$$

$$\beta = \frac{b}{R_p + R_T}$$

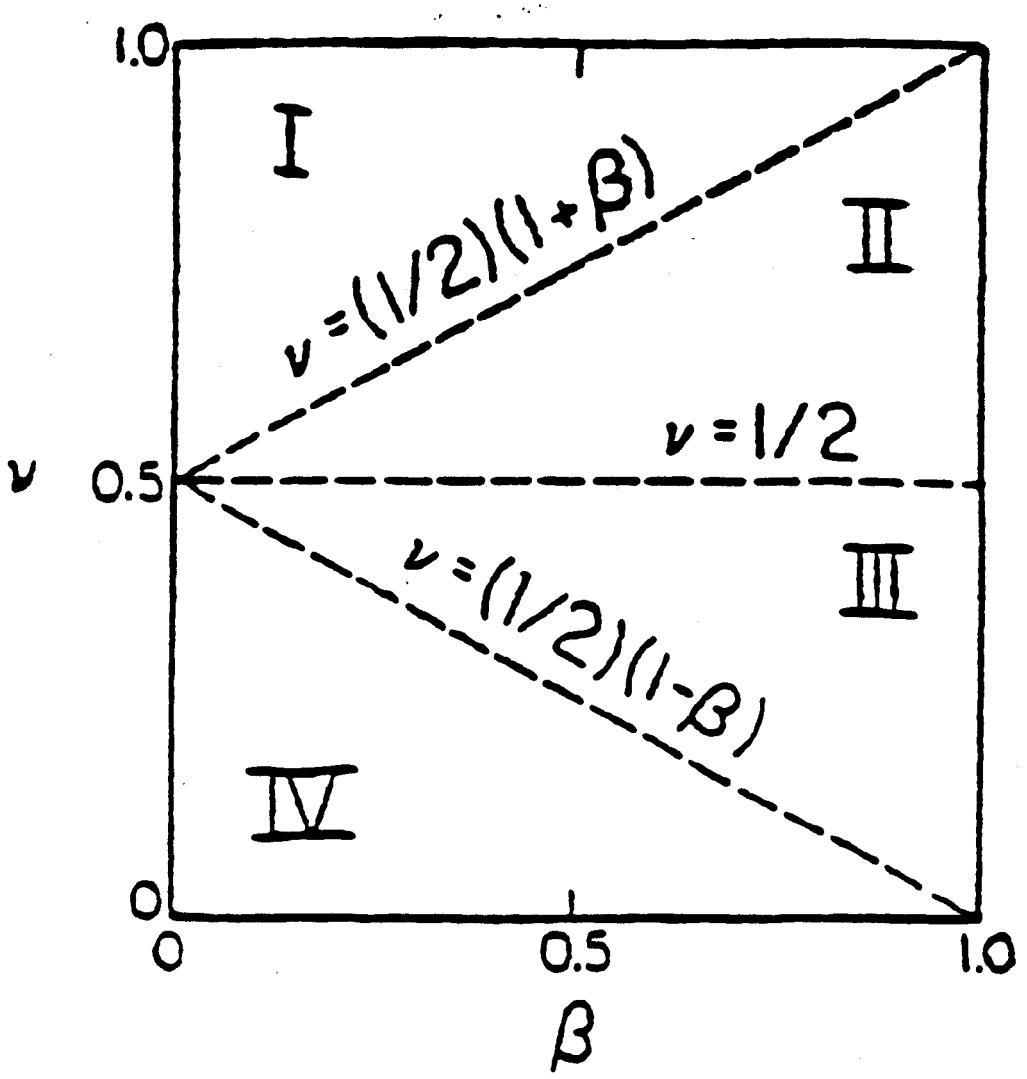

Figure 1-5. Schematic drawing illustrating the different regions associated with a heavy-ion collision as a function of the normalized impact parameter β.

$$\mu = \frac{R_T}{R_p}$$

The different regions in ν-β space are interpreted physically as

I) A cylindrical hole is gouged in the nucleus A_p (which is larger than A_T)

II) A cylindrical channel is gouged in A_p, with a radius smaller than that of A_p.

III) A cylindrical channel is gouged in A_p, with a radius larger than that of A_T.

IV) All of A_p is obliterated by A_T (whose radius is larger than that of A_p).

Since regions I and IV result in the destruction of the projectile fragment, only regions II and III will be considered. Isotopic cross-sections may then be calculated using

$$\sigma(Z,A) = C(Z,A)\sigma(A) \qquad (1\text{-}4)$$

where

$$\sigma(A) = \pi\{[b(A+0.5)]^2 - [b(A-0.5)]^2\} \qquad (1\text{-}5)$$

and the function C(Z,A) describes the ground-state proton-neutron correlations in the projectile just before impact. Two differing dispersion relations were used in the isotopic cross-section calculations with figure 1-6 employing a hypergeometric dispersion relation [Ra77] while figure 1-7 represents the isotopic cross-sections resulting from the Giant-Dipole-Resonance dispersion relation [Mo78]. The results indicate relatively large isotopic cross-sections for the abrasion stage however, the ablation stage will act to reduce the primary distributions. The exact amount of this reduction requires detailed information on the fragments excitation energy and its angular momentum. One popular prescription used to predict the fragment's excitation energy involves calculating the difference in surface area between the abraded fragment and that corresponding to a sphere having the same volume. Multiplying by the surface energy coefficient 0.9 MeV/fm^2 predicts the excitation energy as shown in figure 1-8. The resulting values for low-mass fragments are not very realistic and generally do not predict enough energy for nucleon emission. Furthermore, the theory assumes that this energy has equilibrated throughout the entire fragment which also represents a questionable assumption. At relativistic incident energies, the model assumes that angular momentum

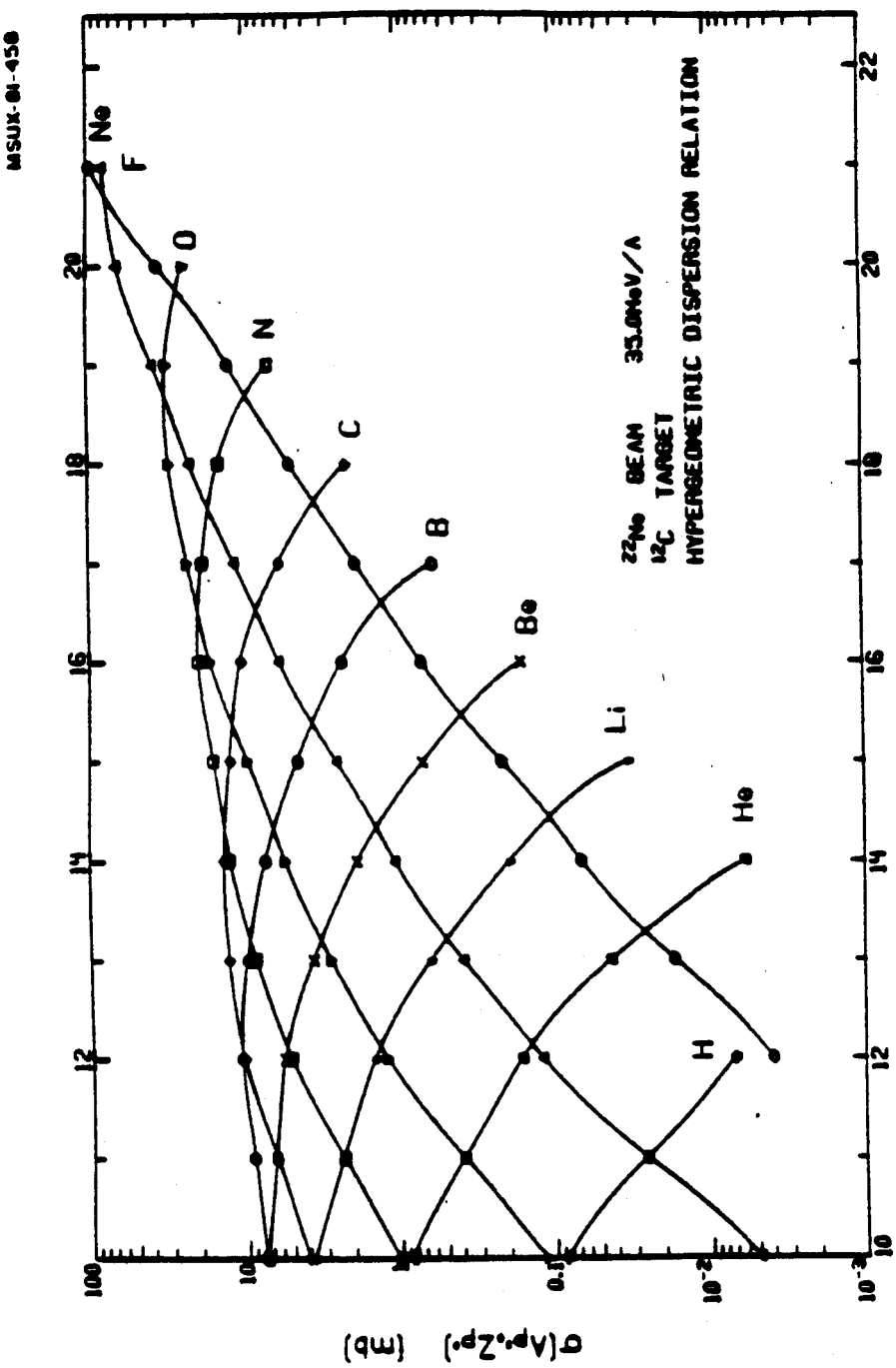

Figure 1-6. Isotopic cross-sections (before the ablation stage) calculated with a hypergeometric dispersion relation. The fireball model was used where the size of projectile and target nuclei are given by πr^2 ($r = 1.2 \times A^{0.333}$ fm)

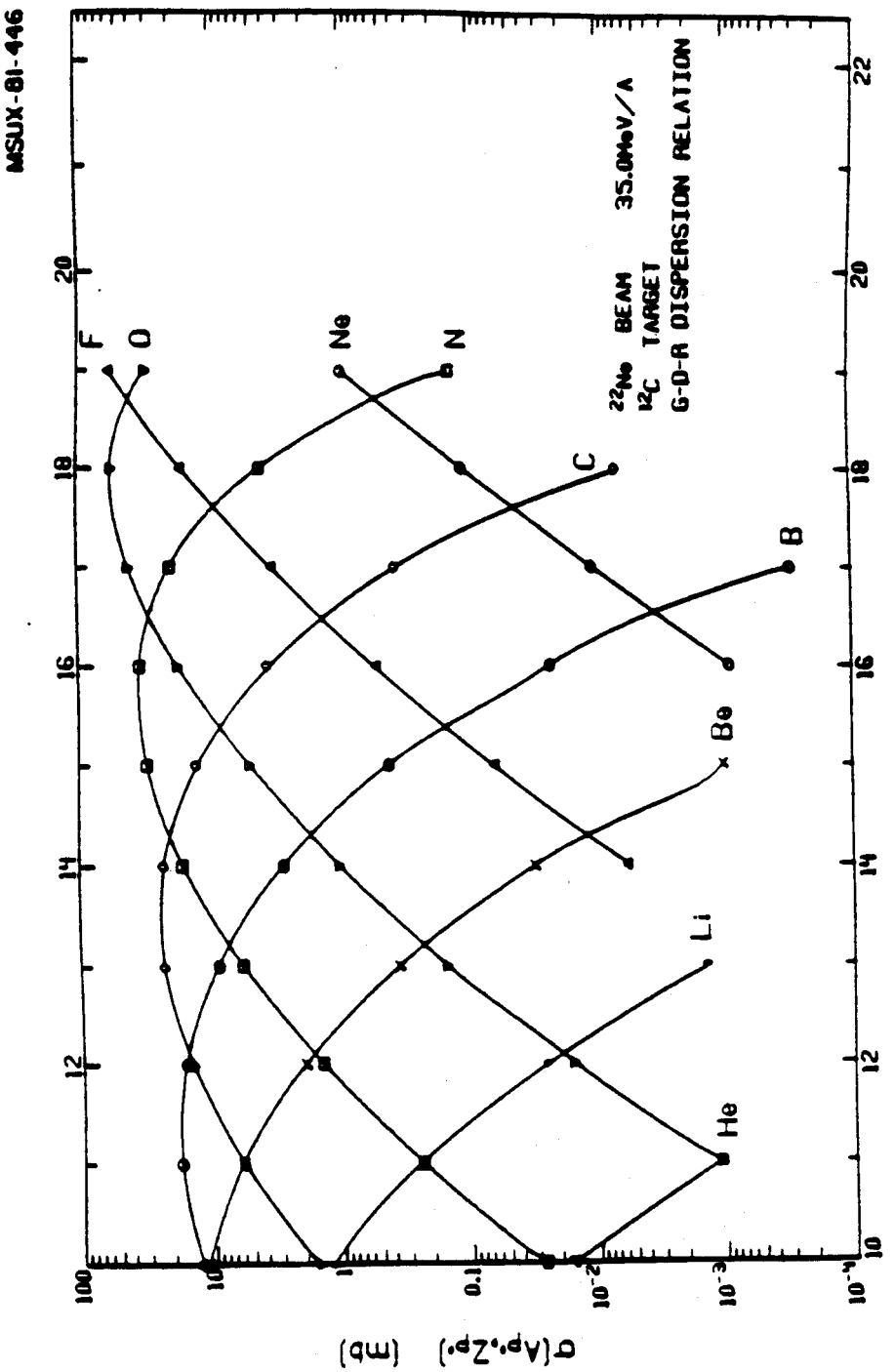

Figure 1-7. Isotopic cross-sections (before the ablation stage) calculated using the Giant-Dipole-Resonance dispersion relation. The fireball model was used where the size of the projectile and target nuclei are given by πr^2 where ($r = 1.2 \times A^{0.333}$ fm).

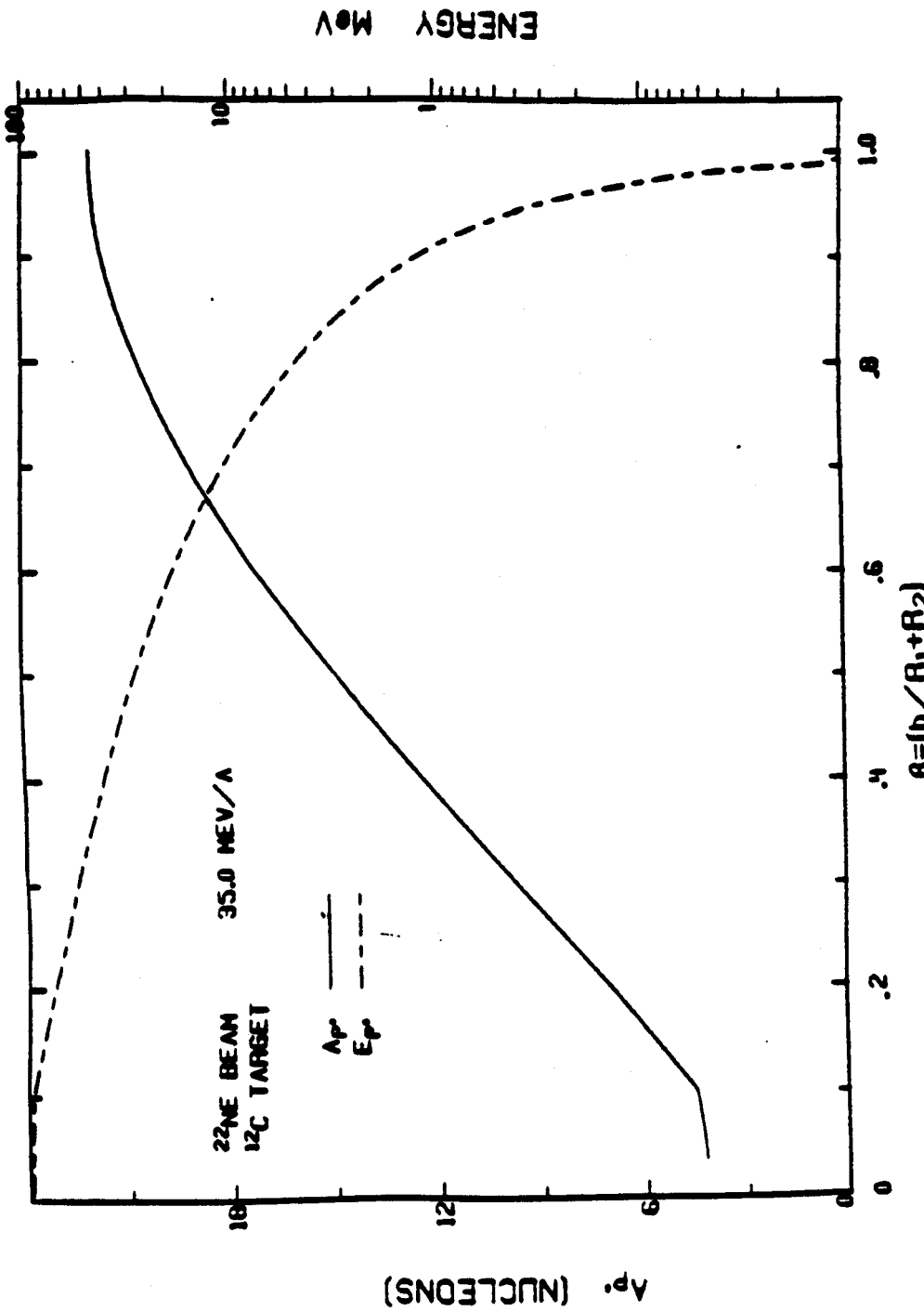

Figure 1-8. Calculated values of the excitation energy and number of nucleons remaining in the projectile spectator as a function of the normalized impact parameter β using the fireball model.

has not been acquired by the projectile fragment. The remaining step would be to use something like an evaporation code to predict the particle emission.

In concluding, we mention that two heavy-ion mechanisms exist which provide favorable yields of exotic nuclei. Fragmentation seems preferable to deeply-inelastic transfer due to reasons discussed previously. A fireball model was used to describe what occurs during fragmentation and then used to predict isotopic cross-sections. Although models exist which can predict the ablation stage of a collision they are generally quite poor and contain nonverifiable assumptions associated with the magnitude and distribution of excitation energy. Thus in practice it has become standard to reduce the primary yields by a factor of ten to estimate the secondary yields [Mo80].

1.3 Decay studies

Until the late 1960's, beta decay data was limited to nuclei lying relatively close to the valley of stability. This limitation was imposed by the lack of adequate production mechanisms capable of providing sufficient yields of exotic nuclei so that their decay modes could be studied. A significant contribution to the study of decay properties of exotic nuclei occurred in the late 1960's when high-energy proton spallation reactions were used to produce large quantities of neutron-rich nuclei. Using an intense

beam of 24 GeV protons from the CERN proton synchrotron on targets of Iridium and Uranium resulted in half-life determinations of ^{11}Li and $^{27-31}$Na [K169]. Coupling the large production cross-sections associated with spallation reactions with thick targets and intense beams resulted in high yields of neutron-rich nuclei out to the very limits of the sd shell. Experimental half-life determinations were limited to alkali elements (Li,Na,K) since the technique employed required the isotopes to diffuse through a heated graphite foil where they would undergo surface ionization, reacceleration and finally identification using a mass spectrometer. Continued improvements and modifications of the accelerator and mass spectrometer resulted in the half-life of ^{32}Na (f-shell nuclei) and the observation of $^{48-50}$K [K172]. More detailed experiments measuring delayed neutron emission probabilities (P_n), beta Q values, and various J^{π} assignments were undertaken for the same sodium isotopes [Ro74]. Pushing this work to the limit half-life measurements for the daughter nuclei $^{29-31}$Mg were obtained at the same facility [De79]. Concurrent with the work performed at CERN, a group at Brookhaven National Laboratory (BNL) undertook the study of $T_z = +5/2$ sd shell nuclei [A176]. Using heavy-ion beams of ^{13}C, ^{18}O, and ^{19}F, they were able to produce and measure masses, half-lives and spectroscopic properties of ^{21}O, ^{23}F, ^{29}Mg, ^{31}Al, ^{33}Si, and ^{35}P

representing the entire set of T_z= +5/2 nuclei contained within the sd shell. In the lower mass region of the chart of nuclides, the ^{10}Be(t,p) reaction was used to generate ^{12}Be and its half-life was then deduced as ≈24.0 ms [A178]. Similarly, using 31 MeV ^{6}Li ions on a ^{10}Be enriched BeO target resulted in the half-life measurement of ^{14}B [A174].

Quite recently, another significant advance occurred which demonstrated a tremendous potential for extending decay studies out to the neutron-drip line for light nuclei. This new reaction mechanism essentially turned the spallation mechanism around and used high-energy heavy-ions as the projectile. The first half-life measurements employing fragmentation of high-energy heavy-ion beams were obtained at Lawrence Berkeley Laboratory (LBL) using ^{40}Ar at 285 MeV/A on ^{9}Be. The experiment resulted in half-lives for 8 neutron-rich nuclei two of which (^{22}O and ^{32}Al) were first time measurements [Mu82]. The new technique demonstrated the potential benefit of heavy-ion beams for the study of exotic nuclei, in particular, their decay modes. Recently, within the last year the half-life of ^{15}B was measured to be 11.0 ± 1.0 msec. using an 84 MeV/A ^{18}O beam on a ^{12}C target [Du84].

Limitations on the heavy-ion approach were mainly due to low beam intensities and inadequate isotope separation.

The first results obtained at Michigan State University, (presented in chapter 3), verify the tremendous capability of heavy-ion reactions for the study of light neutron-rich nuclei and paint a promising picture for future studies. In addition to the MSU group, a Bordeaux-Ganil collaboration is actively involved in decay studies and should provide adequate competition in extending measurements well out toward the neutron drip line [La84].

1.4 Effective Interactions

One of the primary goals of nuclear science is the determination of the effective nucleon interaction in the context of the nuclear many-body problem. The achievement of this goal is contingent upon acquisition of detailed experimental information related to how the free nucleon interaction must be modified in the presence of other nucleons. Two schools of thought have emerged as to the most advantageous method to be employed in the pursuit of this goal. The first such school advocates a phenomenological approach involving the determination of one- and- two- body matrix elements, (comprising the model Hamiltonian), through a numerical least squares fitting procedure [Ch76]. The effective Hamiltonian is generated in a truncated spherical shell model basis through the use of a selected set of empirical energy level data taken from nuclei believed to be well described by this restricted Hilbert space. The

ultimate utility of such an approach can be determined when experimental data emerges which may be compared to the corresponding predicted features calculated with this interaction. Although this effective interaction has been specifically tailored to describe energy level data of nuclei contained deep within this restricted model space, other observables such as spectroscopic factors, ft values, magnetic and electric transitions, and various magnetic and electric moments will provide an independent check on the quality of the resultant interaction [Br80a,Br80b]. When this comparison is made, one generally observes remarkable agreement for nuclei not far removed from those used to generate the Hamiltonian. This outstanding agreement is of course at the expense of introducing a sizable number of free parameters.

In contrast, the second school of thought utilizes an empirically determined nucleon-nucleon interaction which is then modified through the use of many-body mathematical techniques to account for the influence of the nuclear media [Br71]. Although somewhat more fundamental than the aforementioned phenomenological method, (since this method results directly in an eloquent decomposition of the interaction into free nucleon and many-body aspects), this 'realistic' approach is plagued by many difficulties associated with the importance of various Feynman diagrams as well as the procedure for summing them. When comparing overall agreement of the 'realistic' and 'phenomenological'

predictions to existing data, one must concede the greater predictive capability to the 'phenomenological' approach. Thus, it is in the context of the 'phenomenological' approach that the salient features displayed by nuclei far from stability will be discussed. The remainder of this section will be devoted to the description of such a phenomenological shell model technique.

Two basic features of this empirical shell model approach must be elucidated namely, the choosing of an appropriate model Hamiltonian and the selection of a suitable truncated shell model space in which the model Hamiltonian can be diagonalized. The model Hamiltonian employed consists of one- and- two- body matrix elements having the following form

$$H = \sum \varepsilon_i a_i^\dagger a_i + \sum V_{klmn} a_k^\dagger a_l^\dagger a_m a_n \qquad (1.6)$$

where

ε_i = single particle energies

V_{klmn} = two-body matrix elements

$a_i^\dagger$ = single nucleon creation operator (1.7)

a_i = single nucleon annihilation operator

Since the matrix elements of the model Hamiltonian must be adjusted to fit energy level data, one is required to choose a suitable basis set in which the energy diagonalization can

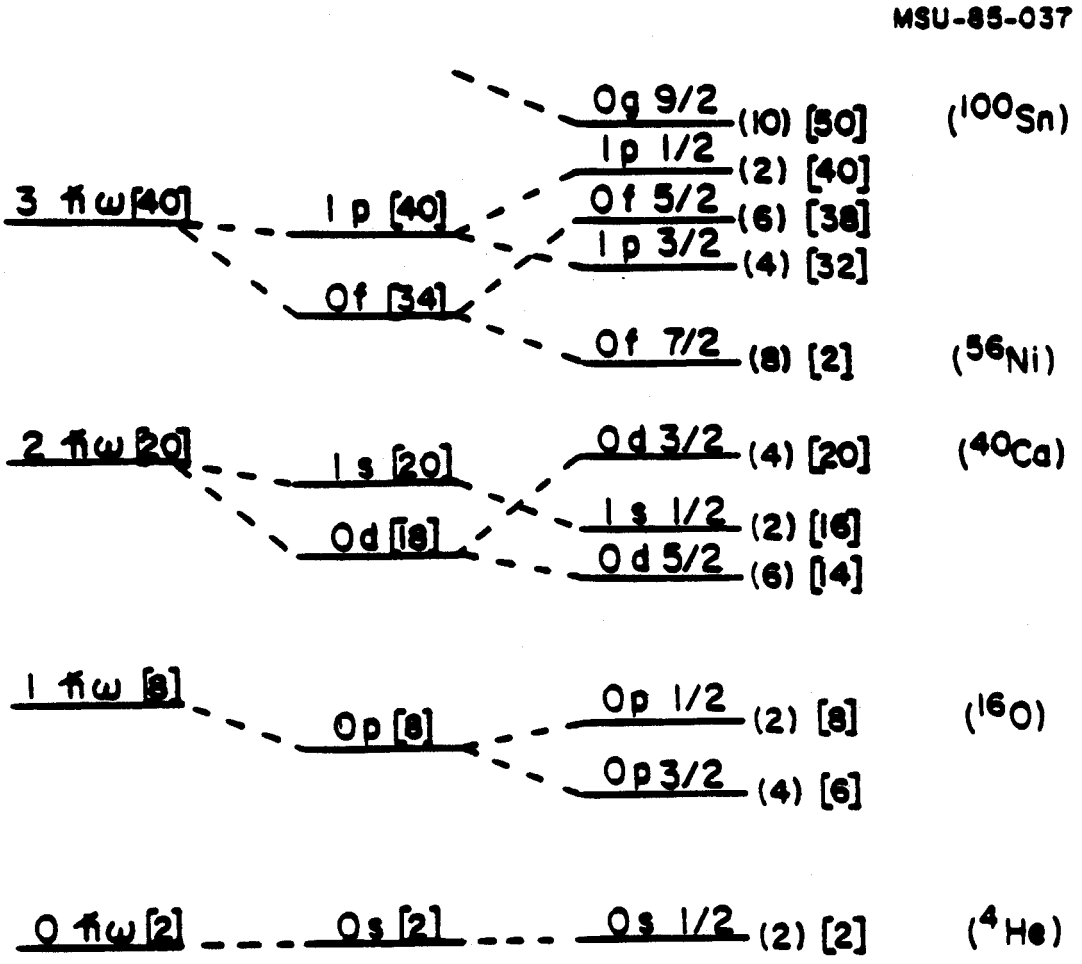

Figure 1-9. The extreme single particle orbits obtained by solving the non-relativistic Schrodinger equation with a Woods-Saxon plus spin-orbit potential.

be done. Futhermore, due to computational limitations [Se68], one is forced to choose a finite subset of the complete basis set and it is within this subset that the wavefunctions will be expanded. Thus, it becomes imperative to make a judicial choice of this subset if one is to have confidence in the resulting set of wavefunctions. The extreme single particle orbits ($0s_{1/2}$, $0p_{3/2}$, $0p_{1/2}$, $0d_{5/2}$, ...), obtained through solving the non-relativistic Schrodinger equation with a Woods-Saxon plus spin-orbit potential, supply a suitable complete basis set (see figure 1-9). This basis set exhibits natural energy partitions associated with shell closures which may be exploited in making the proper choice of truncated model space. The empirical shell model approach requires a three way subdivision of the complete basis set

i) closed core
ii) active orbits (1.8)
iii) forbidden higher lying orbits

Thus, a nucleus characterized by A nucleons will have $A-A_c$ valence nucleons distributed among N active orbits in such a way as not to violate the Pauli principle, where A_c nucleons are contained within an inert core. An individual valence nucleon which occupies a specific shell model orbit will interact with the core nucleons through the one- body matrix

elements which depend simply on the orbit quantum numbers. Likewise, the valence nucleons interact amongst themselves through a residual interaction characterized by the remaining two- body matrix elements. These two- body matrix elements depend on the individual j's of each particle as well as the total J and T (and in one case also depends on A). For example, in a full s-d shell calculation, one assumes an inert O^{16} core with valence nucleons distributed among the active orbits ($0d_{5/2}, 1s_{1/2}, 0d_{3/2}$) such that the higher lying orbits ($0f_{7/2}, 0g_{9/2}, 1p_{3/2}, \ldots$) are inaccessible. The corresponding Hamiltonian consists of 3 single particle energies plus 63 two body matrix elements which are fit to 200-300 well-known energy levels found in nuclei near the interior of the model space. The resulting effective interaction is then used to generate a family of wavefunctions $\psi^{nTJ\nu}$ where

n = number of nucleons occupying the active orbits $(A-A_c)$

J = total angular momentum (1.9)

T = total isobaric spin

ν = counting index which identifies a particular eigenstate of the nJT set

These wavefunctions then comprise the entire predictive content of this empirical shell model approach and are used to compute other observables against which experimental data may be compared. Detailed calculations for beta decay will be presented in chapter 2 of this thesis using wavefunctions obtained from various 'phenomenological' interactions as discussed above.

Chapter 2 - Theory of Beta Decay and the Shell-Model

2.1 Introduction to Fermi and Gamow Teller Beta Decay

Our current understanding of both the strong and weak interactions has benefited greatly from the study of nuclear beta decay. Since its first observation, nuclear beta decay has represented a formidable curio which, like many curios, resulted in a substantial advance in our understanding of nature. From the unexpected observation of the continuous energy spectrum characterizing the emitted beta particles, which resulted in the prediction and eventual observation of the elusive neutrino, to the role played in the downfall of parity conservation [Le56,Le57,Wu57], nuclear beta decay has made a profound mark on contemporary nuclear science. Furthermore, nuclear beta decay holds the promise of providing a testing ground from which the neutrino rest mass may be extracted [Ma69], which if accomplished would have repercussions on the cosmological scale [St79]. In addition, beta lifetime measurements prove extremely important in the determination of stellar evolution since they represent the slowest process in the primary nuclear burn cycle. As indicated, the importance of beta decay to the discipline of physics is multifaceted making it impossible to accurately describe all aspects of this interdependence in a limited amount of space. Therefore, the intention of this

introduction is to discuss the salient features of beta decay and how measurements of its associated properties will contribute to our knowledge of nuclei, particularly nuclei far from stability.

Nuclear beta decay may be coined a semi-leptonic process which involves the interaction of leptons with hadrons and, as such, provides a unique setting in which to study the coupling of leptonic and hadronic degrees of freedom. The elementary processes thought to occur in nuclear beta decay proceed in one of the following manners

$$n \rightarrow p^{+} + e^{-} + \bar{\nu}_{e} \qquad \text{(electron emission)} \qquad (2.1)$$

$$p^{+} \rightarrow n + e^{+} + \nu_{e} \qquad \text{(positron emission)} \qquad (2.2)$$

where the electron neutrino ν_e acts as a silent partner in the beta decay process except that it carries away 1/2 $\hbar$ of spin and an energy which is determined utilizing Fermi-Dirac statistics to describe the three body final state. The formalism developed for handling a three body final state using Fermi-Dirac statistics was able to describe the shape of the observed beta spectrum. Likewise, it is the deviation from the $m_{\nu} = 0$ spectrum shape which proves to be a sensitive test for the determination of the neutrino rest mass. The first of these two processes represents the decay of the

free neutron which has an observed half-life of 623.6 ± 6.2 seconds and provides information on the axial vector coupling constant g_a. The second process, representing the decay of the free proton, is energy prohibited by approximately 1800 KeV due to the greater rest mass energy on the right side of equation (2.2). Although nature does not permit the free proton beta decay, this decay can occur in the presence of a nucleus since the proton may draw the necessary energy from the surrounding nuclear medium. However, this energy exchange mechanism quite naturally introduces nuclear degrees of freedom into the problem which could wash out the resemblance between nuclear beta decay and the elementary processes given in equations (2.1) and (2.2). Observation of super-allowed $J^{\pi} = 0^{+} \rightarrow 0^{+}$ (T=1) beta transitions indicate that this is not the case for Fermi beta decay. On the other hand, observation of Gamow-Teller transitions does reveal a strong influence of the nuclear medium on the corresponding lifetimes. This discussion of beta decay will be limited to only super-allowed and allowed decay mechanisms which are characterized by the following selection rules and comparative half-lives

$$\begin{aligned} &\text{Fermi Transitions} \qquad 2.9 \leq \log ft_{1/2} \leq 3.7 \\ &\Delta J = 0 \\ &\Delta \pi = \text{no} \\ &\Delta T = 0 \end{aligned} \tag{2.3}$$

$$\Delta T_z = \pm 1 \quad \begin{cases} + & \text{electron emission} \\ - & \text{positron emission} \end{cases}$$

Gamow-Teller Transitions $\qquad 4.4 \leq \log ft_{1/2} \leq 6.0$

$\Delta J = \pm 1, 0 \qquad (0 \rightarrow 0 \text{ forbidden })$

$\Delta \pi = \text{no}$

$\Delta T = \pm 1, 0 \qquad (2.4)$

$$\Delta T_z = \pm 1 \quad \begin{cases} + & \text{electron emission} \\ - & \text{positron emission} \end{cases}$$

The formalism developed for the study of allowed beta decay classifies transitions according to pure Fermi, pure G-T, or a mixture of both types of decay. Comparative half-lives of allowed beta transitions may be written in terms of Fermi and G-T matrix elements

$$ft_{1/2} = \frac{K}{g_v^2 B(F) + g_a^2 B(GT)} \qquad (2.5)$$

where

$B(F)^{1/2}$ = Fermi Decay Matrix Element

$B(GT)^{1/2}$ = Gamow-Teller Decay Matrix Element

g_v = Vector coupling constant $\qquad (2.6)$

g_a = Axial vector coupling constant

$$\kappa = \frac{2\pi^3(\hbar c)^7 \ln 2}{(m_e c^2)^5 c} = (1.77541 \pm 0.00004)\times 10^{-94} \text{ erg}^2\text{- cm}^6\text{-sec}$$

This representation requires the determination of two constants g_v and g_a which is best accomplished by measuring the lifetimes of $J^\pi = 0^+ \rightarrow 0^+$ (T=1) Fermi transitions which yield a value for g_v along with measurements of the free neutron lifetime resulting in a value for $g_v^2 + 3g_a^2$. It should also be mentioned that it has become customary to decompose g_v into yet more fundamental constants

$$g_v^2 = G^2\cos^2(\theta_c) \tag{2.7}$$

where

$$G = \text{Weak Interaction Coupling Constant} \tag{2.8}$$

θ_c = Cabbibo angle

The constant G is generally determined from the decay of the $\mu^\pm$ and $\cos(\theta_c)$ reflects the nuclear media contribution with a value approaching one, implying less contribution of the nuclear degrees of freedom. The most recent values of these two terms are [Du83]

$$G = (1.16632 \pm 0.00002)\times 10^{-5} \text{ GeV}^{-2} \tag{2.9}$$

$$\cos(\theta_c) = 0.9748 \pm 0.0003 \qquad (2.10)$$

It has become apparent that the study of Fermi beta decay reveals important information concerning the vector nature of the weak interaction while also providing detailed information on the isospin mixing properties of the Coulomb-nuclear interaction.

Next, we focus our attention on G-T decays which exhibit more complicated phenomena involving participation of many nuclear degrees of freedom and resulting in a substantial altering of the elementary processes. Gamow-Teller transitions involve both a spin and isospin changing operator, whereas Fermi transitions simply involve an isospin rotating operator. Thus G-T decays will provide information on the spin mixing components of the nuclear interaction which are believed to be comparatively large in view of the fact that the nuclear interaction seems to have little or no isospin mixing capability. Futhermore, G-T transitions are valuable in evaluating the resemblance between initial and final state wave functions which may have differing J^{π} and T. Gamow-Teller transition matrix elements are observed to vary substantailly for differing mother-daughter systems which is not the case for Fermi transition matrix elements which almost always exhibit only small deviations from perfect overlap. Before meaningful

structure information can be extracted from a comparison between predicted and measured strengths, one must first address the question of $\sigma\tau$ renormalization arising because of model assumptions as will be discussed in detail later. For shell model calculations involving the full s-d shell, this renormalization factor is seen to be fairly constant having a value of approximately 50% as confirmed by (p,n) reactions [Go80].

One may well expect that G-T beta decay will provide information on the coupling of low lying single particle states to this high lying collective state. Likewise, G-T decay provides an easily accessible test of empirical shell model calculations which employ the isospin formalism. The remaining portion of this chapter will deal quantitatively with the shell model approach to allowed beta decay and finish by presenting the predicted features of G-T decay for light neutron rich nuclei for a variety of model assumptions.

2.2 Introduction to Shell-Model Formalism

Comparative half-lives of allowed beta transitions, as seen in equation (2.5), may be written in terms of Fermi and Gamow-Teller matrix elements. For computational purposes associated with the empirical shell model approach, it proves conveinent to rearrange the aforementioned equation into the following form

$$t_{1/2} = \frac{C}{[f_v + f_{ec}^F]B(F) + [f_a + f_{ec}^{GT}]B'(GT)} \qquad (2.11)$$

where

f_v = phase space factor for Fermi decay

f_a = phase space factor for Gamow-Teller decay

f_{ec}^F = phase space factor associated with electron capture for Fermi decay

(2.12)

f_{ec}^{GT} = phase space factor associated with electron capture for Gamow-Teller decay

The constant C appearing in equation (2.11) measures the pure Fermi decay strength which, when extracted from $0^+ \rightarrow 0^+$ Fermi transitions in the s-d shell, has the value 6170±4 [Wi78] comparing favorably with previously reported values [Br78,La73,Wi80,Ti78]. The remaining constant $(g_a/g_v)^2$ has been incorporated into the modified Gamow-Teller matrix element B'(GT). The utility of this formulation resides in the complete separation of the structure dependence contained in the matrix elements and the energy dependence

contained in the phase space factors. Futhermore, this decomposition of partial half-lives into Fermi and G-T decay components allows information to be extracted about both the vector and axial vector interactions responsible for allowed beta decay.

Fermi beta decay involves a transition between isobaric analog states (I.A.S.) which, assuming charge independent interactions, are identical. The inclusion of charge dependent interactions breaks this exact analog symmetry through the introduction of isospin mixing and a corresponding coulomb energy shift which may be calculated from the Isobaric Mass Multiplet Equation (I.M.M.E.). This resultant energy shift changes the beta Q-value for the transition requiring modification of the phase space factor while isospin mixing necessitates a correction factor in the Fermi matrix element. Evaluation of the Fermi matrix element is straight forward resulting in

$$B(F) = [T(T-1) - T_{z_i} T_{z_f}]\delta_{if}(1-\varepsilon) \qquad (2.13)$$

where $(1-\varepsilon)=0.995 \pm 0.003$ [Wi78] and represents the deviation from perfect overlap due to isospin mixing. The fact that this value lies close to 1.00 indicates that the symmetry breaking is very weak. As mentioned earlier the resulting energy shift will influence the final state interaction between the leptons and hadrons which is usually

accounted for by introducing small multiplicative factors to the phase space factor [Ko83].

$$\delta_R = \text{energy-dependent terms}$$

$$\Delta_R = \text{energy-independent terms} \qquad (2.14)$$

where these terms correct for the final state electromagnetic interactions which modify the corresponding phase space factors. Furthermore, electron capture is seen to compete with positron decay which introduces atomic degrees of freedom into the problem. This however, does not introduce a large uncertainty into the calculation since the atomic wavefunctions are known with high precision.

This concludes the discussion of super-allowed beta decay and directs the discussion toward Gamow-Teller transitions which characterize the decay of light neutron rich nuclei. The beta decay of neutron rich nuclei does not proceed through the Fermi decay component since the isobaric analog states increase in energy as one decays back toward the valley of stability. Thus the Gamow-Teller decay component represents the only type of allowed decay which simplifies equation (2.11)

$$t_{1/2} = \frac{C}{f_a \, B'(GT)} \qquad (2.15)$$

The determination of the G-T matrix element proceeds from the evaluation of linear combinations of one body matrix elements $D_{j_1 j_2}$ and single nucleon matrix elements $S_{j_1 j_2}$ according to

$$B'(GT)^{1/2} = \frac{1}{\sqrt{2(2j_i+1)}} \begin{pmatrix} T_f & 1 & T_i \\ -T_{zf} & \Delta T_z & T_{zi} \end{pmatrix} \sum D_{j_1 j_2} S_{j_1 j_2} \qquad (2.16)$$

The entire predictive capability of the empirical shell model approach is reflected in the $D_{j_1 j_2}$ elements, which reveal the degree of configuration mixing generated by the model Hamiltonian and are calculated from

$$D_{j_1 j_2} = \frac{\langle \psi_f | | | [a^{\dagger}_{j_1} \otimes a_{j_2}]^{\Delta J=1, \Delta T=1} | | | \psi_i \rangle}{\{(2\Delta J+1)(2\Delta T+1)\}^{1/2}} \qquad (2.17)$$

where the triple bar indicates reduction in both spin and isospin and the wavefunctions are obtained from the empirical shell model approach as explained in section (1.4). The single nucleon matrix elements may be calculated using

$$S_{j_1 j_2} = |g_a / g_v| \langle \rho(n_1 l_1 j_1) | \sigma\tau | \rho(n_2 l_2 j_2) \rangle \qquad (2.18)$$

and reflect the relative efficiency of the G-T operator at converting model nucleons from one single-nucleon state to another. The ratio of the axial vector to vector coupling constants is taken to be

$$|g_a/g_v| = 1.2605 \pm 0.0075 \tag{2.19}$$

which may be determined from the free neutron lifetime and $0^+ \rightarrow 0^+$ Fermi decays [Wi82]. The evaluation of $S_{j_1 j_2}$ follows from knowledge of the aforementioned constant and

$$\langle {}^1/_2 || \tau || {}^1/_2 \rangle = \sqrt{6} \tag{2.20}$$

$$\langle \rho(n_1 l_1 j_1) || \sigma || \rho(n_2 l_2 j_2) \rangle = \sqrt{(2j+1)}\, C^{j_1 j_2}_{l_1 l_2}\, \delta_{l_1 l_2}\, I_{j_1 j_2}$$

$$I_{j_1 j_2} = \int R_{j_1} R_{j_2} r^2 dr \tag{2.21}$$

$$C^{j_1 j_2}_{l_1 l_2} = \left[(-)^{l_1 + {}^1/_2 - j_2} \frac{2\sqrt{j_2 (j_2+1)}}{2l_1+1}\, \delta_{j_1 j_2} \right.$$

(2.22)

$$\left. -(-)^{l_1 + {}^1/_2 - j_1} \left\{ \frac{2(2j+1)}{2l_1+1} \right\}^{1/2} \delta_{j_2, l_2 \pm {}^1/_2}\, \delta_{-j_1, -l_1 \pm {}^1/_2} \right]$$

The resulting free nucleon values of $S_{j_1 j_2}$ for the various active orbits employed in the calculations are given in table (2.1). When the free nucleon values are used along with the $D_{j_1 j_2}$ to calculate partial lifetimes, one observes systematically shorter lifetimes relative to experiment. This 'quenching' of the $\sigma\tau$ strength is believed to originate from a variety of sources such as model space truncation effects which include both core polarization and high lying collective states involving the forbidden orbits [Ma67,Sh74]. Other effects include non-nucleonic degrees of freedom such as delta resonances, mesonic exchange currents and relativistic corrections to the nucleon wavefunctions [Ch71,Ba75,Kh78,Mu73,To79]. The empirical alternative to the exact calculation of this renormalization is to treat the $S_{j_1 j_2}$ as parameters in a least squares fit to experimental values of the G-T matrix elements [Br78]. When this was done for the universal s-d shell interaction (USD) of Wildenthal [Wi82] an orbit independent scale factor of 0.77 emerged, representing a 69% increase in the predicted lifetimes as compared to those obtained using the free nucleon $S_{j_1 j_2}$ values.

The final issue to be discussed concerns the evaluation of the phase space factor f_a which when determined allows the partial half-lives to be calculated

TABLE 2.1

J	J'	L	$S_{J\,J'}$ (Free Nucleon)
$^3/_2$	$^3/_2$	2	-4.747
$^1/_2$	$^1/_2$	0	7.506
$^5/_2$	$^5/_2$	2	8.881
$^5/_2$	$^3/_2$	2	-9.494
$^3/_2$	$^5/_2$	2	9.494
$^1/_2$	$^1/_2$	1	-2.502
$^3/_2$	$^3/_2$	1	7.912
$^3/_2$	$^1/_2$	1	-7.077
$^1/_2$	$^3/_2$	1	7.077

Table 2-1. Single nucleon matrix elements for p-sd shell model orbits.

and compared to existing experimental values. Following the prescription of Wilkinson and Macefield [Wi74], one may obtain phase space factors accurate to within ≈0.5% for nuclei used in this study. Evaluation of the phase space factor starts from the analytic expression for f due to a chargeless point nucleus

$$f_o = (1/60)[2W_o^4-9W_o^2-8]P_o + (1/4)W_o \ln(W_o+P_o) \qquad (2.23)$$

where W_o equals the total electron end point energy (electron rest mass units), $P_o=(W_o-1)^{1/2}$ and higher order corrections are introduced through the multiplicative factors given below

$$\delta_{WM} \ , \ \delta_D \ , \ \delta_R \qquad (2.24)$$

The resulting total phase space factor may then be written as

$$f_a = \delta_D \delta_R \delta_{WM} f_o \qquad (2.25)$$

with the most important phase space correction factor being δ_{WM} which is calculated in the form

$$\delta_{WM} = \exp\left[\sum a_n (\ln E_0)^n \right] \qquad (2.26)$$

the a_n coefficients are given in [Wi74]. These values were calculated assuming a uniform spherical charge distribution whose radius was adjusted to fit electron scattering and muonic x-ray data. Energy-dependent 'outer' radiative corrections to order alpha, finite nuclear mass and screening effects associated with atomic electrons were also included in the δ_{WM} correction factor. The factor δ_R accounts for the outer radiative correction to orders $Z\alpha^2$ and $Z^2\alpha^3$ and is given by

$$\delta_R = 1 + 3.67\times10^{-4}|Z| + 3.60\times10^{-6}Z^2 \qquad (2.27)$$

where Z is the atomic number of the daughter nucleus. The final correction factor δ_D incorporates the effects of the diffuseness of the charge distribution

$$\delta_D = 1 + 1.8\times10^{-5}|Z|^{1.36} - 1.2\times10^{-6}|Z|W_0 \qquad (2.28)$$

The evaluation of the total phase space factor depends most critically on the beta Q value of the transition, an approximate E^5 dependence, which requires an accurate determination of coulomb energy differences between initial

and final states. These coulomb energies were assumed to follow

$$\Delta E_c(Z,A) = \xi_c(Z)\left[2(Z+1)/A\right]^{1/3} \qquad (2.29)$$

where the values of $\xi_c(Z)$ were obtained from empirical analog state binding energy differences and the neutron-proton mass difference. The values for $\xi_c(Z)$ are listed in table (2.2) and supply the last component necessary for determination of Gamow-Teller transions using the empirical shell-model approach. The following section utilizes this formalism to predict G-T decay modes and half-lives of neutron-rich nuclei.

2.3 Decay and Half-life Predictions

Beta decay features of neutron-rich nuclei have been calculated using the shell-model formalism discussed in the previous section. A variety of different model-space assumptions and effective interactions have been used (see figure 2-1) in order to ootain a comprehensive set of predictions for many light neutron-rich nuclei. The most complete set of beta decay predictions which include all $T_z \leq {}^5/_2$ nuclei falling within the sd shell were carried out using the USD interaction [Wi83]. The USD interaction was

TABLE 2.2

Z	$\xi_c(Z)$
8	3.509
9	3.999
10	4.300
11	4.787
12	5.020
13	5.495
14	5.695
15	6.086

Table 2-2. Coefficients used to determine coulomb energy differences between nuclei.

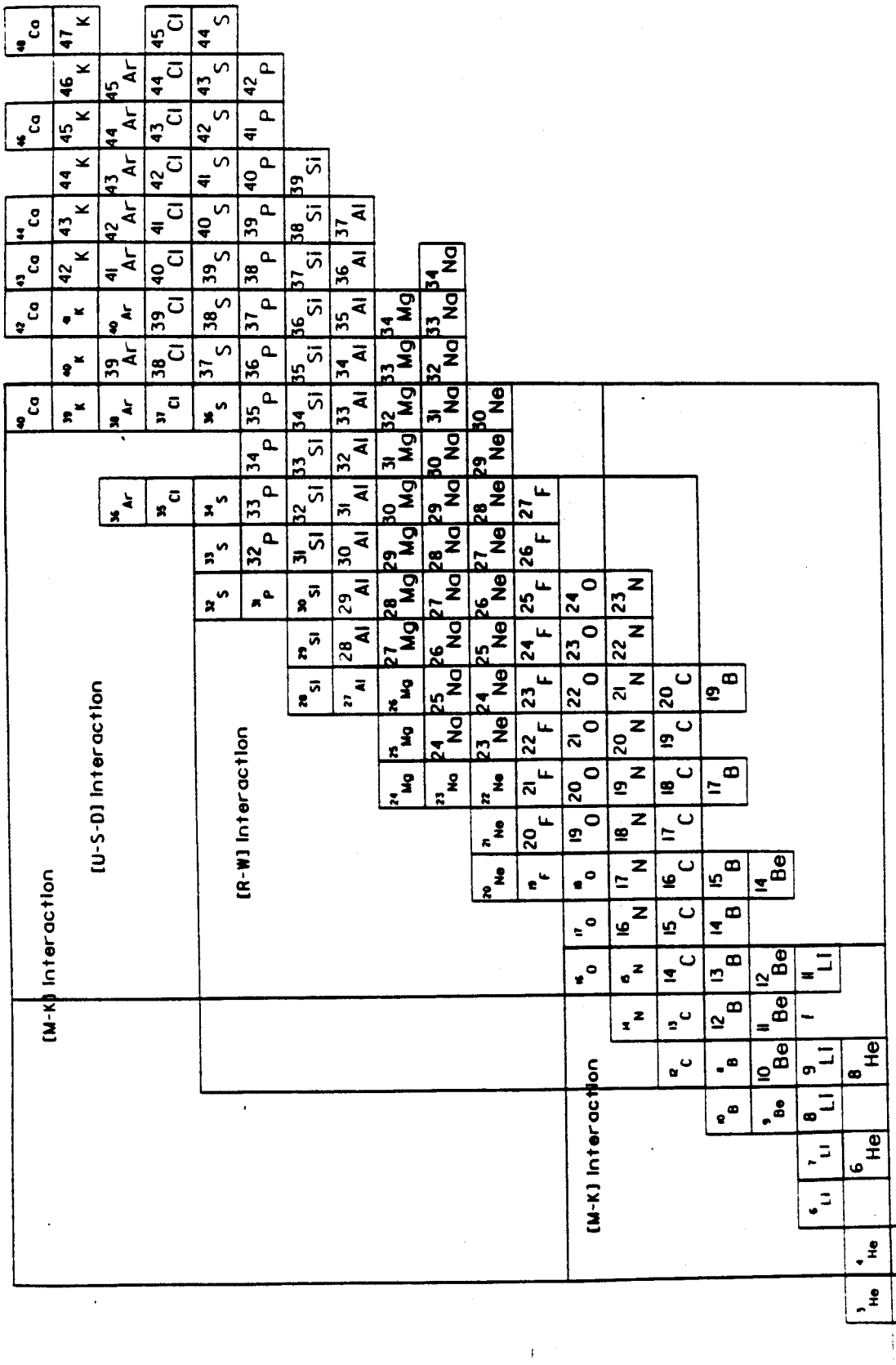

Figure 2-1. Chart of the Nuclides depicting the different effective interactions used for various mass regions.

constructed using the isospin formalism and limited to a fixed one-body spectrum and a set of two-body matrix elements which have been scaled by the A dependent factor $(18/A)^{0.3}$. Predicted half-lives have been scaled by 1.69 to account for the observed $\sigma\tau$ quenching within the sd-shell [Br83]. The calculated half-lives are compared to existing experimentally determined half-lives in figure 2-2. Due to the strong influence of beta Q values on the half-lives of neutron-rich nuclei, a comparison between measured and calculated Q values is presented in figure 2-3 which provides insight into discrepancies originating from the energy dependent contributions.

Beta decay predictions were extended down into the p-shell orbits to include light neutron-rich nuclei that had low-lying negative parity states. Level structures for $j \leq 5/2$ and decay modes were calculated for ^{17}C, ^{17}N, ^{19}O, and ^{19}N using the Reehal-Wildenthal Hamiltonian [Re73] which spans the space $(0p_{1/2}, 0d_{5/2}, 1s_{1/2})$ [Cu81,Cu82]. The ground state of ^{19}N was calculated to be $1/2^-$, well separated from its first excited state. However, in ^{17}C the three lowest lying states ($5/2^+$, $3/2^+$, $1/2^+$) were predicted within 570 KeV of each other making the ground-state J^π assig ment difficult. Coupling this with the observed ground-state inversion ($1/2^+$) of ^{15}C forced us to consider all three J^π

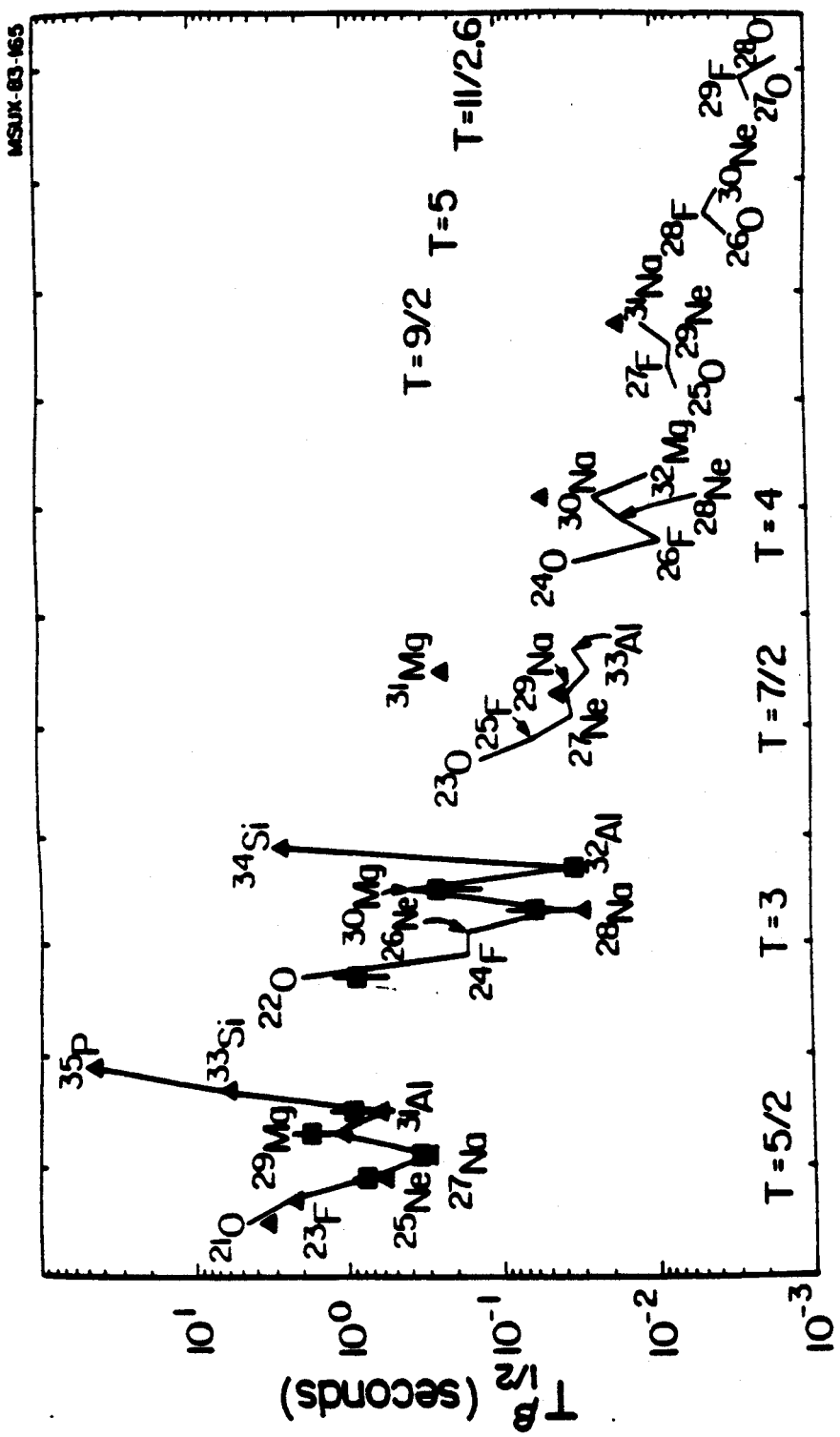

Figure 2-2. Comparison of half-lives calculated for the Gamow-Teller beta decay of the sd-shell nuclei with five or more excess neutrons with experimental measurements. The solid line represents the shell model predictions using the USD interaction of Wildenthal. Experimental values are taken from [Mu84] and references sited within.

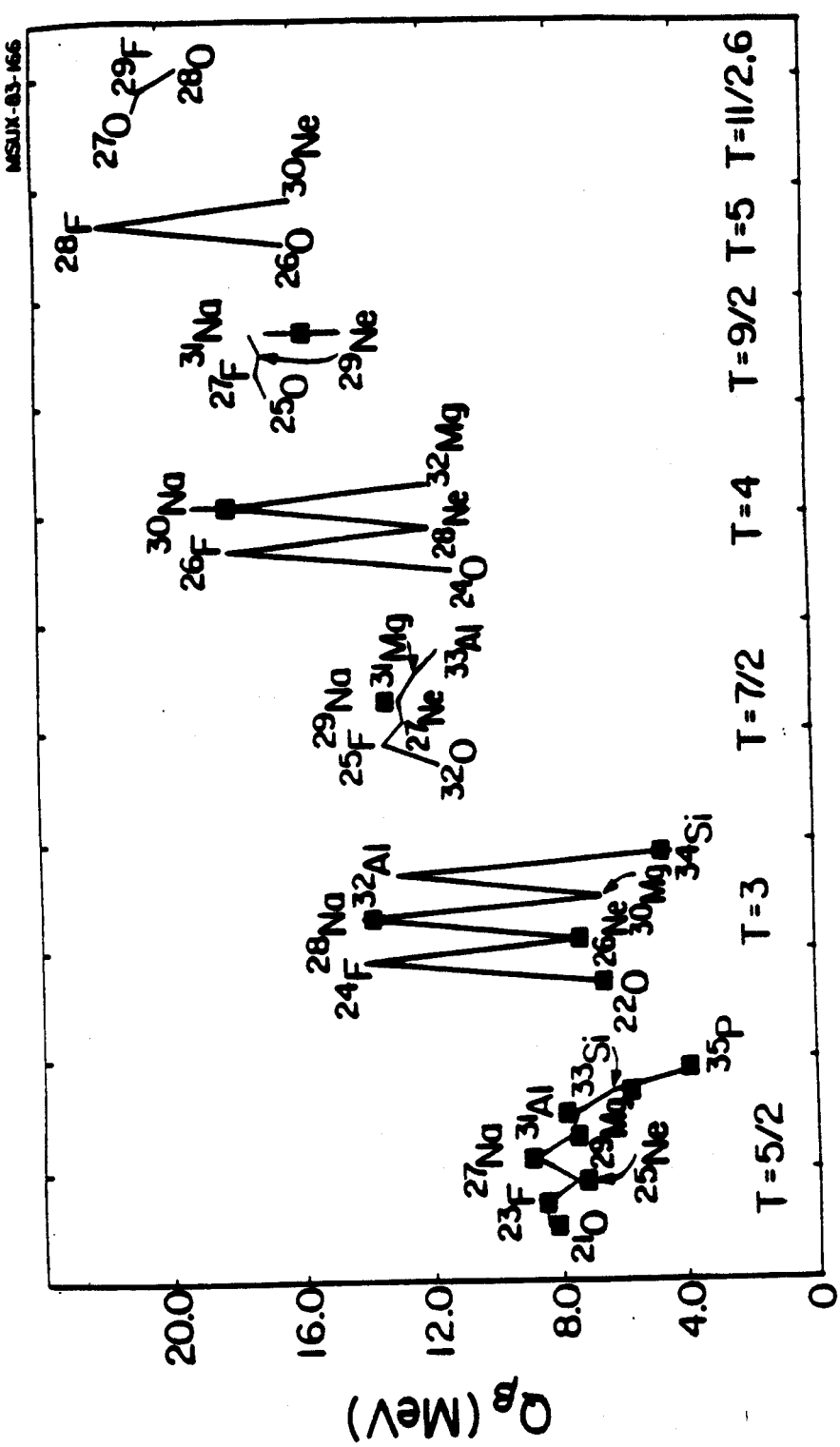

Figure 2-3. Comparison of beta Q values calculated for the decays of the sd-shell nuclei with five or more excess neutrons with experimental values. The solid line represents the predicted beta Q values using the USD interaction of Wildenthal. Experimental values are taken from [Wi83] and references sited within.

values as reasonable candidates for the ground-state of ^{17}C. Decay modes and half-lives for ^{17}C and ^{19}N are shown in figures (2-4,2-5,2-6) where the half-lives have included the 0.6 quenching factor discussed earlier. It is observed that exclusion of spin-orbit partners, such as $0d_{3/2}$ in this calculation, results in a shorter predicted half-life than observed experimentally [Mc70]. This can be attributed to the mixing of differing phases associated with spin-orbit partners as seen in equation (2.22). In order to eliminate this effect, additional calculations were done using the Millener-Kurath interaction [Mi75] which represents a full $2\hbar\omega$ calculation. Of particular interest are the predicted decay modes of ^{17}C, ^{15}B, ^{11}Li, and ^{14}Be which are shown in figures (2-7,2-8,2-9). These predictions prove interesting since it is possible to extract spectroscopic information about the parent and daughter nuclei through a half-life measurement as will be discussed in section 3.4 of this thesis.

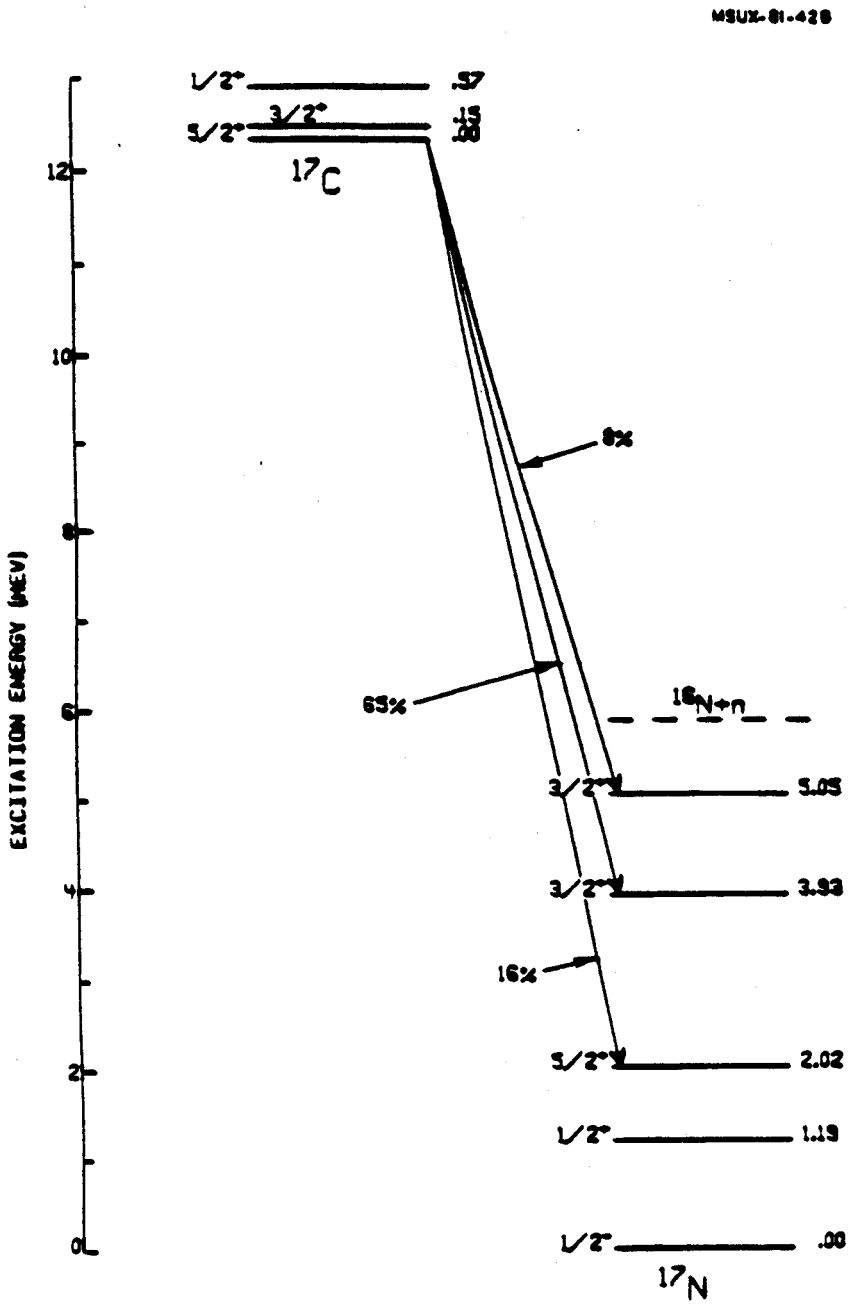

Figure 2-4. Gamow-Teller beta decay branching ratios predicted for the decay of ^{17}C using the Reehal-Wildenthal interaction. The predicted half-life is ≈100 ms when a $^{5}/_{2}^{+}$ ground state J^{π} is assumed (quenching has been included).

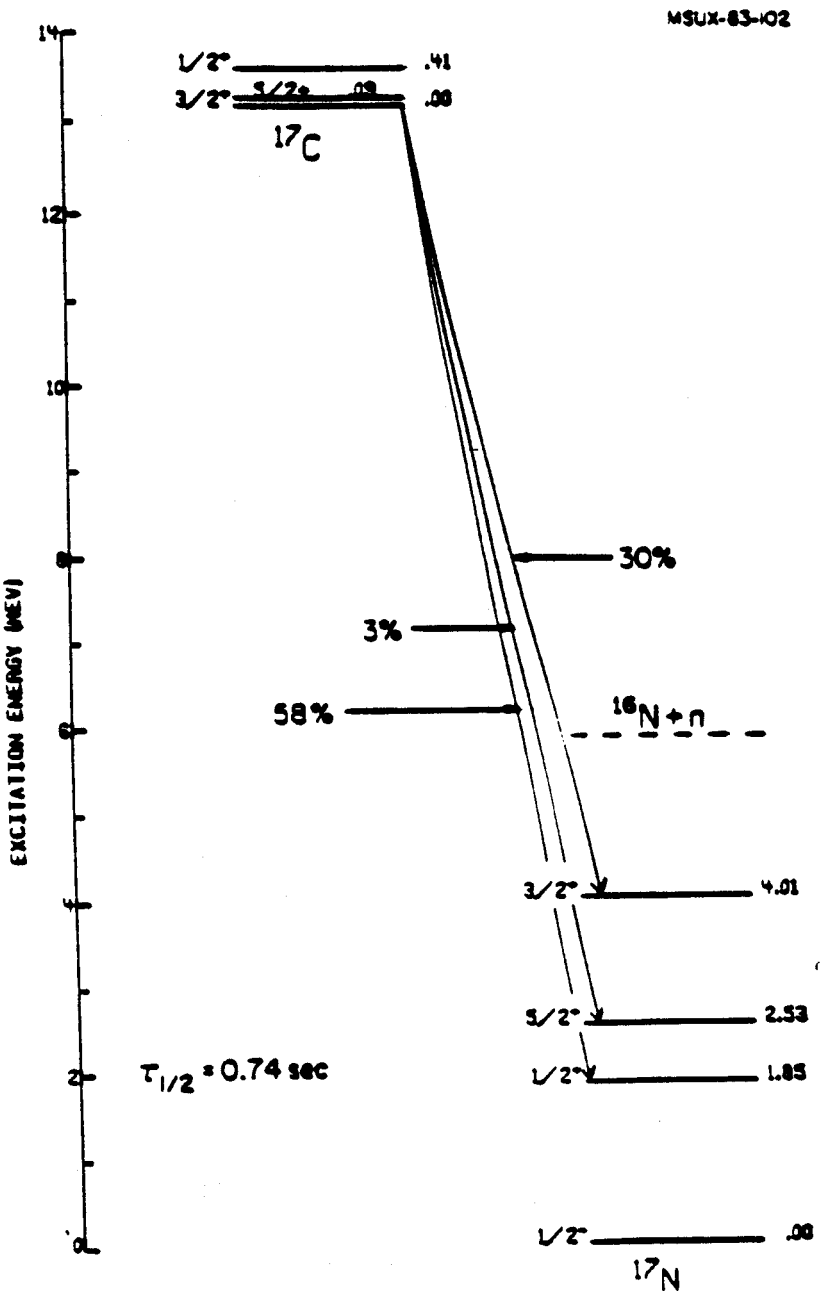

Figure 2-5. Gamow-Teller beta decay branching ratios predicted for the decay of ^{17}C using the Millener-Kurath interaction. This full $2\hbar\omega$ calculation predicts an inversion of the $^3/_2^+$ and $^5/_2^+$ states in ^{17}C in addition to predicting a much longer half-life (quenching has been included).

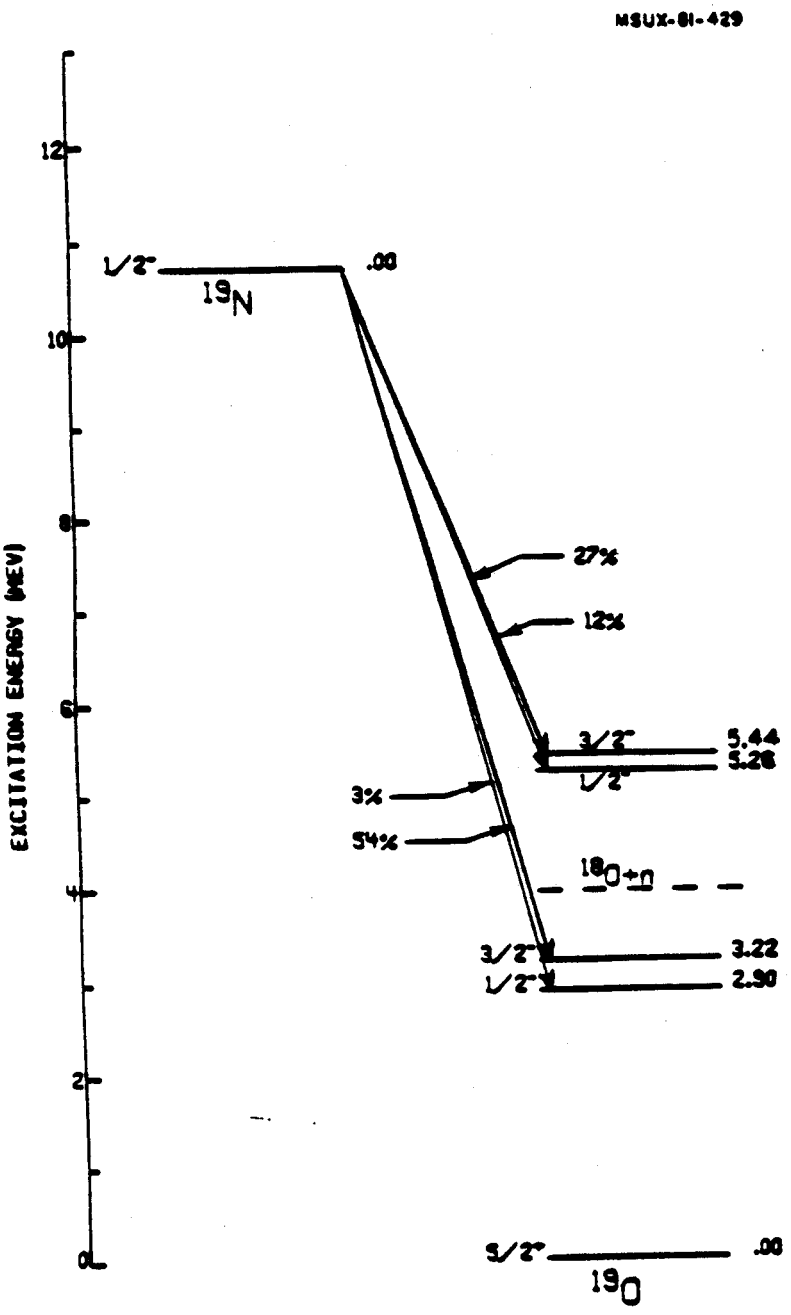

Figure 2-6. Gamow-Teller beta decay branching ratios calculated using the Reehal-Wildenthal interaction. The ground state of ^{19}N was predicted to be $^1/_2^-$ with 43% of the branching strength popoulating neutron unbound states in ^{19}O.

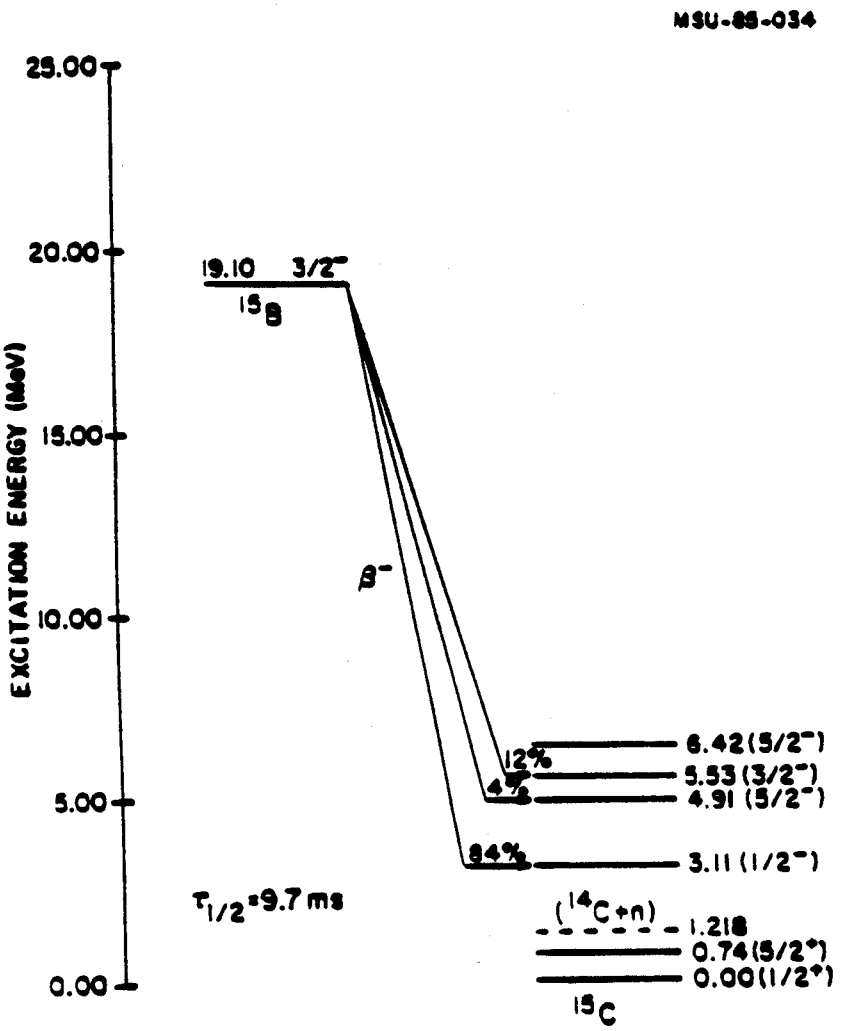

Figure 2-7. Gamow-Teller branching ratios predicted for the decay of ^{19}B using the Millener-Kurath [MK] interaction. The calculation predicts a 9.7 ms half-life with all decays populating neutron unbound states in ^{15}C.

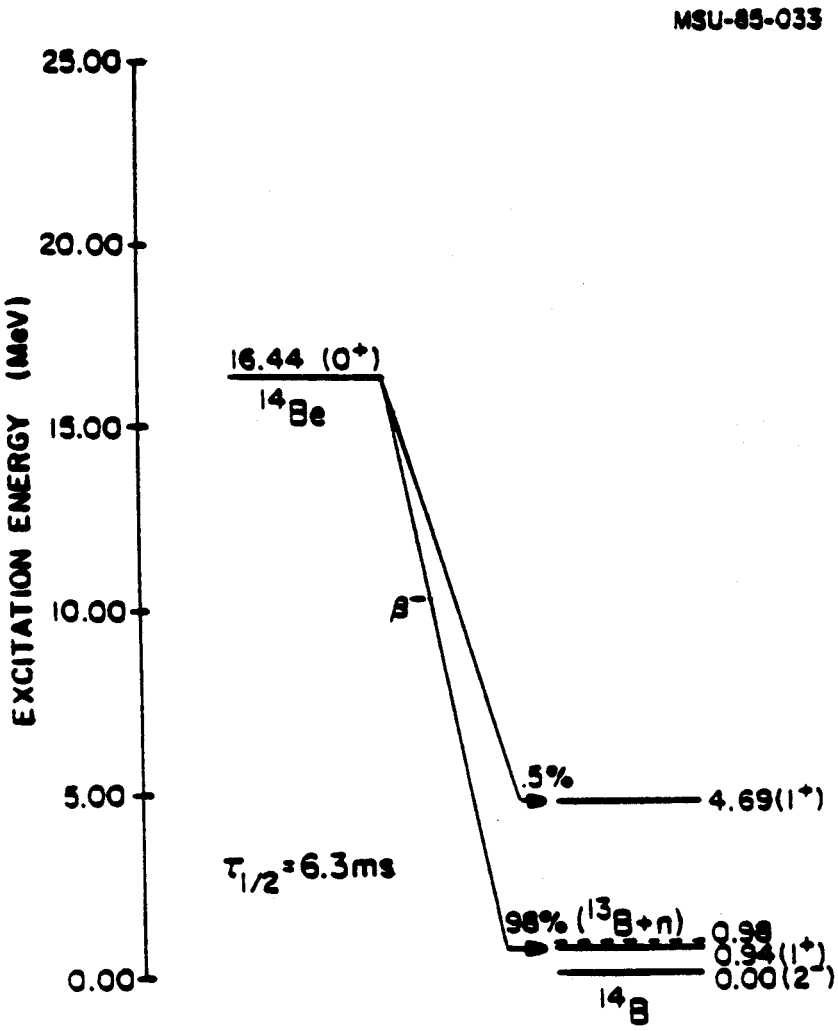

Figure 2-9. Gamow-Teller branching ratios predicted for the decay of ^{14}Be using the [MK] interaction. The calculation predicts a strong (98%) branch to a 1^+ state in ^{14}B.

Chapter 3 - Half-life Measurements of Neutron-rich Nuclei

3.1 Introduction

The primary objective of this experiment was to utilize the high-intensity heavy-ion beams provided by the K500 cyclotron for the production of neutron-rich light nuclei and to measure their corresponding half-lives. In addition, this experiment would serve as the first significant test of the mass separating capabilities of the Reaction Product Mass Separator (RPMS). The performance of the RPMS is discussed in appendix A, as are its design and construction aspects. This experiment utilized an isotopically enriched ^{18}O beam on targets of ^{9}Be and ^{181}Ta for the production of light neutron-rich nuclei. The target thickness was chosen to stop the primary beam so that projectile fragments could be observed at a 0° scattering angle. A schematic diagram which depicts a 35 MeV/A ^{22}Ne beam stopping in a 1.4 mm^2 carbon foil is shown in figure 3-1, illustrating what is believed to occur within the target. At any location within the target, an incident projectile may undergo a nuclear fragmentation producing reaction products that must then traverse through the remaining target material. The reaction products have lower Z values than the beam and, therefore, more range allowing them to escape from the target. The code DONNA has been used to calculate the energy loss of both the

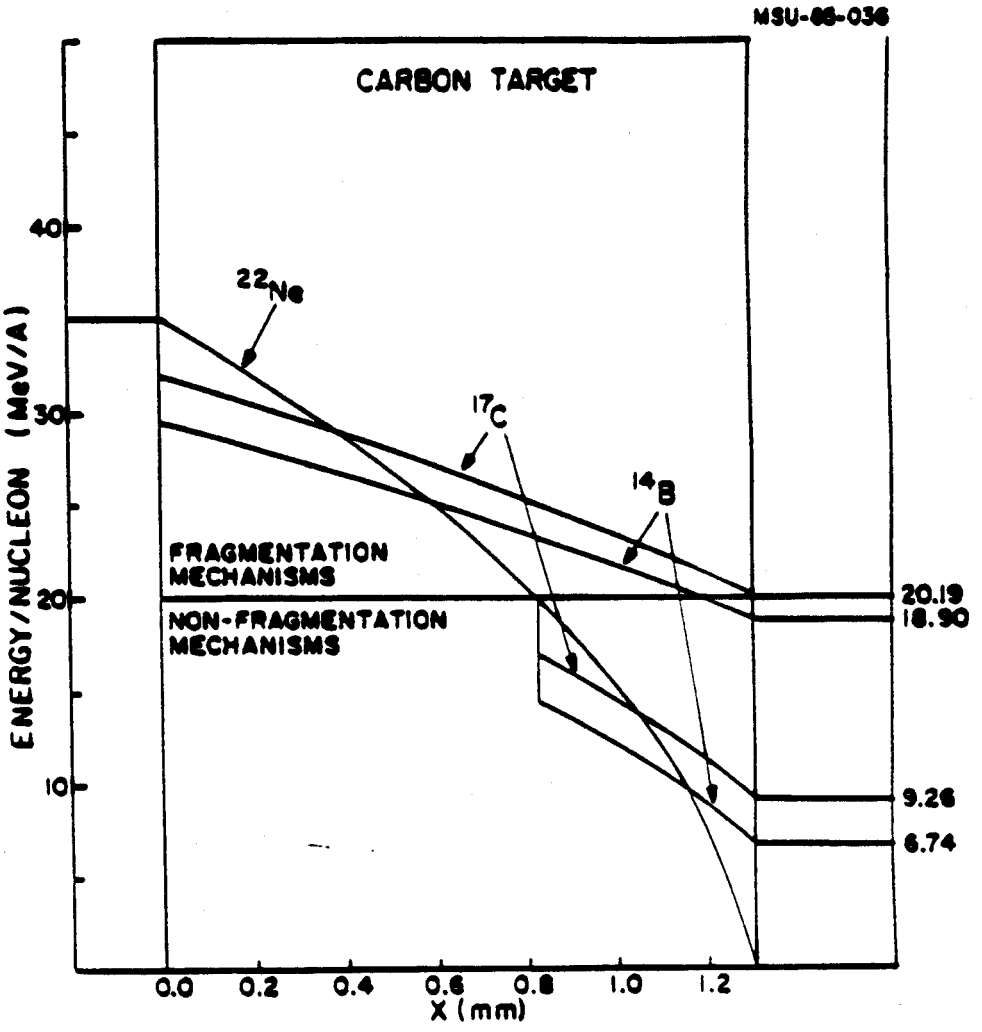

Figure 3-1. Schematic illustration of a 35 MeV/A ^{22}Ne beam traversing a thick carbon foil. The energy loss calculations were performed using the code DONNA.

beam and fragments as they pass through the target. The reaction products emerge with a broad range of velocities due to the distributed source within the target. The sudden reduction in velocity associated with the nuclear collision was calculated using

$$\Delta\left(\frac{E}{A}\right) = \frac{n\,\chi}{A_{ps}} \qquad (3\text{-}1)$$

where

$\Delta(E/A)$ = reduction of the projectile fragment's energy per nucleon

A_{ps} = number of nucleons in the projectile-spectator

n = number of nucleons removed from the incident projectile (3-2)

χ = binding energy per nucleon of the incident projectile

The large overlap of velocities between differing isotopic species suggested by the calculation, indicates that for thick targets the velocity slits at the end of the Wien

filter may have limited value. During the actual experiment the target thickness was reduced (via a target rotation) until the first indications of increasing background in the focal plane detector system were observed. This technique allowed isotopes with Z closer to that of the beam to be observed and studied. The experiment also produced valuable information concerning the isotopic yield dependence on target material. For instance, using the ^{181}Ta target resulted in a moderate rate of ^{14}Be whereas the ^{9}Be target did not produce any significant ^{14}Be rate, this target material dependence was even more dramatic when ^{17}C rates were compared. This same target dependence was also see in the Ganil work which provided the primary motivation for using the heavier targets [Gu83].

3.2 Experimental Setup and Procedure

The experiment consisted of bombarding targets of ^{9}Be and ^{181}Ta with a 30 MeV/A $^{18}O^{5+}$ beam extracted from the K500 cyclotron at the National Superconducting Cyclotron Laboratory (NSCL). The experiment involved repeated measurements of the time interval between the detection of a heavy-ion reaction product and its associated beta, a technique similiar to that employed by the Lawrence Berkeley collaboration [Mu82]. The electronics setup used during the

experiment is shown in figure 3-2. During the actual experiment the electronics could be run in one of two possible modes corresponding to continuous-beam mode or gated-beam mode. With continuous beam it was possible to accumulate (within a reasonable time) enough statistics on heavy-ion reaction products to optimize the isotope of interest on the focal plane detector system. The gated-beam mode was used when actual half-life measurements were underway. Central to the electronics setup is the BEAM-OFF gate generator (located near the center of figure 3-2) which was used to eliminate the beam for a designated time period. Elimination of the beam was iniciated with a TTL signal from the BEAM-OFF gate generator and accomplished by shifting the phase of the cyclotron RF (observed to eliminate the beam within 40 μsec). A quartz oscillator pulser feeding a scaler provided the time information necessary to determine half-lives (i.e. a clock) and was monitored frequently throughout the run to insure stability. The focal plane detector system consisted of a 2-dimensional position-sensitive proportional counter [Or81] followed by a solid-state detector telescope made up of a 300 mm^2 × 100 μm (Si) ΔE detector backed by a 500 mm^2 × 5 mm (SiLi) E detector, as shown in figure 3-3. The detector system was only 1.0 m down line from the last quadrupole doublet, just outside a 10 mil stainless steel vacuum window. A pair of horizontal and vertical defining slits were positioned directly in front of the 2-dimensional

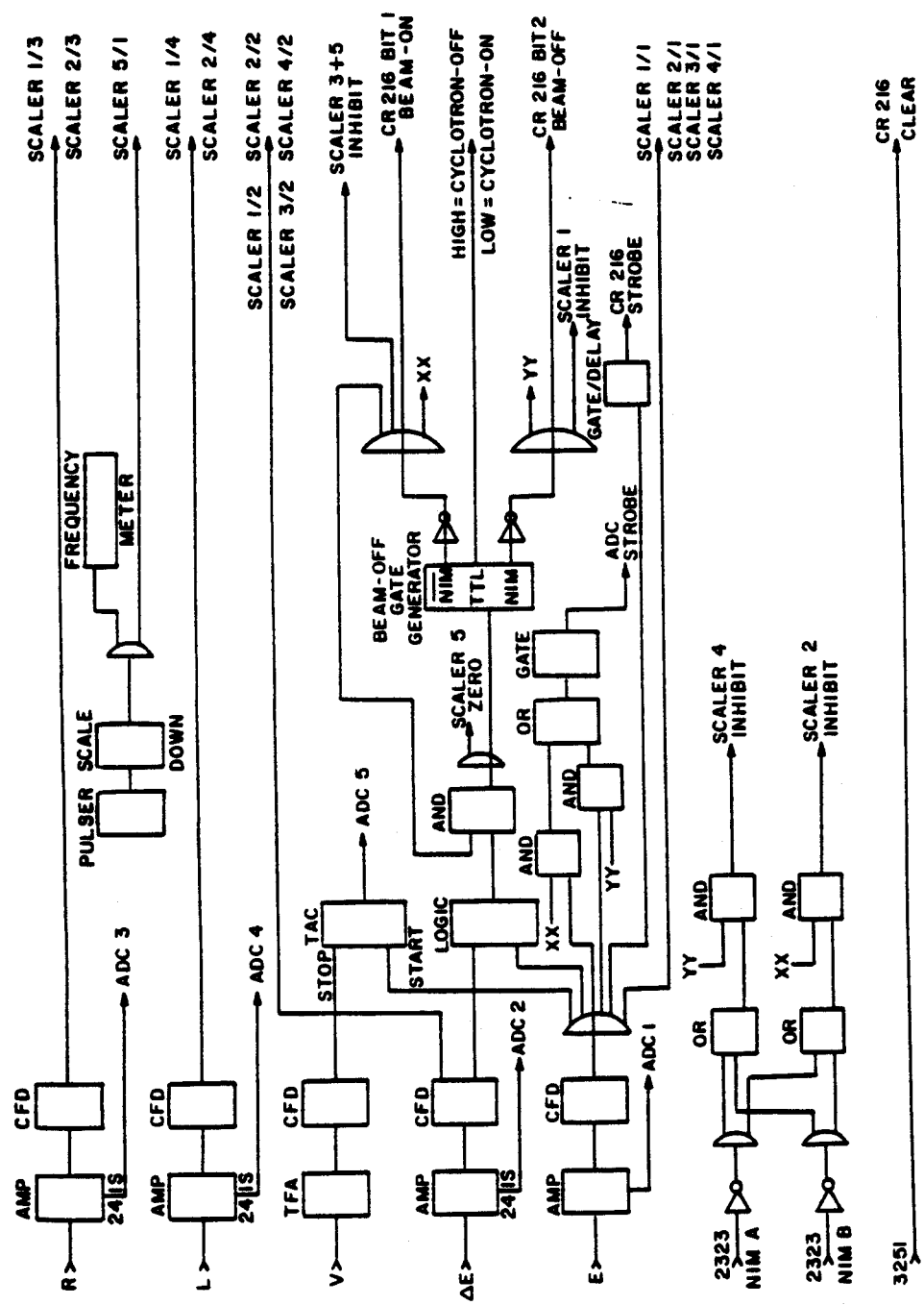

Figure 3-2. Schematic diagram illustrating the electronics used for half-life experiment on the RPMS.

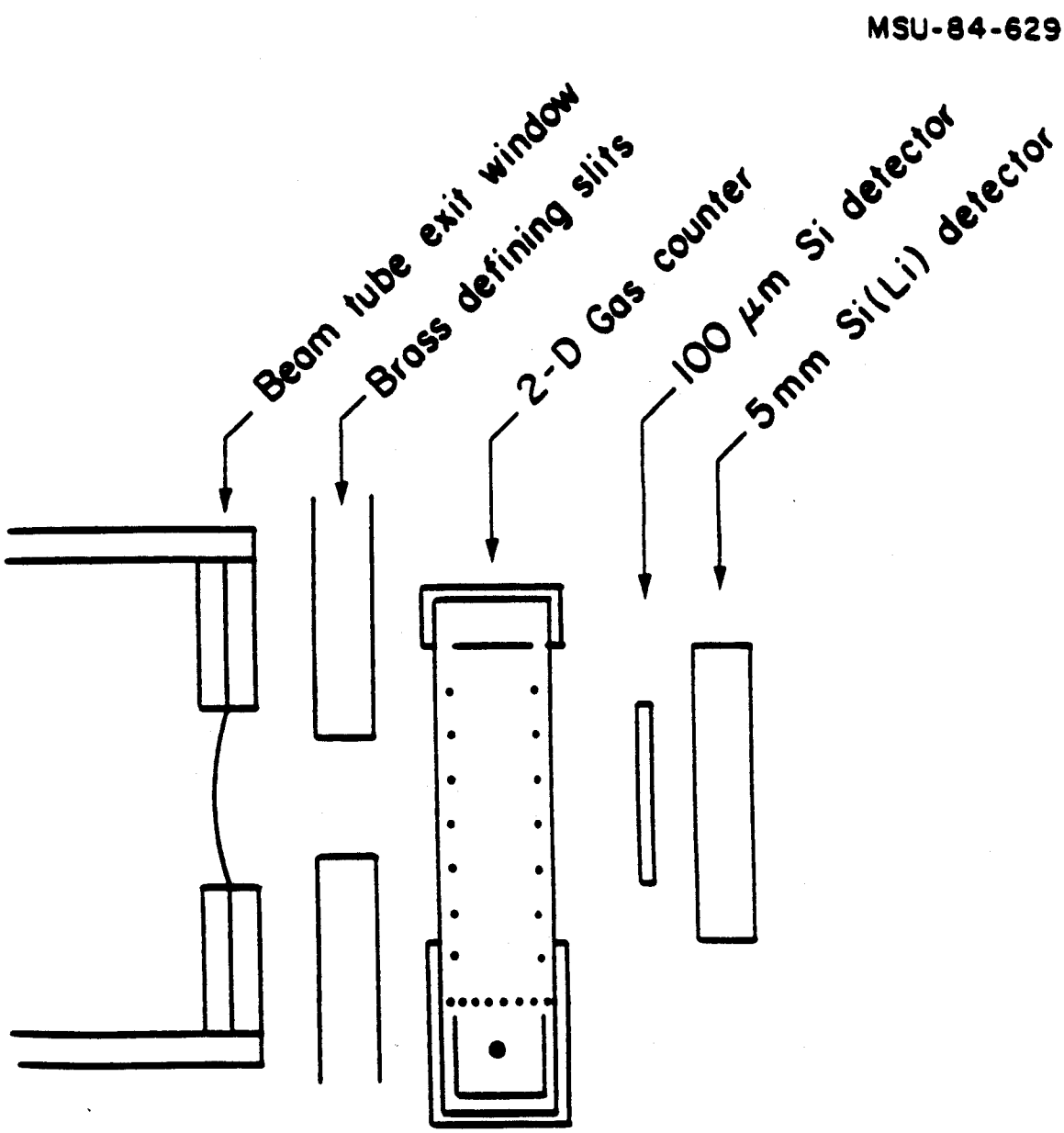

Figure 3-3. Schematic drawing of the focal plane detector arrangement used in the half-life measurements on the RPMS.

proportional counter allowing the removal of interfering M/Q species. Beta decay half-life measurements were carried out one ion at a time since many different isotopic species had similiar or identical M/Q values. This technique proved useful since it would allow simultaneous measurements of all isotopic species hitting the detector system. The beam off time interval was adjusted to the longest lived species so that ions stopping in the E detector had a good chance of decaying before the arrival of the next ion. In addition to on-line analysis all data were written to tape for more complete analysis at a later date.

3.3 Data Analysis

Data analysis was carried out in a tape-playback mode using the histogramming program SARA [Sh85] on a VAX 750. Data written to tape during the experiment consisted of two differing types corresponding to beam-on and beam-off events. Beam-on information consisted of five signals providing particle identification along with horizontal and vertical position information. Beam-off information consisted of energy signals from the solid-state telescope and time information from a pulser feeding a scaler. Heavy-ion reaction products were identified using a particle identification function (P.I.D.) coupled with vertical position information related to the M/Q of the isotopic species. The P.I.D. function was constructed using the ΔE

and E signals from the solid-state telescope according to the following relation [Mu82]

$$(E + \Delta E)^{1.78} - E^{1.78} = A^{0.78} Z^{2} \qquad (3.3)$$

It should be mentioned that the expression stated above is less valid when the ion loses a small amount of energy in the second detector. Deviations from the functional form given in (3.3) were seen for a small percentage of events in this experiment as shown in figure 3-4, however the overall quality of this functional form was very good as seen in figure 3-5. Plotting vertical position vs. the particle I.D. function results in islands corresponding to differring isotopic species as illustrated in figure 3-6. Placing 2-dimensional contours around various isotopic groups allows their beta decay spectra to be accumulated. Beta decay for nuclei contained within this study either represent mother-daughter decays or simple decays where the daughter nucleus is stable or long-lived. The histogramming code was written to allow up to a maximum of six half-life curves to be generated simultaneously during a single run if simple beta decay is appropriate. However, if a mother-daughter decay is appropriate then only the mother and corresponding daughter decay curves can be accumulated during a single run. Histogramming the time interval distribution between a specific beam-on event and all subsequent beam-off events

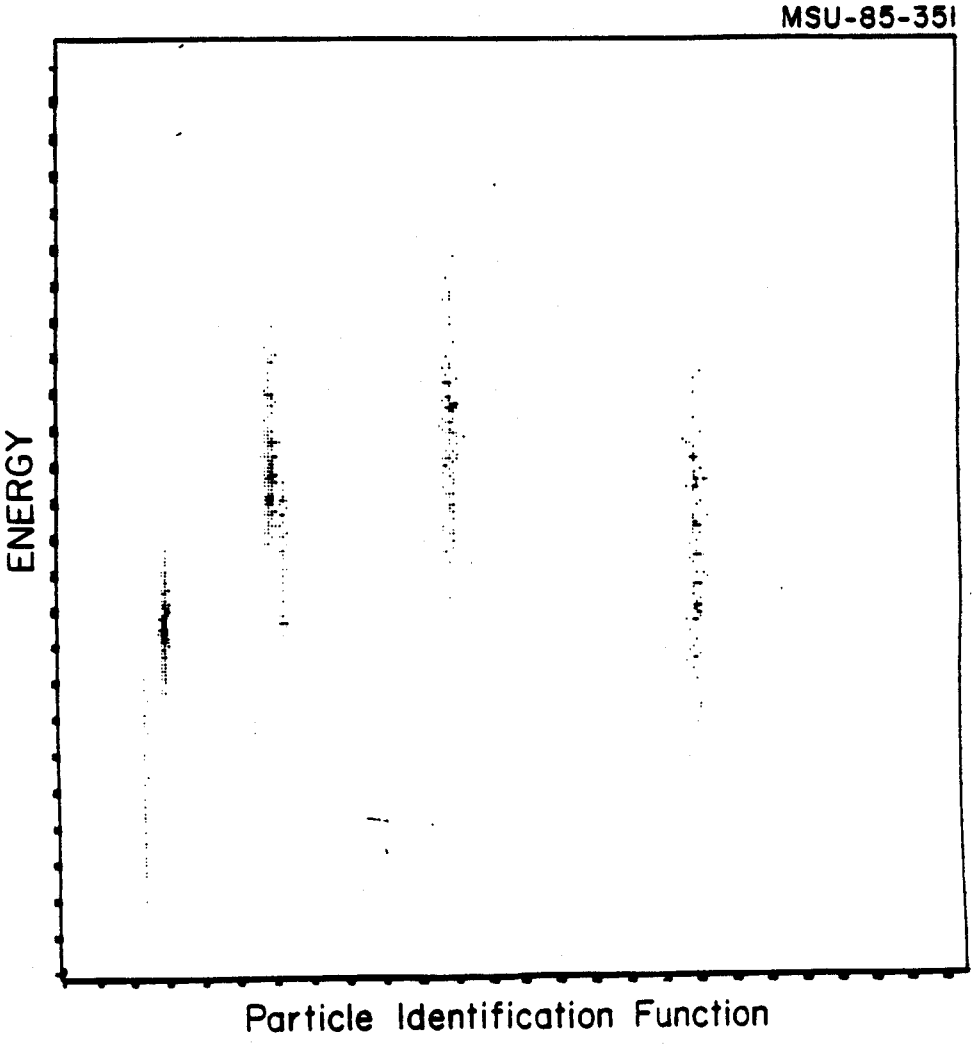

Figure 3-4. Spectrum of the E detector signal vs. the particle identification function illustrating the energy characteristics of the reaction products hitting the focal plane detector system.

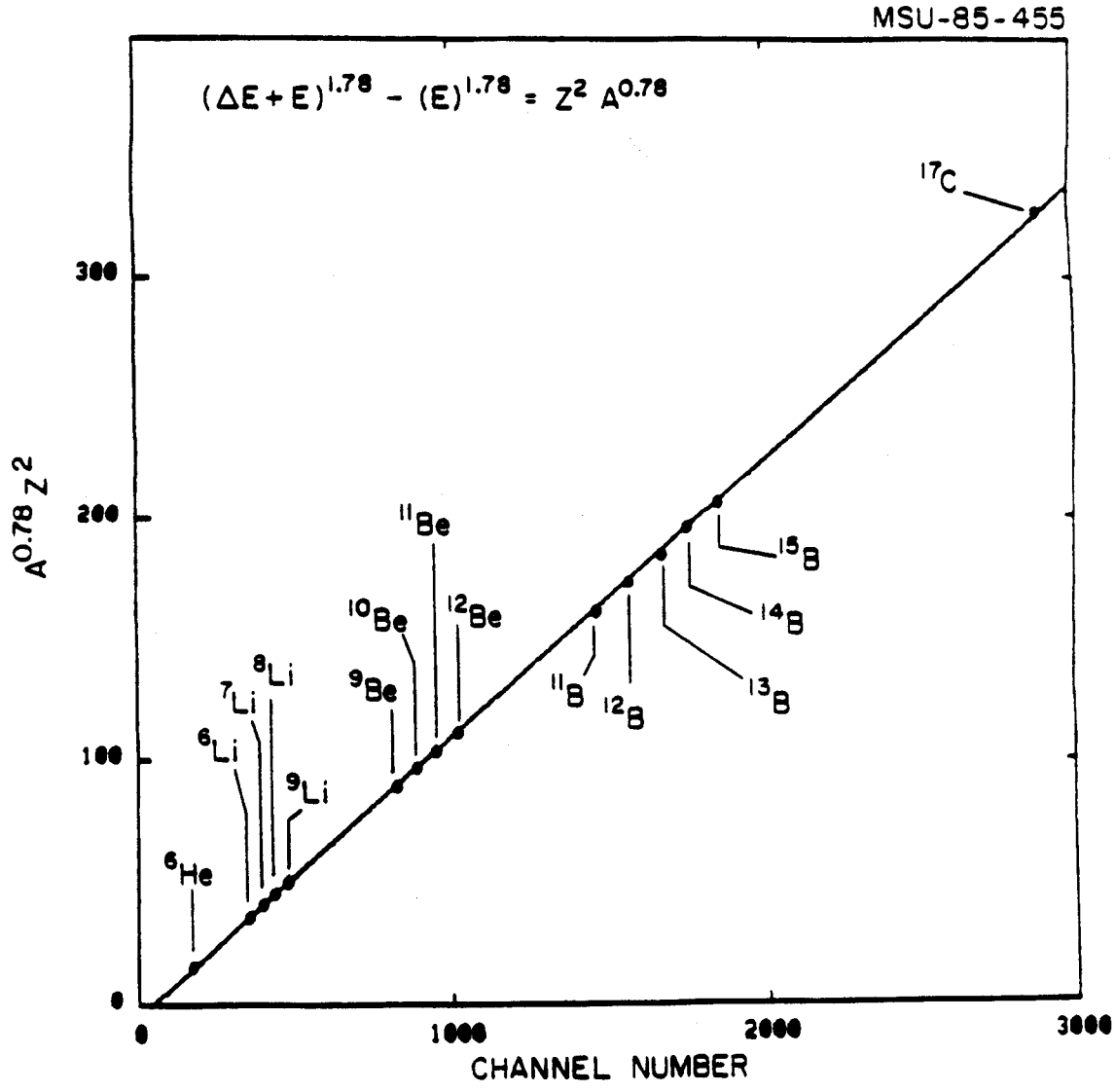

Figure 3-5. Linear fit to mass centroids demonstrating the quality of the particle identification function.

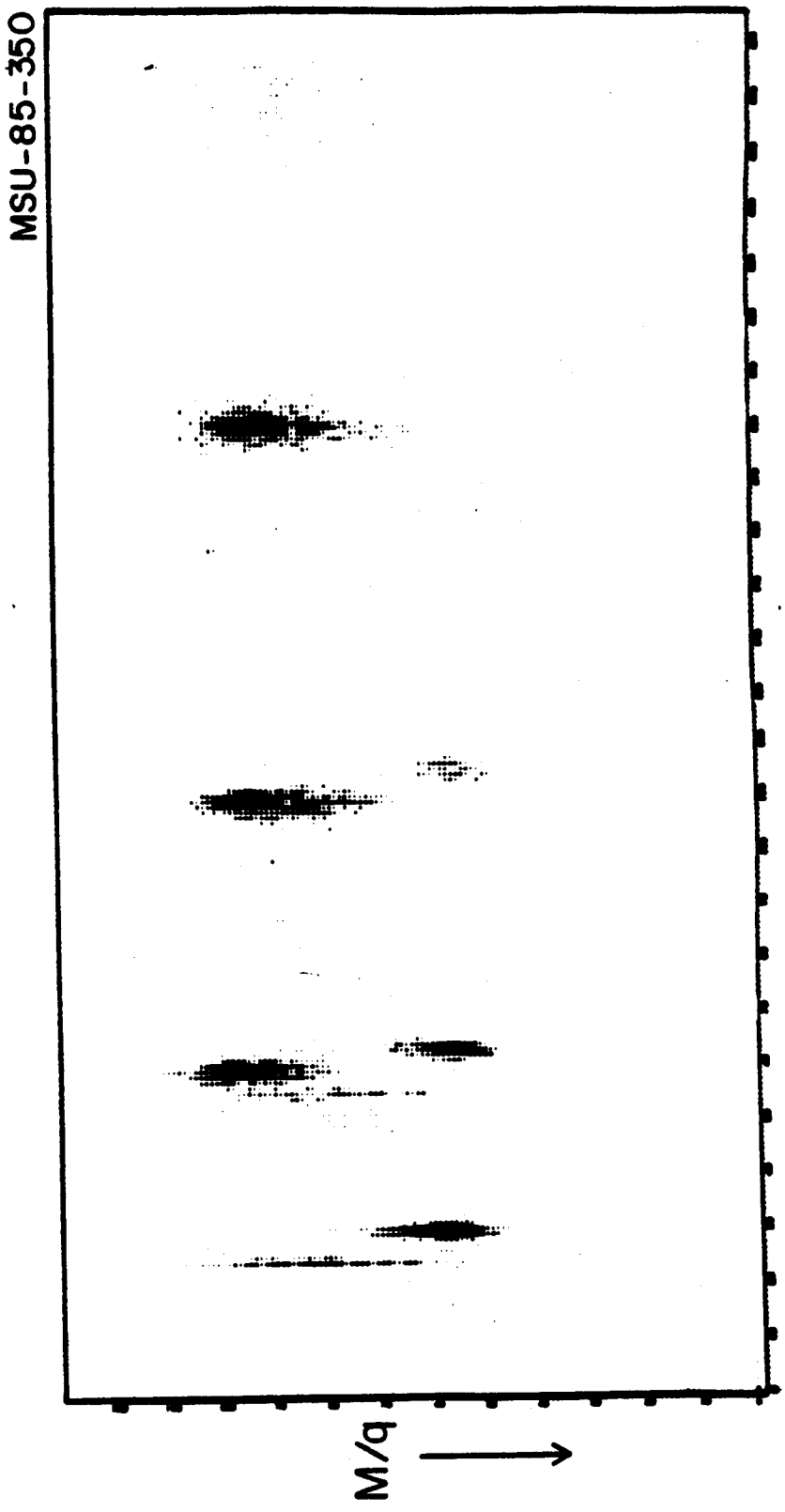

Figure 3-6. Illustration of the mass islands corresponding to different isotopic species.

occurring within the beam-off time interval results in a beta decay curve corresponding to that particular isotope. The channel to time conversion factor was obtained using the pulser frequency recorded during the run (for many of the runs this calibration was 0.6104 ms/channel). A lower level energy gate of 2-3 MeV was placed on the electron energies to insure that the ^{6}He decays did not enter into the decay curves for runs taken at M/Q=3. The efficiency for observing a beta following a heavy-ion event should be approximately 50% due to the detector geometry and agrees well with the efficiencies observed. To check the beta efficiencies, the number of betas observed within each beam-off time interval were monitored and the results will be presented in section 4 of this chapter. Once the decay curves were generated a least squares fit assuming a simple exponential plus constant background was performed with the program LEASTSQUARES to determine the half-life.

For the more complicated mother-daughter decays the method used required a second beta to follow the first beta within a fixed time period [T ms]. Setting this time value equal to approximately 2 half-lives of the daughter significantly cleaned up the mothers decay curve without severely reducing the total number of events. It is expected that this condition would result in approximately a factor of 2 reduction in the total number of events in the parent decay curve. The daughter's decay half-life could also be

extracted by taking the time difference between the first and second betas and histogramming the resulting time distribution. This method of dealing with mother-daughter decays proved very effective and even allowed some spectroscopic information to be extracted from the resulting half-lives. For a number of runs a fast component was observed in the beta decay spectra which is believed to come from thermal neutrons generated during the beam-on time. Thermal neutrons within the room having a characteristic energy of 1/40 eV (corresponding to velocities around 2 m/msec) will eventually come in contact with the room walls (or whatever) and undergo a (n,γ) capture. The resulting γ can then be picked up in the solid-state E detector and produce a "decay time" characteristic of the room. In order to estimate the effect of this fast component on the resulting half-lives a contour was placed around a long-lived isotopic species such as ^{11}Be and its decay curve was accumulated (see figure 3-7). By scaling the number of events contained within the fast background component with the number of heavy-ion events contained within the contour results in a comparatively weak contribution to the "true" beta decay half-life. Scaling with respect to the number of heavy-ion events is justified since the number of neutrons generated during the beam-on time interval is proportional to the beam intensity. Details associated with how these effects were taken into account

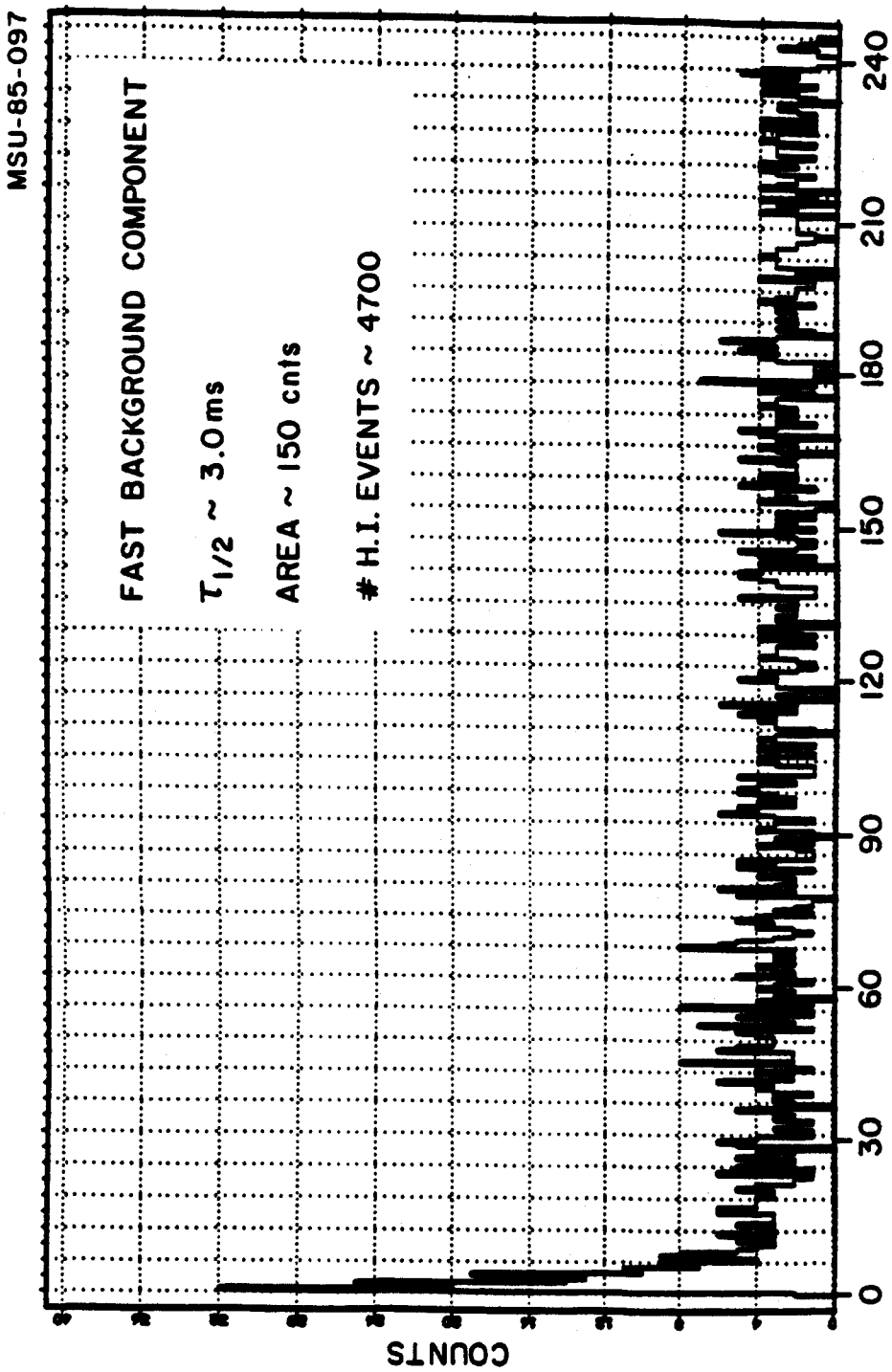

Figure 3-7. Spectrum of the fast component believed to originate from thermal neutrons. The heavy-ion gate was placed around the long-lived lithium isotopes.

will be discussed in the next section along with the resulting half-lives of the 8 neutron-rich nuclei observed in this experiment.

3.4 Results

Half-life determinations for 8 neutron-rich light nuclei are carried out assuming either a simple decay mode or a mother-daughter decay mode. The experiment resulted in basically three different runs which are labeled as A, B and C. The parameters that are controlled in the analysis are the following

i) Heavy-ion contour
ii) electron energy contour
iii) binning size
iv) [T] in mother-daughter decays

A discussion of how each of these parameters can affect the extracted half-life will be given in section 4.1 along with a summary of the "best" choices for each. Run A was taken using a beam-off time interval of 0.7 sec. and a clock frequency of 26.2142 kHz. The RPMS was set to allow M/Q species between 3.00 and 2.75 to reach the focal plane detector system (see figure A-12 (b)). The isotopes observed in sufficient quantity to allow half-life determinations

were ^{11}Be, ^{14}B, ^{17}C, ^{9}Li, ^{12}Be, ^{15}B and the daughter decay of ^{12}Be (i.e. ^{12}B). Half-life determinations for ^{9}Li and ^{17}C were hampered due to the short value of the beam-off time interval as compared to their extracted half-lives. Previous half-life determinations for ^{9}Li gave 175±1.0 ms which allows approximately 4 half-lifes to be observed. Using a least squares fitting routine and assuming the curve to be comprised of an exponential plus constant backgound resulted in a half-life of approximately 150±28 ms. However, the constant background value was poorly determined and the fast component associated with thermal neutrons was not taken into account. The situation for ^{17}C was similiar to that for ^{9}Li indicating that another run should be undertaken with a longer beam-off time interval (run C). The half-lives of ^{14}B and ^{15}B were determined using the simple beta decay assumption. The resultant half-life of ^{15}B is given in table 3-1 and represents our only measurement of this isotope. The half-life of ^{14}B was averaged with the half-life determination from run C and that result is given in table 3-1 as well. The half-life of ^{11}Be (≈13.8 sec.) could not be determined yet it provided a method for obtaining the decay time associated with the fast background component. To determine the half-life of ^{12}Be and its daughter ^{12}B a

mother-daughter decay was assumed and resulted in the half-lives given in table 3-1. Run B was characterized by a beam-off time interval of 0.52 sec. and the same clock frequency as previously used. The RPMS was set for M/Q=3.5 with ^{11}Li also coming in with sufficient intensity to allow a half-life determination. Since the daughter of ^{11}Li is long-lived a simple beta decay was used for its half-life determination whereas for ^{14}Be a mother-daughter decay was used. The statistics for ^{14}Be were fairly low yet a good half-life measurement resulted which was also the case for ^{11}Li (both results are given in table 3-1). The half-life associated with the daughter decay of ^{14}Be was 10-11 ms indicating that the lowest lying 1^+ state in ^{14}B is below the neutron threshold as shown in figure 2-9. The final run (run C) contained essentially the same M/Q values that were seen in run A, except the the M/Q dispersion was increased and the defining slits were narrowed eliminating many of the M/Q=3.0 nuclei. Sufficient yields of ^{14}B, ^{9}Li and ^{17}C allowed half-life measurements of these nuclei. The beam-off time interval was set at 2.04 sec allowing an accurate background to be fit for the Li and C isotopes. The resultant half-life determinations are given in table 3-1. The resulting decay curves for runs A, B and C with their corresponding best fits are shown in figure 3-8. Each curve has been truncated in time for display in this figure. In each case the curves

Table 3-1

Isotope	This Measurement	Previous Measurement	Prediction[f]
^{9}Li	173±14 ms	175±1 ms[a]	127 ms
^{11}Li	7.7±0.6 ms	8.5±0.2 ms[a]	3.5 ms
^{12}Be	21.3±2.2 ms	24.4±3.0 ms[b]	14.7 ms
^{14}Be	4.2±0.7 ms	---	4.7 ms
^{12}B	20.0±1.5 ms	20.41±.06 ms[c]	22.7 ms
^{14}B	12.8±0.8 ms	16.1±1.2 ms[d]	18.6 ms
^{15}B	8.8±0.6 ms	11.0±1.0 ms[e]	10.3 ms
^{17}C	202±17 ms	---	(689,487,396) ms

a) Reference [Ro74]
b) Reference [Al78]
c) Reference [Aj75]
d) Reference [Aj76]
e) Reference [Du84]
f) Reference [Br85]

Table 3-1. Comparison between half-lives from the present investigation, previous studies and shell model predictions

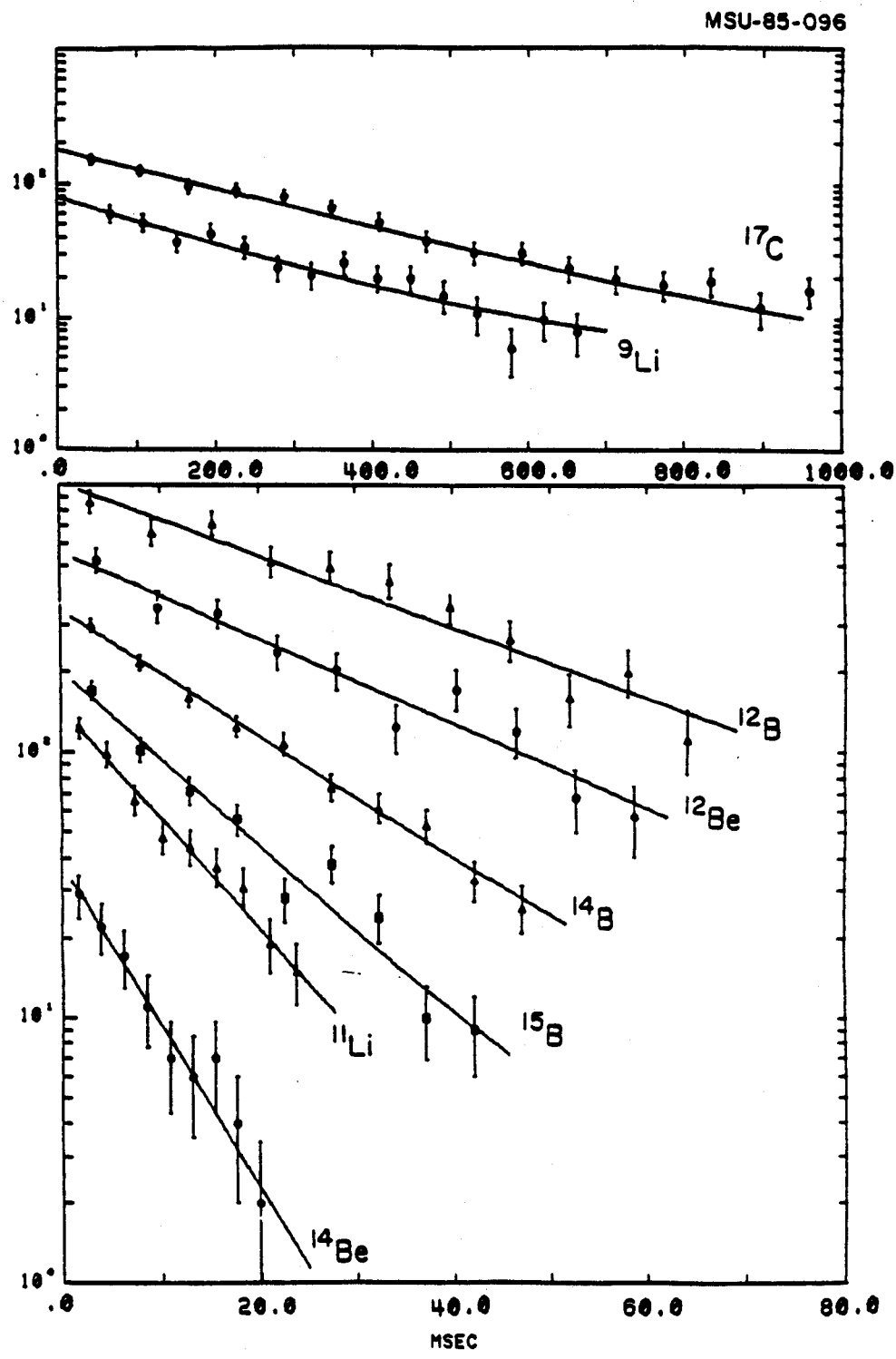

Figure 3-8. Decay curves with their corresponding best fits for the 8 neutron-rich isotopes measured in this experiment.

were extended in the analysis to obtain a good determination of the background.

Chapter 4 - Summary and Recommendations for Future Study

4.1 Summary and Conclusion

The results presented in table 3-1 represent the "best" half-lives as determined using a method of analysis employing different combinations of the parameters listed in section 3.4. The heavy-ion particle identification was made using a combination of M/Q information (vertical position) and particle I.D. (via the solid-state telescope) resulting in an unambigous particle identification as shown in figures 3-5 and A-11. The number of heavy-ion events contained within each of the heavy-ion contours for runs A, B and C are given in table 4-1 along with the efficiency for observing a corresponding event in the beta decay spectrum. All "simple" beta decay half-lives given in table 4-1 were obtained using every beta seen within the beam-off time interval as opposed to using just the first beta within each beam-off time interval. The relatively weak fast background component was determined by placing a heavy-ion contour around ^{11}Be for runs A & C and around the long-lived Li isotopes for run B. The magnitude of the fast background component was observed to be fairly small with half-lives ranging from 3 to 5 ms. Only run B required careful consideration of the fast background contribution to extracted half-lives. Further investigations studing

possible correlations between the magnitude of the fast background component and the electron energy did not reveal evidence for the existance of such a correlation. The choice of the electron energy gate did however change the extracted half-lives with the largest deviation being around 9% for ^{9}Li (with the deviation representing mostly fluctuations with a slight tendency toward predicting longer half-lives for larger electron energy gates). The half-lives of ^{17}C and ^{9}Li were taken directly from run C since run A had a relatively short beam-off time period. The shorter beam-off time period resulted in a poorly fit background contribution (which predicted too high a background contribution) and thus a shorter half-life. The small time steps recorded during the beam-off time period allowed the adjustment of the time coordinate bin size. Too small a bin size resulted in too few counts per channel to justify the use of a least squares fitting procedure whereas larger bin sizes weighted the decay constant strongly on the background. It was found that the half-life dependence on bin size was around the 8% level with larger bin sizes resulting in longer extracted half-lives (although ^{9}Li and ^{17}C did show deviations from this tendency). The mother-daughter decay modes were characterized by a parameter [T] which was explained earlier in section 3.3. This parameter was not found to affect the extracted half-life significantly if its variation was confined to around twice the daughter's decay half-life.

Shorter values of [T] substantially reduced the decay curve statistics resulting in a poor overall fit.

In conclusion this experiment resulted in the half-lives of eight neutron-rich light nuclei two of which represent first time measurements. Error bars were typically 10% of the extracted half-life which proves competitive when compared to previous measurements using similar techniques. It is noted that the half-lives as determined from the present investigation appear systematically shorter than those obtained from previous measurements. The cause of this discrepancy will be investigated in future experiments. The background rate represented the major contribution to the half-life uncertainty. Background events may have a number of different origins such as the stainless steel vacuum window. Since a substantial number of reaction products were observed to stop within the ΔE detector it is reasonable to assume that some of the heavier isotopes stopped in the stainless steel vacuum window from which their emitted betas would have a clean path to the detector system (this may be eliminated with some appropriately placed magnets). In addition this experiment produced valuable data concerning the performance of the RPMS which will aid in the design of the phase II device.

4.2 Recommendations for Future Study

The initial results of the first half-life measurements using the RPMS provide a promising outlook for continuation of these studies using different beam and target combinations. More detailed spectroscopic studies resulting in branching ratio determinations via beta-gamma coincidence experiments should also be possible due to the relatively background-free environment provided by the RPMS. Beta-gamma coincidence experiments are important because branching ratio data provide more direct comparisons to shell model predictions than do half-life determinations. In addition to branching ratio data, beta-gamma coincidence experiments can be used to obtain excited state energy information forthe daughter nucleus, mass determinations via beta Q value measurements, and may provide the information necessary to make J^{π} assignments. One particular experiment of considerable interest is associated with the beta-gamma coincidence for the decay of ^{14}Be to the predicted 0.94 MeV state in ^{14}B. The gamma signature should be relatively clean since the branching ratio to this state is predicted to be ≈98 % and could provide confirmation of the result obtained in the present experiment. Another recommendation for future decay studies is the development of a 4π neutron detector. Calculations as verified by existing experimental data indicate that as one moves away from the valley of stability the neutron threshold energies become small giving rise to

beta-delayed neutron emitters thus the need for beta-neutron coincidence experiments.

Further suggestions center on experiments to establish optimized yields for neutron-rich nuclei using different beam-target combinations. Results from the present experiment suggest significant advantages associated with heavier targets for the production of neutron-rich nuclei. If this tend continues, as is suggested from the Ganil work [Gu83], then the use of thorium and uranium targets should provide even greater yields of neutron-rich nuclei than the tantalum target used in the present study. Exploiting heavier beams such as ^{22}Ne and ^{40}Ar will allow the study of neutron-rich nuclei in different mass regions. A proposal to use ^{22}Ne at 25 MeV/A on a thorium target has been accepted and will be carried out this spring. It is anticipated that this reaction will provide sufficient yields of ^{17}B, $^{18-20}$C and $^{19-21}$N to allow half-life determinations. The observed deviation from projectile fragmentation systematics suggests that a quasi-elastic or deeply-inelastic production mechanism may be the dominant mechanism responsible for the isotopic yields. Since both of the aforementioned mechanisms are characterized by yields which peak near the grazing angle it will be important to measure isotopic yields as a function of scattering angle. Experiments performed away from 0° will allow the use of thinner targets (since the

beam can then be stopped in a faraday cup) which will result in reaction products of higher velocity and less energy spread. This concludes the section on recommendations for future study and demonstrates the vast potential for extending current investigations on exotic nuclei out to the very limits of particle stability.

Table 4-1

Isotope	Run A events	Run B events	Run C events	Decay mode	Run A $\tau_{1/2}$	Run B $\tau_{1/2}$	Run C $\tau_{1/2}$
^{9}Li	4511		896	simple	150±28*		173±14
^{11}Li		1094		simple		7.7±0.6	
^{11}Be	1573		1198	simple	3.0±1.0*		
^{12}Be	2443		588	M & D	20.9±2.1		21.6±2.2
^{14}Be		584		M & D		4.2±0.7	
^{12}B				M & D		20.3±1.3	
^{14}B	1213		1190	simple	13.4±0.8		12.2±0.8
^{15}B	836		210	simple	8.8±0.6		8.2±0.6
^{17}C	1066		1445	simple	183±52*		202±17

* Values were not used in the determinaion of the best half-life

All half-lives are given in msec

Appendix A

A.1 Design Concepts for Recoil Ion Analyzers

A.1.1 Introduction

A recoil mass analyzer is a device or instrument which employs electric and magnetic fields to achieve a desired separation between ions of interest and those considered as background. The separation is most commonly a spatial one [Mu81] although temporal separations are also used as in a time-of-flight spectrometer [Pi84]. The primary function of a separator is to dump the beam so that only a very small portion if any reaches the detector or collector. The second function of the apparatus is to separate the recoil nuclei according to mass or M/Q since mass and charge can not be uncoupled in the electromagnetic force equation. The difficulty associated with the design of a ion separator can be appreciated when one observes that the ratio of background events to 'good' events may reach values as high as 10^{10} or 10^{11} for some heavy ion reactions. The majority of this background is due to the beam with the remaining fraction attributable to undesirable events produced simultaneously with the 'good' events during the reaction. A specific separator design must be taylored to the phase

space characteristics of the emerging reaction products. These phase space characteristics vary dramatically from one reaction mechanism to another, thus providing a natural classification scheme for separators according to the type of reaction products to be separated. Within this classification scheme mass separators fall into one of four catagories given by

i) Fusion-Product Separators
ii) Fission-Product Separators
iii) Spallation-Product Separators
iv) Fragmentation-Product Separators

For both fusion-product separators such as the Selector for Heavy-Ion reaction Products (SHIP) at Gesellschaft fur Schwerionenforschung in Darmstadt [Mu81] and the MIT-BNL Recoil Mass Separator (RMS) [Di80] and fragmentation-product separators such as the Reaction Product Mass Separator (RPMS) at NSCL, beam elimination is critical since reaction products are peaked at 0°. An excellent review of existing mass separators and their design features is given in [En81]. The goal of this section will be to present techniques applicable to the design of general separators with subsequent sections making the transition from general to specific design considerations taking selected examples from the design of the Michigan State Reaction Product Mass

Separator (RPMS). The formalism developed in the following sections apply equally well to the design of spectrometers which differ from separators in that they allow direct mass measurements. With this difference noted the remaining discussion will use the words separator and spectrometer interchangably.

Within the last 25 years significant advances in our understanding of charged particle optics have been witnessed. Beginning with the emergence of a first-order matrix formulation of charged particle optics in the late 1950's [Co58,Pe61] to the completion of an extended second-order treatment in the mid 1960's [Br67], the field has experienced a steady and rapid growth. With the second-order matrix formulation acting as a foundation, a computer code called TRANSPORT became available in the early 1970's [Br70,Br73] ushering in a new era of computer assisted spectrometer design. Extension of the matrix algebra to higher-order has met with resistance because of the cumbersome nature of evaluating a prohibitively large number of matrix elements associated with standard beam line components. In addition it is a commonly held belief that alternative methods such as raytracing prove more efficient for the determination of higher-order aberrations than would a generalized third-order matrix theory. Although more CPU intensive, raytracing has the advantage that it includes all higher-order aberrations which is accomplished by numerically integrating the exact equations of motion as the

particle traverses through the system and thus in principle is only limited by the accuracy of the user inputted electric and magnetic fields. The program RAYTRACE has been used extensively to design a number of magnetic spectrometers [Ko81]. Recently, raytracing codes such as MOTER [Th79] have been developed which employ a sophisticated optimization algorithm capable of adjusting up to 40 system parameters in order to achieve a maximized system resolving power. Using a Monte Carlo simulation process, MOTER is capable of reducing or eliminating higher-order aberrations through the appropriate choice of system parameters thus improving tremendously on its predecessor RAYTRACE. Although raytracing techniques prove extremely powerful for the reduction of higher-order aberrations, it is the first and second-order formulations that paint a clear and concise picture of how one should view the transport of charged particle beams. Thus it is through the understanding of the matrix formulation that one gains the insignt or 'intuition' necessary for a systematic approach to spectrometer design. In many respects the development of a first-order solution represents the most difficult and critical aspect associated with achieving the best possible spectrometer system. This is true for two major reasons:

i) The first-order imaging and dispersion represent the largest contribution to the spectrometer's resolving power thus permitting higher-order

aberrations to be treated as perturbations on the first-order solutions.

ii) The choice of the first-order configuration affects the magnitude of all resulting higher-order aberrations and the ease with which these aberrations can be reduced or eliminated.

Before discussing the procedure for obtaining first-order solutions it is important to review the important parameters associated with charged particle trajectories through magnetic and electric fields. The ion parameters which determine the trajectory of the ion through an electromagnetic system are its charge Q, mass M, and velocity V. Since M and Q always appear together as M/Q in the force equations it is possible to reduce the required ion parameters to two, either (M/Q,V) or (M/Q,P). In addition to the ion parameters, the dispersive and imaging properties of common magnetic and electric field devices used in spectrometer systems must be discussed. There exist three basic electromagnetic devices capable of providing first-order dispersion, they are:

i) magnetic dipole (momentum dispersion)

ii) electric field (energy dispersion)

iii) Wien filter (velocity dispersion)

Various combinations of the above devices can be used to obtain M/Q, P/Q, T/Q and V dispersion corresponding to mass, momentum, energy and velocity spectrometers respectively. Another important class of electromagnetic devices are the quadrupoles which provide first-order imaging for the system. Because quadrupoles act as perfectly astigmatic lenses they are usually found as doublets in spectrometer systems in order to achieve focussing in both transverse coordinates. However in a number of spectrometers the dispersive plane imaging can be achieved directly from the dipole field eliminating the need for a quadrupole doublet but still requiring a y-imaging quadrupole. The first-order focusing strength associated with a magnetic dipole is proportional to the bend angle through the device and can only produce dispersive plane focusing. The remaining ingredients required to determine first-order solutions are the physical and practical constraints imposed on the system. These constraints generally revolve around

i) envelope size which determines the aperture requirements of the differing electromagnetic elements used in the spectrometer.

ii) available area which determines the maximum physical size of the spectrometer.

iii) available electric and magnetic field strengths which determine the overall dispersion and imaging properties of the spectrometer.

A majority of the constraining criteria can be directly tied to economic limitations. Finally, one must always keep in mind the primary objective of any particular spectrometer design, namely the type and degree of spectrometer selectivity needed for the physics under investigation. In general one is often required to compromise the 'best' possible design to insure the flexibility of the device, allowing a range of differing experiments to be carried out. Differing first-order systems are then composed of a combination of the aforementioned elements in order to achieve a desired first-order solution subject to the imposed constraints. In general more than one first-order solution exists which can satisfy the first-order criteria. These differing solutions correspond to differing optical modes of the system, and reflect such differences as point-to-point v.s. point-to-parallel imaging or the number of cross-overs etc. To chose the best first-order solution involves a number of considerations as discussed earlier but one suggestion states that the source of second and higher-order aberrations is related to the magnitude of the first-order transfer coefficients and their derivatives. Once the fist-order solution has been chosen then techniques for the elimination of higher-order aberrations come into play starting with those of second-order.

A general prescription has been put forth describing how to eliminate arbitrary N^{th}-order aberrations [Br70]

without significantly affecting the $(N-1)^{th}$-order solutions. This method relies on the matrix formalism to describe a specific N^{th}-order coupling coefficient in terms of products of first-order Taylor coefficients and a Greens function which contains additional combinations of first-order Taylor coefficients. The next section will deal with this in a quantitative way and indicate the procedure used to reduce higher-order aberrations.

A.1.2 Beam Optics Notation

In order to put the treatment of charged particle optics on a more quantitative foundation we need to establish a coordinate system and notation which is conducive to the understanding of beam transport theory. The Serret-Ferenet coordinate system, shown in figure A-1 represents such a system where an arbitrary 'ray' or trajectory is defined relative to the 'central ray' of the system. This 'central ray' may correspond to a particular P/Q as for a momentum spectrometer, M/Q as for a mass spectrometer, T/Q as for an energy spectrometer, or V as for a velocity spectrometer depending on the type of spectrometer under investigation. The matrix formulation employs a set of 6 coordinates (see table A-I) which are used to describe the spatial and dispersive characteristics associated with an arbitrary ray. For the sake of

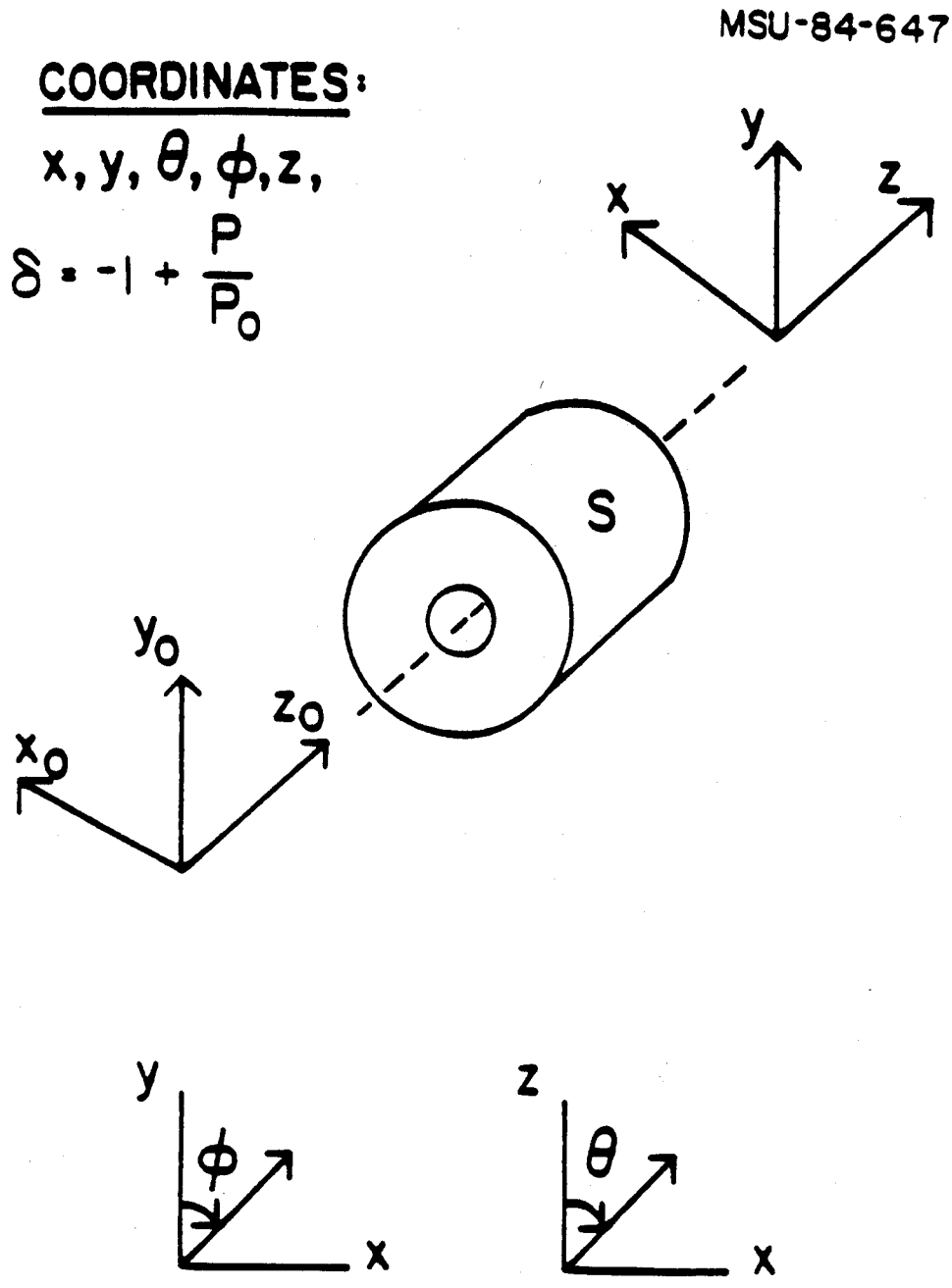

Figure A-1. Coordinate system used for magnetic optical systems following the notation of TRANSPORT.

Table A-1

x= radial displacement of the arbitrary ray with respect to the assumed central trajectory.

θ= the angle this ray makes in the radial plane with respect to the assumed central trajectory.

y= transverse displacement of the ray with respect to the assumed trajectory.

φ= the transverse angle of the ray with respect to the assumed central trajectory.

ℓ= the path length difference between the arbitrary ray and the assumed central trajectory.

δ_p= the fractional momentum deviation of the ray from the assumed central trajectory.

Table A-1. Definition of the coordinates used in the ion optical program TRANSPORT.

completeness it will be shown how the matrix formulation evolves from the exact equations of motion governing a charged particle in a static magnetic field.

The matrix approach starts by describing a charged particle trajectory in terms of a Taylor's expansion

$$x(t)=\sum (x|x_o^{\kappa}y_o^{\lambda}\theta_o^{\mu}\phi_o^{\nu}\delta_{p_o}^{\chi})\ x_o^{\kappa}y_o^{\lambda}\theta_o^{\mu}\phi_o^{\nu}\delta_{p_o}^{\chi}$$

$$y(t)=\sum (y|x_o^{\kappa}y_o^{\lambda}\theta_o^{\mu}\phi_o^{\nu}\delta_{p_o}^{\chi})\ x_o^{\kappa}y_o^{\lambda}\theta_o^{\mu}\phi_o^{\nu}\delta_{p_o}^{\chi} \qquad (A-1)$$

where x(t) and y(t) represent the transverse position of the particle as a function of its distance along the central trajectory (t). The subscript $_o$ indicates the coordinate values associated with the ray at the object location (t=0). The general curvilinear equation of motion for a charged particle in a static magnetic field is given by [Br70]

$$P\frac{d^2\vec{T}}{dT^2} = \frac{Q}{P}\left(\frac{d\vec{T}}{dT} \times \vec{B}\right) \qquad (A-2)$$

where Q is the charge of the ion, P its momentum, $\vec{T}$ its position vector and T the distance traversed. Equation (A-2) has made use of the fact that P is a constant of the motion and $\vec{B}$ represents the magnetic induction. Substitution of the expression (A-1) into a coordinate specific form of the

equation of motion allows the Taylor coefficients to be solved in terms of the magnetic field. If the magnetic field is such that it can be expressed in terms of an anti-symmetric scalar potential in the y coordinate.

$$\phi(x,y,t) = -\varphi(x,-y,t) \tag{A-2}$$

a significant simplification results. Condition (A-2) requires the magnetic field to be everywhere perpendicular to the magnetic midplane (y=0) and allows the description of the magnetic field $\vec{B}(x,y,t)$ throughout all space if the normal derivatives (in the x coordinate) of $B_y(0,0,t)$ are known. The median plane magnetic field posessing this type of symmetry may be described in terms of a multipole expansion

$$B_y(x,0,t) = B\rho \sum K_n(t)\, x^n \tag{A-3}$$

where $K_n(t)$ is proportional to the n^{th} partial derivative of B_y with respect to x on the central trajectory. Substituting the multipole expansion of the magnetic field given in (A-3) into the field dependent Taylor coefficients results in coupling coefficients having the following multipole strength dependence

$$(x_i | x_o^{\kappa} y_o^{\lambda} \theta_o^{\mu} \phi_o^{\nu} \delta_{p_o}^{\chi}) = \pm \left[\frac{n!}{\kappa!\lambda!\mu!\nu!\chi!} \right] I_{in}(t) \qquad \text{(A-4)}$$

$$+ \text{(terms involving } K_0, \ldots, K_{n-1})$$

where $n=(\kappa+\lambda+\mu+\nu+\chi)$ and

$$I_{in}(t) = \int_o^t G_i(t,\tau)\, K_n(\tau)\, \Pi\, (x|\alpha_k)^{\eta_k}\, (y|\beta_l)^{\omega_l}\, d\tau \qquad \text{(A-5)}$$

$$(\alpha_k, \eta_k) \in \{ (x_o,\kappa), (\theta_o,\mu), (\delta_{p_o},\chi) \}$$

$$(\beta_k, \omega_k) \in \{ (y_o,\lambda), (\phi_o,\nu) \}$$

$$G_1(t,\tau) = (x(t)|\theta(\tau))$$

$$G_2(t,\tau) = (\theta(t)|\theta(\tau)) \qquad \text{(A-6)}$$

$$G_3(t,\tau) = (y(t)|\phi(\tau))$$

$$G_4(t,\tau) = (\phi(t)|\phi(\tau))$$

Median plane symmetry conditions restrict aberrations to those which contain y and/or ϕ an even number of times. Specifically, the minus sign in (A-4) is used when y and/or ϕ appear 0,4,8,12,... times and the plus sign is used when

they appear 2,6,10,... times. The general form of the coupling coefficients given in (A-4) represents a powerful result which may be used to determine the optimum location of a correcting multipole field which is located at the value of t giving rise to a maximum in $I_{in}(t)$. Although this technique provides a method of eliminating higher-order aberrations it generally becomes impractical for $n \geq 3$ and in some cases introduces differing aberrations of the same order that limit the obtainable resolving power of the device. For most spectrometer designs it is sufficient to carry this solution out to second-order in which case a ray's position on the focal plane is given by

$$x_f = \sum_i (x|\alpha_i)\alpha_i + \sum_{ij}\sum (x|\alpha_i\alpha_j)\alpha_i\alpha_j \qquad (A\text{-}7)$$

where

$(x|\alpha_i)$ = first-order Taylor coefficients

$(x|\alpha_i\alpha_j)$ = second-order Taylor coefficients

$\alpha_i \in \{x, \theta, y, \varphi, \delta_m, \delta_p\}$

where the mass dispersion coordinate δ_m, similiar to the momentum dispersion coordinate δ_p, has been introduced to fascilitate discussion of mass spectrometers. Again the

assumption of midplane symmetry results in the following simplification

$$(x|y_o)=(x|\phi_o)=(y|x_o)=(y|\theta_o)=0 \qquad (A-8)$$

As stated earlier the coupling coefficients are dependent on the multipole field components of order equal to or less than the order of the coupling coefficient. The goal of spectrometer design is to achieve the maximum resolving power for a specified phase space transmission through the device as is economically feasible. Resolving power for an isotope separator is defined by

$$R_m = M/\delta M \qquad (A-9)$$

where δM represents the full width at half maximum of a peak at mass M. For a given object size Δx and magnification m of the spectrometer system, R_m is directly proportional to the system dispersion $D_m=(x|\delta_m)$:

$$R_m=D_m/m\Delta x \qquad (A-10)$$

where the dispersion is a direct measure of the spatial separation d between focussed species of M and $M+\Delta M$ at the focal plane implying the relation:

$$D_m = d(M/\Delta M) \qquad (A-11)$$

Thus high resolving power is achieved through a combination of large dispersion and low magnification at the focal plane location. The methods outlined in this section will be used to describe the design of the RPMS in the following sections.

A.2 Motivation for a Mass Separator at NSCL

Recently, heavy ion reaction mechanisms such as fusion, deep inelastic, and fragmentation have proven prolific in the production of exotic nuclei. Utilization of the high yields associated with these complex many-body collisions is contingent upon the development of analyzing systems capable of separating relevant events from a plethora of unwanted events as well as transporting these events of interest to a background-free environment where they may be studied using conventional detector systems. A major branch of nuclear physics is devoted toward the study of exotic nuclei, their stability, their decay modes, and their half-lives. The nature of heavy ion collisions make them promising candidates for extending this field of study out to the very limits of particle stability. The fragmentation mechanism which is seen to dominate at high projectile energies is particularly promising since the

observed phase space volume associated with the reaction products is remarkably compatible with the acceptance capabilities of spectrometer systems used to study such nuclei. Combining the contributions from thicker targets and kinematic focussing features associated with high-energy fragmentation should improve yields by approximately 10^6 over deeply-inelastic transfer reactions. From the standpoint of spectrometer design, narrow angular distributions are a welcome sight since they reduce the effect of geometric aberrations on the mass resolving power. Likewise, narrow momentum distributions reduce chromatic aberrations that could degrade the mass resolving power. However, even more importantly are the economic considerations surrounding the use of large acceptance spectrometer systems which require large-gap magnetic and electric fields. Another important feature associated with the high-energy nature of fragmentation is related to the charge state distribution of the emerging reaction products which is peaked at the fully-stripped value for low mass fragments and provides yield gains of 2 or 3 over conventional reaction mechanisms which spread a given mass over many differing charge states.

Disadvantages associated with fragmentation reaction products are their high electric rigidities which require large values of the electric field integral to achieve high resolving power. Although this does not represent a serious

problem for low mass nuclei where the percentage-wise separation of differing M/Q species is relatively large, it can represent a significant problem when heavier mass reaction products are under investigation. Likewise heavier mass fragments, unlike the lighter mass fragments, do not concentrate a given mass species into a single charge state thus reducing the overall collection efficiency. Furthermore, the emerging reaction products are peaked at 0° requiring elimination of the beam which can be many orders of magnitude more intense than the isotopes under investigation. These problems although troublesome in no way outweigh the benefits associated with the fragmentation mechanism which in many cases provide the only known way to reach the very exotic isotopes. The major advantages associated with recoil separators when compared to ISOL type separators are the shorter detection and collection times allowing extremely short-lived species to be investigated and elimination of ion source efficiency factors which bias specific isotopic species. Although some overlap in capabilities exist between the two techniques, they may clearly supplement each other for the study of exotic nuclei.

Taking advantage of the high intensity heavy ion beams available from the K500, a mass separator would prove tremendously useful for the study of exotic nuclei particularly their half-lives and decay modes. Of primary

interest are the measurements of half-lives which require relatively high beam intensities which is exactly where NSCL will be the most competitive. The coupling of high intensity beams with larger spectrograph transmission should produce estimated increases of 10^6 in exotic nuclei yields enabling new particle stability determinations as well as half-life measurements.

A.3 The M.S.U Reaction Product Mass Separator

The primary goal in the development of a mass separator at NSCL was to design and build a device capable of utilizing the competitive features associated with heavy ion beams available from the K500 cyclotron for the production of exotic nuclei. The separator should employ magnetic and electric fields to achieve the fast 'on-line' isotope separation necessary for the study of short-lived species and should focus reaction products of a particular M/Q in x, y, and velocity on a mass-dispersive focal plane thereby eliminating the need for a large focal plane detector system and its accompanying background problems.

The phase I RPMS meets such design criteria by triple-focussing reaction products, of 30 MeV/A or less, directly from the target to a mass-dispersive focal plane approximately 14 m down line [No84]. The RPMS achieves M/Q dispersion through the use of an E X B device (Wien filter)

followed by a magnetic dipole and may be classified as a standard Aston mass spectrometer arrangement. A pair of quadrupole doublets are used to achieve the required imaging where the first of these doublets is located directly in front of the Wien filter and provides collimation of the initially diverging reaction products. The remaining doublet rides on the movable tail section just following the magnetic dipole and focusses separated isotopes to a point on the focal plane (see figure A-2). At the core of the RPMS sitting on a movable undercarriage is a 5 m MARK VI Wien filter on loan from the Berkeley Bevatron. The Wien filter employs a +250 kV Glassman supply and a -400 kV Spellman supply to generate a uniform electric field (E_w) throughout its 4" gap. Since the entire Wien filter moves, it proved most conveneint to mount the high-voltage supplies directly to their corresponding feed-throughs so they could travel with the velocity filter (see figure A-3). The Wien filter magnetic field (B_w) is achieved with a pair of current sheets providing a maximum field of 600 Gauss @ 600 amp. limited by available water-cooling. Just following the Wien filter located at the pivot point of the RPMS is a large-gap (6") dipole magnet acquired from Cornell which provides a maximum field strength $(B_w)_{max}$=4.3 kG (power supply limited). The leading pair of large 8" aperture quadrupoles were obtained from the Space Radiation Effects Laboratory (SREL) and the remaining less massive 4" quadrupole doublet,

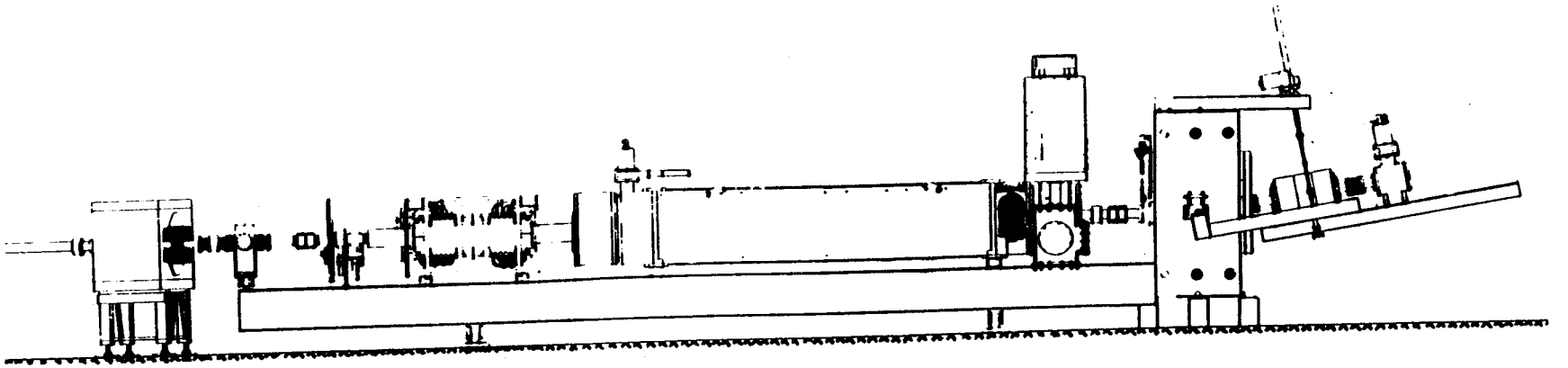

Figure A-2. Pictorial drawing of the RPMS. The beam inflector magnet is the first component at the left, followed by the target chamber, aperture holder, quadrupole doublet, Wien filter (5 m long) with high voltage supplies on the top right end, magnetic dipole and pivoting "tail" with quadrupole doublet and focal plane detectors at the right end.

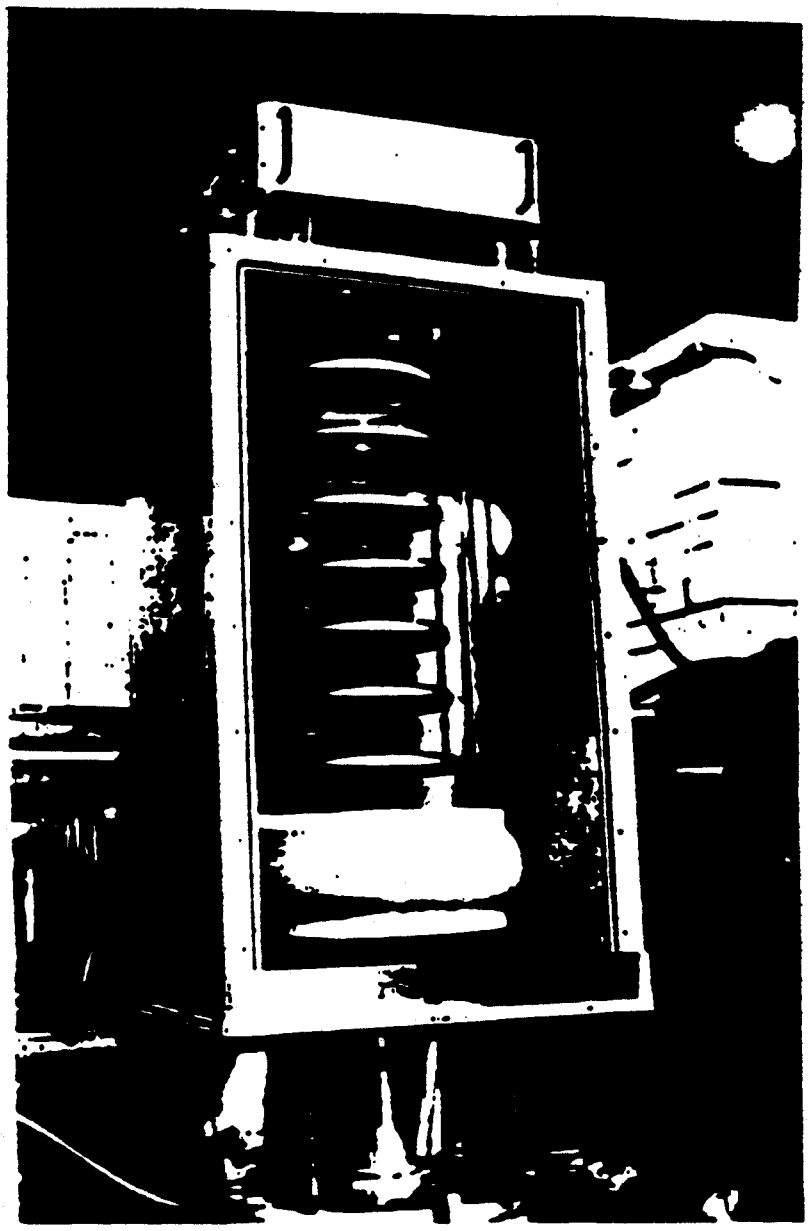

Table A-3. Velocity, dispersion and M/Q scaling features of the RPMS.

obtained from Maryland, sits atop the movable tail section. The movable tail section is supported and controlled by a screw wench bolted to the top of the dipole and provides variable tail angles between 0° - 20°. An aperture is positioned behind the target to shield the Wien filter cathode and prevent plate scattering. In addition, a pair of horizontal velocity slits are positioned at the velocity dispersive plane between the Wien filter and Cornell magnet to privide additional velocity selection.

Two features of the M.S.U. RPMS make it unique among mass separators first, it is the only triple-focussing device designed for heavy ion reaction products with energies greater than 5 MeV/A and secondly, it is not confined to a 0° scattering angle but can be varied from 0° - 30°. The variable scattering angle was accomplished in such a way as to limit the area swept out by the device thereby allowing it to fit within the confines of the available experimental area. As shown in figure A-4 this was done by placing the pivot point of the device directly under the dipole and using an 'inflector' magnet, located just before the target, to swing the beam through $\pm 15^{\circ}$. The variable scattering angle is beneficial because it eliminates problems associated with the beam at 0° and it allows the study of isotopic yields from predominantly non-fragmentation mechanisms.

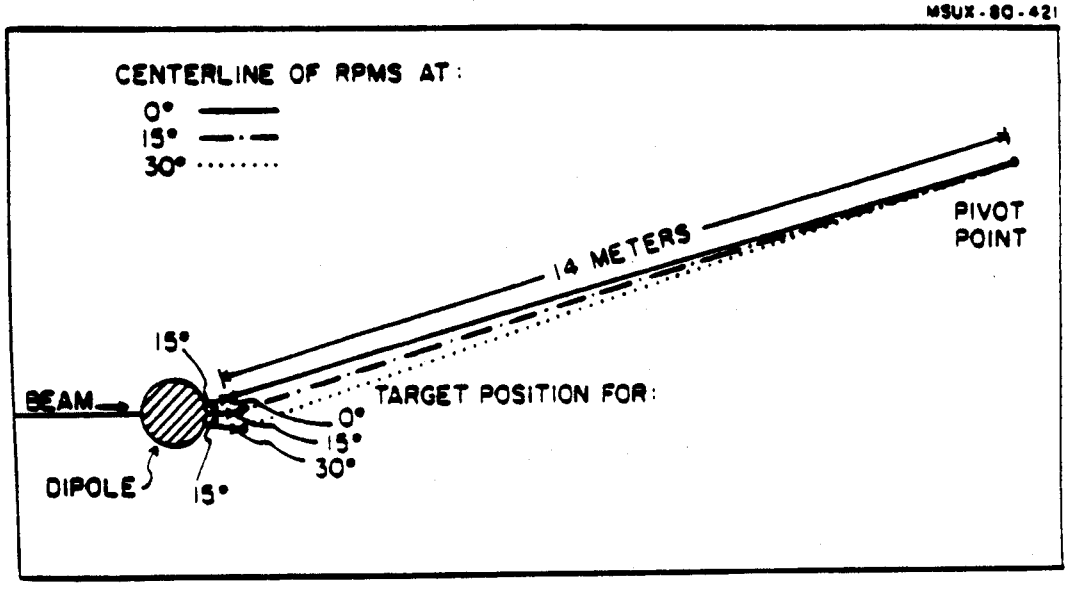

Figure A-4. Illustration of the angle-changing technique used for the RPMS with scattering angles of 0 , 15 , and 30 explicitly shown.

The first-order optical design was obtained with a modified version of TRANSPORT which had all 'path-length' terms, contained in the fifth column of the first-order matrices, replaced with mass dispersive terms similar to the way momentum dispersive terms are used in the sixth column of the same matrices. The first and second-order Wein filter matrix elements of Ianoviciu [Ia74] were calculated separately with the code TRANSE [Ha80] and then input into TRANSPORT as non-adjustable parameters. All calculations involving the Wien filter assumed a 5 m length with a magnetic field strength of 470 Gauss and maximum electric field strength of 40 KV/cm. For high velocity reaction products, mass resolving power limitations are dominated by the electric field integral $\int E_w dl$ which for the MARK VI Wien filter is approximately 2×10^7 V. Although the electric field integral dominates mass resolving power for high rigidity fragments, it is always possible to increase mass resolution at the expense of phase space acceptance indicating that a more appropriate figure of merit may be the total electric field strength parameter given by

$$V_E = E_w \times l \times d \times w = 4.0 \times 10^5 \ V\text{-}m^2 \qquad (A\text{-}12)$$

where

E_w = electric field strength (40 kV/cm)

l = effective length of E_w (5m) (A-13)

d = field gap (0.1 m)

w = width of electric field plates (0.2 m)

Figure A-5, taken from [Ha81], illustrates how mass dispersion depends on the energy of the reaction products for a typical RPMS optical layout. Two different first-order solutions, as shown in figure A-6, resulted from the requirement of point-to-point imaging in both the dispersive and non-dispersive planes and zero velocity dispersion at the mass dispersive focal plane. The basic difference between the two solutions is that solution (i) requires slightly greater quadrupole focussing in order to achieve the intermediate y cross-over not found in solution (ii), otherwise they may be considered equivalent. The contribution of higher-order effects on the mass resolving power were examined with the code RAYTRACE, the results of which are shown in figure A-7 (a). The results illustrate the limitations on mass resolution, which are directly attributed to chromatic aberration induced by the quadrupoles, manifested through the large $(x|\theta\delta)$ term. This effect was reduced by offsetting the first quadrupole doublet with respect to the Wien filter which had the effect of reducing the momentum band-pass of the RPMS in such a way as to significantly improve the resolving power of the

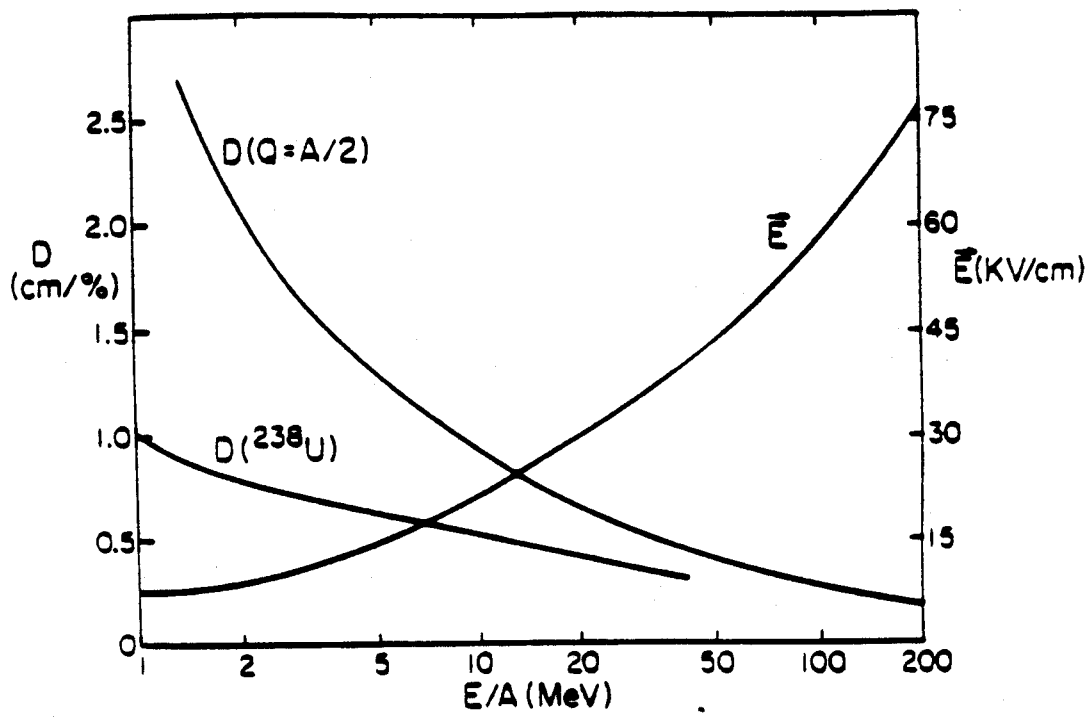

Figure A-5. Maximum achievable dispersion for the Mark VI Wien filter assuming a magnetic field limit of 470 Gauss. The magnification of the system is unity for all calculations and the solid angle is roughly constant over the entire energy range.

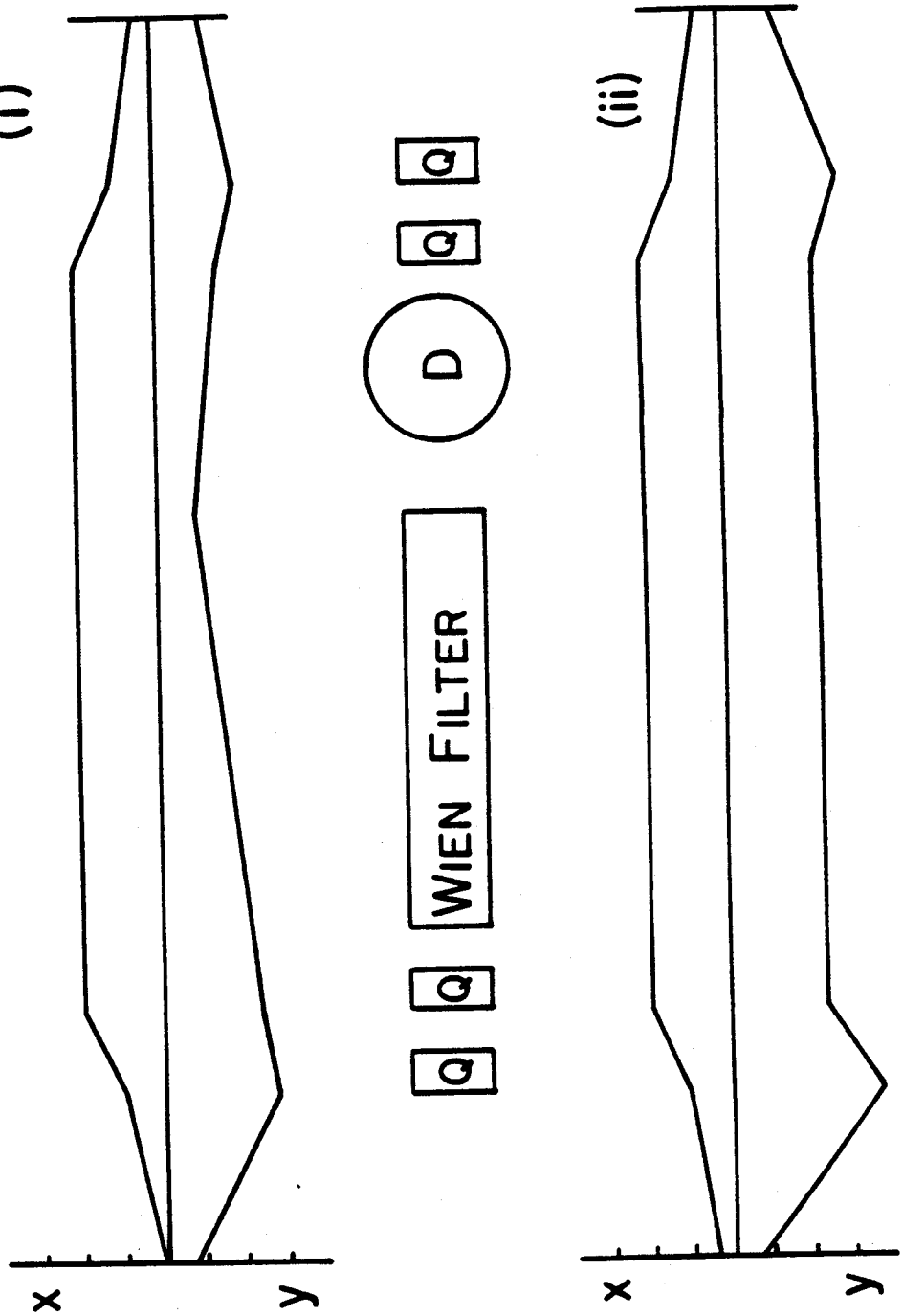

Figure A-6. Schematic drawing of the X and Y beam envelopes for two different optical modes of the RPMS.

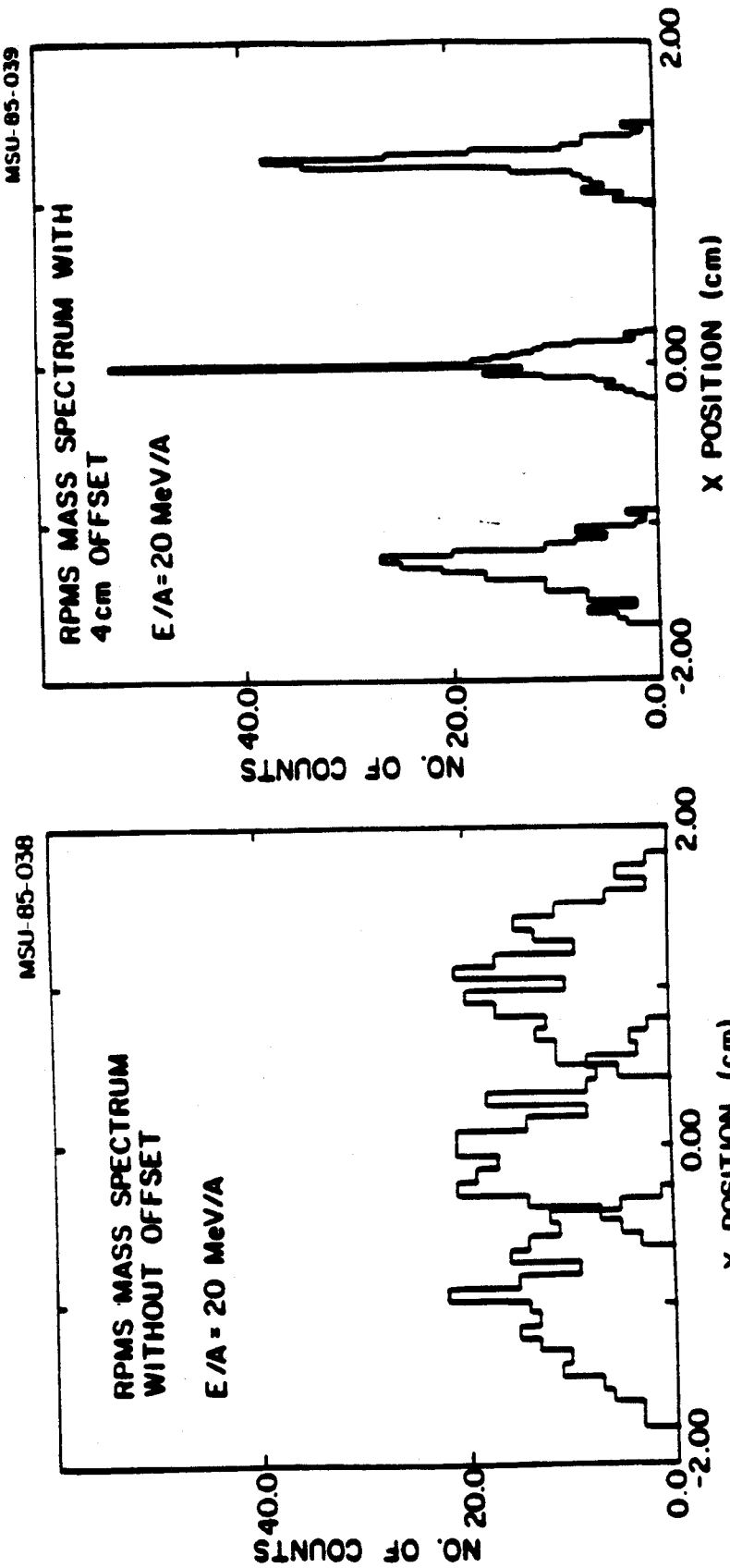

Figure A-7. One dimensional histograms calculated with RAYTRACE for the three mass groups A-49,50,51 assuming Q-25 at 20 MeV/A. a) With the quadrupole axis same as the Wien filter axis. b) With the quadrupole axis displaced by 4 cm to reduce the effect of chromatic aberrations.

device as shown in figure A-7 (b). A significant discrepancy between the first-order resolving power and that calculated with RAYTRACE stressed the importance of higher-order chromatic terms when large momentum bandpass is allowed as illustrated in figure A-8. A two-dimensional histogram calculated with the program RAYTRACE illustrates the type of mass resolution predicted for the RPMS when one assumes a $1^{\circ} \times 4^{\circ}$ angular acceptance and a ±12% energy bandpass for nuclei having 20 MeV/A (see figure A-10 and accompanying table A-2). The RPMS transmission was calculated as shown in figure A-9 and shows a transmission for the central mass of approximately 45% with the +12% energy rays showing higher transmission than the -12% energy rays. This concludes the discussion of the design and construction features of the RPMS. The next section will discuss the initial testing and performance of the RPMS.

A.4 Testing and Performance of the RPMS

Initial testing of the RPMS required threading a 35 MeV/A $^{14}N^{5+}$ beam through the system to check its over-all alignment and imaging characteristics. Scintilators where placed at the target, intermediate velocity dispersive plane, and the focal plane providing various beam viewing locations. Verification of the RPMS aliegnment was hindered by the 4" offset between the leading quadrupole doublet and

MSU-85-040

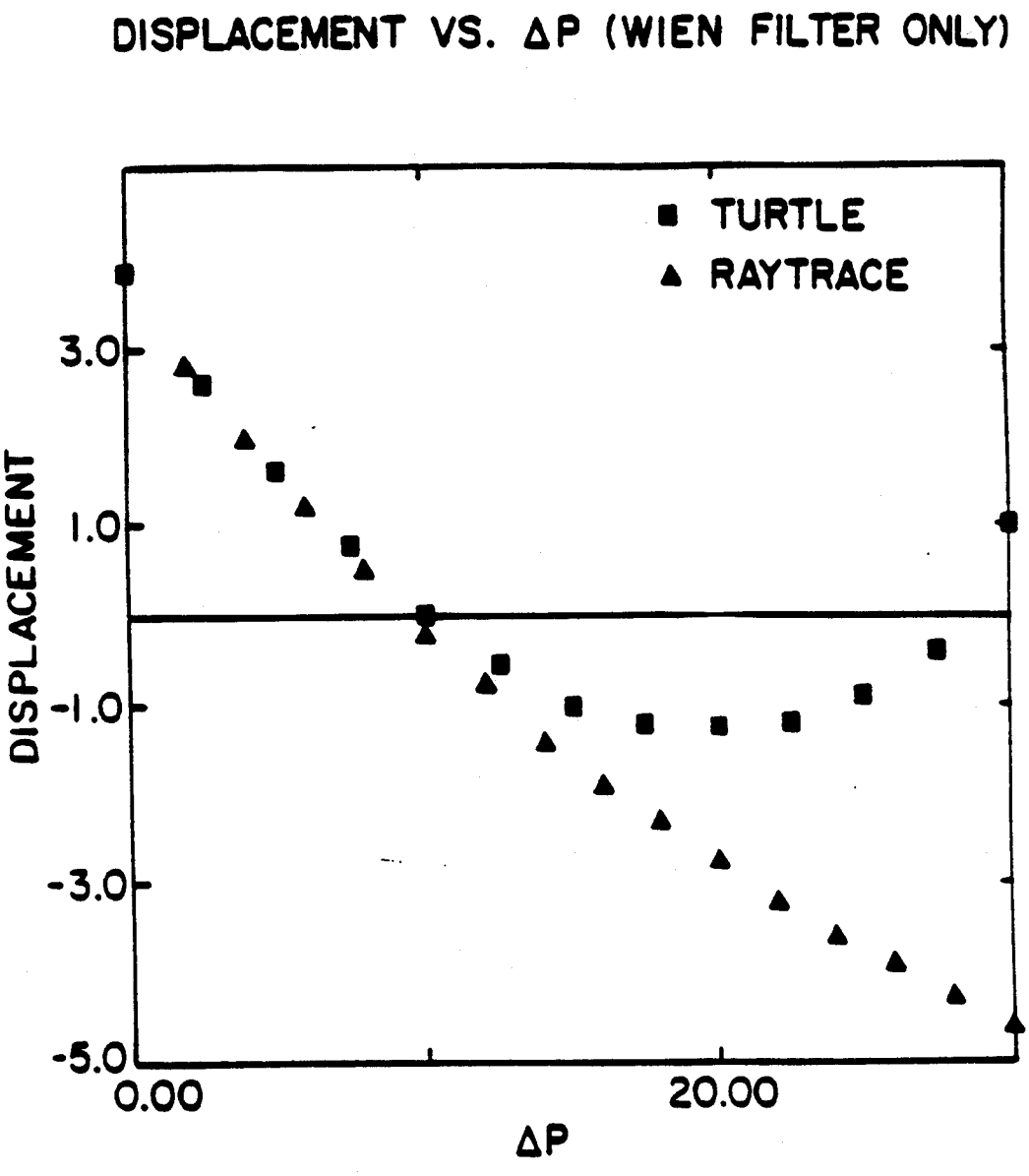

Figure A-8. Calculation of a ray's displacement at the exit of the Wien filter as a function of the momentum illustrating the large discrepancies between second-order calculations and ray tracing for large momentum ranges.

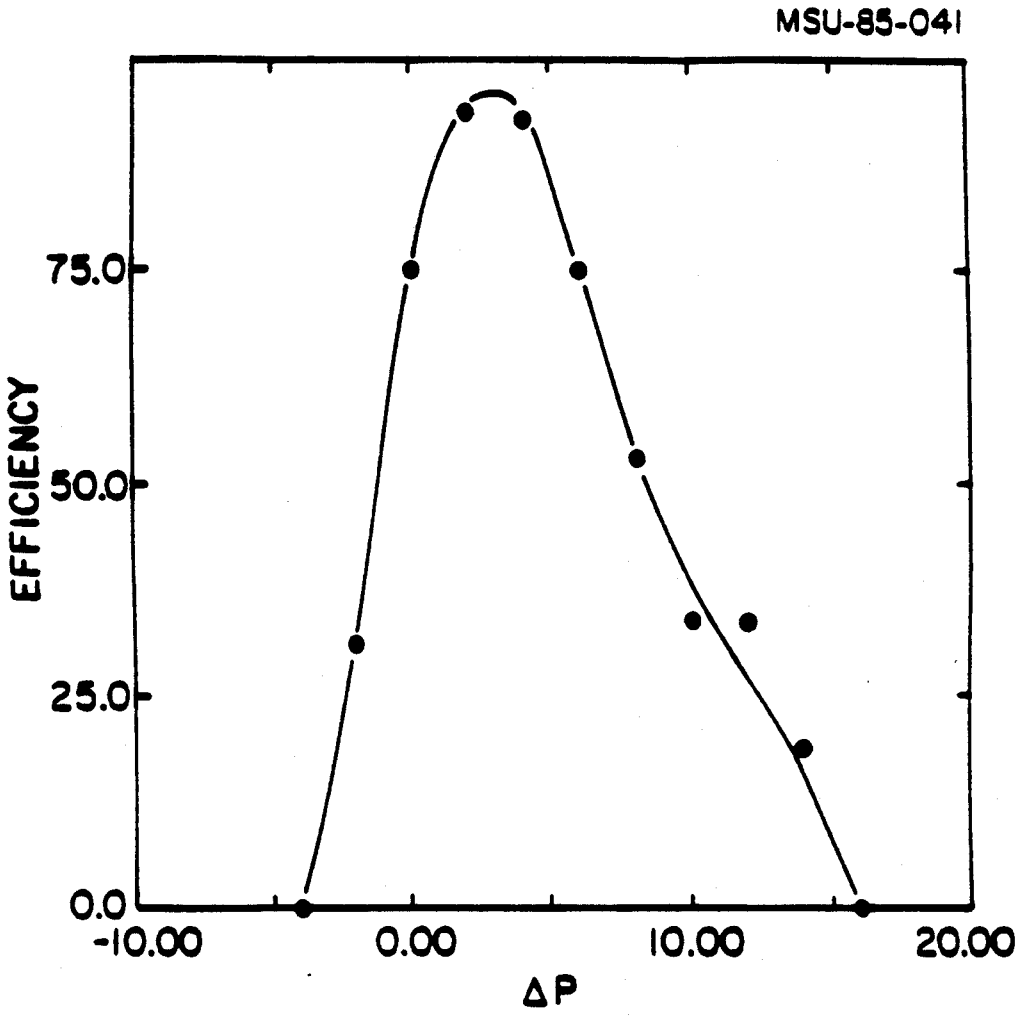

Figure A-9. Calculation of the momentum bandpass of the RPMS with the offset axis.

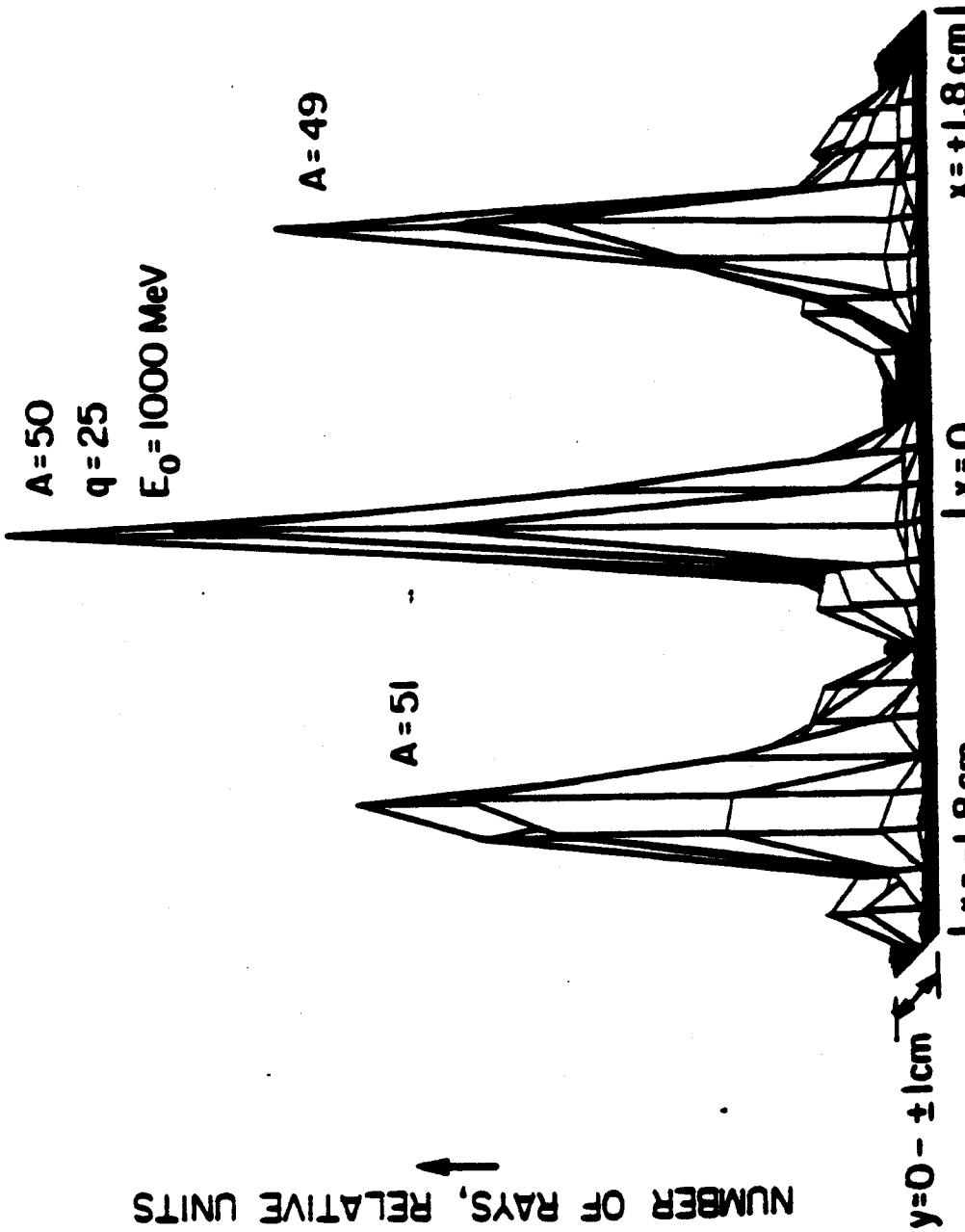

Figure A-10. Two-dimensional histogram calculated with the program RAYTRACE, illustrating the mass separation at 20 MeV/A.

Table A-2

RPMS	Parameters	Prototype
Layout	QQWDQQ	(W= Wien Filter)
Length	14.3 m	
Max. Energy	30 MeV/u	
Angular Range	0° - 30°	
Resolution	$M/\Delta M = 100^{*}$ (base-to-base)	
	$= 200^{**}$ (base-to-base)	

* Calculated for E/A = 20 MeV and M = 2Q with TURTLE assuming 1 msr and 16% energy range.

** Calculated for $^{40}Ca + {}^{40}Ca$ fusion products at E_{beam}/A = 5 MeV assuming 1 msr an 8% energy range.

Table A-2. Optical design parameters for the RPMS.

Wien filter which required the beam to skim within 1 cm of the bottom plate of the Wien filter. Although some difficulty was encountered an intermediate image was achieved at the velocity dispersive plane and allowed the Wien filter electric field to be tested and roughly calibrated. Varying the electric and magnetic field strengths produced the anticipated vertical displacements at the velocity dispersive plane thus verifying that the Wien filter was performing as a velocity filter. With both B_W and the tail angle at zero an image was obtained at the focal plane. The imaging properties of the quadrupoles could not be checked easily because of the quadrupole steering induced by the off-axis displacement of the beam. The alignment difficulties did not pose a significant problem however, since the reaction products easily make it through the system. Converting to a thick Be target and a focal plane detector system consisting of a 2-dimensional proportional counter (see section 3.1) backed by two large area (17.7 cm^2) Si(Li) detectors immediately produced heavy-ion reaction products at the focal plane detector system. To establish a mass reference point, a search for 'beam velocity' alpha particles was undertaken. These alpha particles had a characteristic signature associated with their punch through energy. Once the alpha particles were centered on the detector it was possible to scale to lower velocity M/Q=2 reaction products by turning down the

electric field strength and decreasing the quadrupole strengths. This procedure resulted in the appearance of $^{6}Li^{3+}$ and $^{10}B^{5+}$ with a hole between associated with the particle unstable $^{8}Be^{4+}$ isotope. The next step was to scale to differing M/Q reaction products leaving the velocity bite constant. This was done by moving the tail angle and readjusting the quadrupole strengths. The final diagnostic was to see if the dispersion scaled as expected which required similiar percentage increases in E_w , B_w , B_c , and tail angle. An example of increasing the mass dispersion is shown in figure A-11. A summary table indicating the different scaling laws is presented in table A-3.

Although the qualitative performance of the RPMS has proven impressive, some questions still remain concerning the first-order imaging properties of the device. Further investigation of the performance of the RPMS will be continued in upcoming runs. It would prove enlightening to place the detector system at the velocity dispersive plane and quantitatively study the properties of the Wien filter. Other interesting questions associated with the transmission of the RPMS must be investigated in order to attatch cross-sections to observed nuclei. Although a sizable amount of work remains, the ability of the RPMS to separate heavy-ion reaction products and allow half-life determinations has been demonstrated. In my opinion, studies of low mass nuclei using the RPMS can continue with studies of the RPMS itself

Table A-3

Scaling Parameter	Constant Parameter	Quadrupoles	E_w	B_w	B_c	tail
M/Q	V_o & D_m	+P	-	-	-	-P
D_m	M/Q & V_o	-	+P	+P	+P	+P
V_o	M/Q & D_m	+P	-	-P	-P	-2P

P = Percentage Change

$V_o = E_w / B_w$ = Central Velocity through Wien Filter

D_m = Mass Dispersion

Table A-3. Velocity, dispersion and M/Q scaling features of the RPMS.

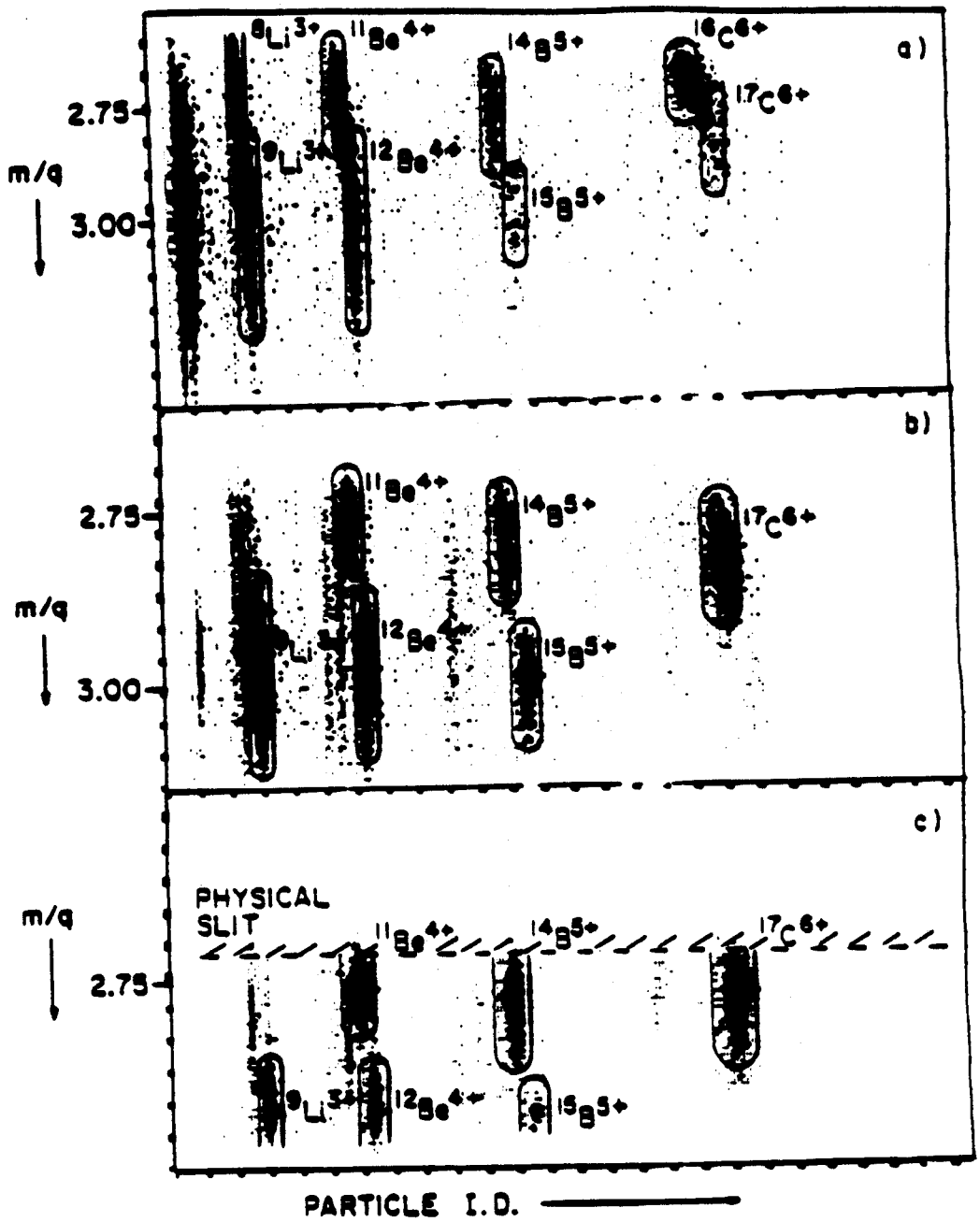

Figure A-12. Vertical position vs particle ID signal for a) low mass dispersion b) Higher mass dispersion c) maximum mass dispersion. In a) Z=1-6 groups are seen with $^{3}H^{1+}$, $^{6}He^{2+}$, $^{9}Li^{3+}$, $^{12}Be^{4+}$ and $^{15}B^{5+}$ forming the horizontal M/Q=3.0 line. Directly above this line one can see $^{8}Li^{3+}$, $^{11}Be^{4+}$, $^{14}B^{5+}$ and $^{16}C^{6+}$ having M/Q values 2.67, 2.75, 2.80 and 2.67 respectively. In b) the dispersion was increased to eliminate $^{8}Li^{3+}$ and $^{16}C^{6+}$ with electronic gates eliminating Z=1 and 2 species. In c) the dispersion was maximized in order to eliminate as may M/Q=3.0 species as possible.

being carried out in parallel.

LIST OF REFERENCES

Aj75 F. Ajzenberg-Selove, Nucl. Phys. A248 (1975) 1

Aj76 F. Ajzenberg-Selove, Nucl. Phys. A268 (1976) 1

Al78 D.E. Alburger, et al., Phys. Rev. C 17, (1978) 1525

Al81 D.E. Alburger, C.J. Lister, J.W. Olness, and D.J. Millener, Phy. Rev. C23 (1981) 2217

Ar71 A.G. Artukh, et al., Nucl. Phys. A176, (1971) 284

Au79 P. Auger, et al., Z. Physik A289, (1979) 255

Ba75 A. Barroso, and R.J.Blin-Stoyle, Nucl. Phys. A251, (1975) 446

Br67 K.L. Brown, SLAC Report No. 75, or Advances Partical Phys. 1, 71-134, (1967)

Br70 K.L. Brown, SLAC-PUB-762 June, 1970

Br71 G.E. Brown, Unified Theory of Nuclear Models and Forces (North-Holland Publ.,1971)

Br74 K.L. Brown and Ch.Iselin, CERN 74-2, (1974)

Br73 K.L. Brown, D.C. Carey, Ch. Iselin and F. Rothacker CERN 73-16, (1973)

Br77 K.L.Brown, F.Rothacker, D.C.Carey, and Ch.Iselin, SLAC Report No. 91, (1977)

Br78 B.A. Brown, W. Chung, and B.H. Wildenthal, Phys. Rev. Lett. 40, (1978) 1631

Br80a B.A. Brown, W. Chung, and B.H. Wildenthal, Phys. Rev. C21 (1980) 2600

Br80b B.A. Brown, W. Chung, and B.H. Wildenthal, Phys. Rev. C22 (1980) 774

Br85 B.A. Brown, private communication

Ch71 M. Chemtob and M. Rho, Nucl. Phys. A163, (1971) 1

Ch76 W. Chung, Ph.D. thesis, Michigan State University 1976

Co58 E.D. Courant and H.S. Snyder, Ann. Phys. (NY) 3, 1-48, (1958)

Cu81 M.S. Curtin, B.H. Wildenthal, and J.A. Nolen, Jr., NSCL Annual Report 1980-81, pg 55

Cu82 M.S. Curtin, B.H. Wildenthal, and B.A. Brown, Bull. Am. Phys. Soc. 27, (1982) 696

Di80 A.C. DiRienzo, H.A. Enge, S.B. Gazes, M.K. Salomaa and A. Sperduto, Phys. Rev. C21 (1980) 2101

Du84 J.P. Dufour, et al., Preprint CENBG 8430

En81 H.A. Enge, Nucl. Instr. and Meth. 186, (1981) 413

Gi84 R. Gilman, et al., Phys. Rev. C 30, (1984) 958

Go77 J. Gosset, et al., Phys. Rev. C 16, (1977) 629

Go78 J. Gosset, J. I. Kapusta, and G. D. Westfall, Phys. Rev. C18 (1978) 844

Go80 C.D. Goodman, et al., Phys. Rev. Lett. 44, (1980) 1755

Gu84 D. Guerreau, et al., Ganil Preprint IPNO DRE 83-19

Ha80 L.H. Harwood, private communication

Ha81 L.H. Harwood, and J.A. Nolen, Jr., Nucl. Instr. and Meth. 186, (1981) 435

He72 H.H. Heckman, D.E. Greiner, P.J. Lindstrom, and F.S. Bieser, Phys. Rev. Lett. 28, (1972) 926

Io74 D. Ioanoviciu, Int. J. Mass Spect. and Ion Phys. 15, (1974) 89

Kh78 F.C. Khanna, I.S. Towner, and H.C. Lee, Nucl. Phys. A305, (1978) 349

Ko81 S. Kowalski and H.A. Enge, Mit Program (unpublished)

Ko83 V.T. Koslowsky, Ph.D. thesis, University of Toronto, (1983)

La73 W.A. Landford and B.H. Wildenthal, Phys. Rev. C 7, (1973) 668

Le56 T.D. Lee and C.N. Yang, Phys. Rev. 104, (1956) 254

Le57 T.D. Lee and C.N. Yang, Phys. Rev. 105, (1957) 1671

Ma67 H.A. Mavromatis and L. Zamick, Nucl. Phys. A104, (1967) 17

Ma69 P. Marmier and E. Sheldon, Physics of Nuclei and Particles, (Academic Press, New York ,1969) 361

Mo78 D. J. Morrissey, W. R. Marsh, R. J. Otto, W. Loveland, and G. T. Seaborg, Phys. Rev. C18 (1978) 1267

Mo80 D.J. Morrissey, private communication

Mo81 S. Morinobo, I. Katayama, and H. Nakabushi, Proc. Int. Conf. on Nuclei Far from Stability, CERN 81-09, (1981) 717

Mi75 D.J. Millener and D. Kurath, Nucl. Phys. A255, (1975) 315

Mu73 N.C. Mukhopadhyay and L.D. Miller, Phys. Lett. 47B, (1973) 415

Mu81 G. Munzenberg et. al., Nucl. Inst. and Methods 186 (1981) 423

Mu84 M.J. Murphy, T.J. M.Symons, G.D. Westfall, and H.J. Crawford, Phys. Rev. Lett. 49, (1982) 455

No84 J.A. Nolen, Jr., L.H. Harwood, M.S. Curtin, E. Ormand, and S. Bricker, Proceedings of the Oak Ridge Conference.

Or81 E. Ormand, J. Nolen and J. Yurkon, Cyclotron Annual Report (1981) 73

Pe61 S. Penner, Rev. Sci. Instrum. 32, 150-160, (1961)

Pi84 C. Pillai, D.J. Vieira, G.W. Butler, J.M. Wouters, S.H. Rokni, K. Vaziri and L.P. Remsberg Preprint LA-UR 842960

Ra77 J. O. Rasmussen, R. Donanglo, and L. Oliveira, LBL Report No. LBL-6580, 1977 (unpublished)

Re73 B.S. Reehall and B.H. Wildenthal, Particles and Nuclei 6, (1973) #6

Se68 T. Sebe and M. Harvy, Preprint AECI 3007, 1968 (unpublished)

Sh74 K. Shimizu, M. Ichimura, and A. Arima, Nucl. Phys. A226, (1974) 282

Sh85 B. Sherrill, Ph.D. thesis, Michigan State University 1985

St79 G. Stigman, et al., Ann. Rev. Nucl. Part. Sci. 29, (1979) 313

Ti78 G.A. Timmer, F. Meurders, P.J. Brussaard, and J.F.A. Van Hienen, Z. Physik A288, (1978) 83

Th75 C. Thibault, R. Klapisch, C. Rigaud, A. M. Poskanzer, R. Prieels, L. Lessard, and W. Reisdorf, Phys. Rev. C12 (1975) 644

Th79 H.A. Thiessen, M.M. Klein, and K.G. Boyer, LASL Report, April, 1979 (unpublished)

To79 I.S. Towner and F.C. Khanna, Phys. Rev. Lett. 42, (1979) 51

Va79 K. Van Bibber, et al., Phys.Rev. Lett. 43, (1979) 840

We76 G.D. Westfall, et al., Phys. Rev. Lett. 37, (1976) 1202

We79 G.D. Westfall, et al., Phys. Rev. Lett. 43, (1979) 1859

Wi71 D.H. Wilkinson, et al., Phys. Rev. A166, (1971) 661

Wi73 D.H. Wilkinson, Nucl. Phys. A209, (1973) 470

Wi74 D.H. Wilkinson and B.E.F. Macefield, Nucl. Phys. A232, (1974) 58

Wi78 D.H. Wilkinson, A. Gallmann, and D.E. Alburger, Phys. Rev. C 18, (1978) 401

Wi80 H.S. Wilson, R.W. Kavanagh, and F.M. Mann, Phys. Rev. C 22, (1980) 1696

Wi82 D.H. Wilkinson, Nucl. Phys. A377, (1982) 474

Wi83 B.H. Wildenthal, M.S. Curtin, and B.A. Brown, Phys. Rev. C 28, (1983) 1343

Wu57 C.S. Wu, E. Ambler, R.W. Hayward, D.D. Hoppes, and R.F. Hudson, Phys. Rev. 105, (1957) 1413